

# Multiferroic hexagonal HoMnO<sub>3</sub> films

Von der Fakultät Maschinenwesen

der

Technischen Universität Dresden

zur

Erlangung des akademischen Grades

Doktoringenieur (Dr.-Ing.)

angenommene Dissertation

von

**M.Sc. Jong-Woo Kim**

geboren am 21. Mai 1977

in Chun-Cheon, Süd-Korea

2009

1. Gutachter: Prof. Dr. Ludwig Schultz (TU Dresden)
2. Gutachter: Prof. Dr. Manfred Fiebig (Universität Bonn)

Tag der Einreichung: 29.07.2009

Tag der Verteidigung: 22.12.2009

## Abstract

The fundamental properties of hexagonal multiferric  $\text{HoMnO}_3$  films have been thoroughly investigated. The films are grown by pulsed laser deposition on  $\text{Y:ZrO}_2(111)$  substrates. High quality epitaxial  $\text{HoMnO}_3$  films of 25 – 1000 nm thickness were successfully prepared. The film properties are compared to those of single-crystals. The magnetization measurements revealed that the films show a deviating magnetic behavior from the single-crystals in several ways. For instance, the films have a weakened antiferromagnetic  $\text{Ho}^{3+}$  order confirmed from magnetic susceptibility. The differences are likely to be related to the modified (mostly larger) lattice parameters of films. An approximate phase diagram in comparison with the single-crystal's one is constructed. For multiferroicity investigations, Second Harmonic Generation (SHG; in collaboration with the group of M. Fiebig) has been employed. By SHG, the ferroelectric polar order of the films is obviously confirmed. The ferroelectric switching at room temperature could be clearly demonstrated, whereas leakage of films requires generally a more sophisticated approach.

## Kurzfassung

Die fundamentalen Eigenschaften von hexagonalen multiferroischen  $\text{HoMnO}_3$  Schichten werden eingehend untersucht. Die dünnen Schichten wurden mittels gepulster Laserdeposition auf  $\text{Y:ZrO}_2(111)$ -Substraten gewachsen. Hochwertige epitaktische  $\text{HoMnO}_3$ -Dünnschichten von 25 – 1000 nm Dicke wurden erfolgreich hergestellt. Die Dünnschichteigenschaften werden mit denen von Einkristallen verglichen. Die Magnetisierungsmessungen ergeben, dass die dünnen Schichten ein von den Einkristallen in verschiedener Weise abweichendes magnetischen Verhalten zeigen. Zum Beispiel haben die dünnen Schichten eine abgeschwächte antiferromagnetische  $\text{Ho}^{3+}$  Ordnung, die durch die magnetische Suszeptibilität bestätigt wird. Die Unterschiede sind wahrscheinlich auf die veränderten (meistens grösseren) Gitterparameter der dünnen Schichten zurückzuführen. Ein Phasendiagramm wird zum Vergleich mit Einkristallen konstruiert. Durch Second Harmonic Generation (SHG; in Zusammenarbeit mit der Gruppe von M. Fiebig) wird die ferroelektrische Ordnung der dünnen Schichten eindeutig bestätigt. Das ferroelektrische Umschalten bei Raumtemperatur kann eindeutig nachgewiesen werden, wobei durch den Leckstrom der dünnen Schichten allgemein eine detailliertere Vorgehensweise benötigt wird.



# Table of contents

<b>Introduction</b>	<b>1</b>
<b>1 Fundamentals</b>	<b>5</b>
1.1 Ferroic properties . . . . .	5
1.2 Magnetoelectric effect . . . . .	7
1.3 Symmetry considerations . . . . .	10
1.4 Curie-Weiss extrapolation . . . . .	11
1.5 Nonlinear optics: Second Harmonic Generation . . . . .	11
<b>2 Hexagonal rare-earth manganites, HoMnO<sub>3</sub></b>	<b>15</b>
2.1 Crystal structure . . . . .	16
2.1.1 Influence of RE <sup>3+</sup> radius on crystal structure . . . . .	16
2.1.2 Hexagonal HoMnO <sub>3</sub> . . . . .	17
2.1.3 Ferroelectricity in hexagonal REMnO <sub>3</sub> . . . . .	18
2.2 Magnetic structure . . . . .	19
2.2.1 Spin arrangements . . . . .	21
2.2.2 Magnetic interactions . . . . .	22
2.3 Phase diagrams . . . . .	24
2.4 Magnetoelectric coupling . . . . .	26
<b>3 Experimental methods</b>	<b>29</b>
3.1 Sample preparation . . . . .	29
3.2 Sample characterization . . . . .	32
<b>4 Epitaxially grown HoMnO<sub>3</sub> thin films and capacitor layers</b>	<b>39</b>
4.1 Crystal structure . . . . .	39
4.2 Lattice parameters . . . . .	42
4.3 HoMnO <sub>3</sub> /YMnO <sub>3</sub> superlattices . . . . .	43

4.4	Capacitor trilayer . . . . .	46
4.5	Summary . . . . .	48
<b>5</b>	<b>Magnetic properties and phase diagram of films and single-crystals</b>	<b>49</b>
5.1	Temperature dependence of magnetization . . . . .	49
5.1.1	Curie-Weiss law . . . . .	49
5.1.2	Spin reorientation temperature, $T_{SR}$ . . . . .	51
5.1.3	Low temperature anomalies . . . . .	53
5.2	Magnetic field dependence of the magnetization . . . . .	60
5.2.1	Magnetic field-induced phase transition . . . . .	60
5.2.2	High-field transition of single-crystals . . . . .	64
5.3	The $\text{HoMnO}_3$ phase diagram . . . . .	65
5.4	Summary . . . . .	67
<b>6</b>	<b>Characterization by SHG</b>	<b>69</b>
6.1	Electric polar order . . . . .	69
6.2	Magnetic order . . . . .	72
6.3	Summary . . . . .	76
<b>7</b>	<b>Electrical properties</b>	<b>79</b>
7.1	Ferroelectric polarization . . . . .	79
7.2	Experimental difficulties with leakage current . . . . .	80
7.3	Summary . . . . .	82
<b>8</b>	<b>Conclusions and outlook</b>	<b>83</b>
	<b>References</b>	<b>86</b>

# Introduction

Multiferroics, the term introduced by Schmid [Schmid 94a], exhibit two or more primary ferroic properties simultaneously in the same phase. Occasionally, if some coupling exists among these ferroic order parameters, a new fascinating field comes into sight, i.e. the order parameters can be controlled in a joined way. This peculiar phenomenon has got much attention because of both its intrinsic physical nature and the potential applications [Spaldin 05, Eerenstein 06].

As ferroelectrics and magnets have served as crucial materials in industry for some decades, the coexistence of these two properties has attracted strong interest. The term *magnetoelectric (ME) effect* describes the dependence of the magnetization on an electric field or of the ferroelectric polarization on a magnetic field. This is obviously desirable for device miniaturization trends, because a single device can perform more than one task, and magnetization could be controlled *power-less*.

Some possible applications of magnetoelectric materials have been proposed already more than three decades ago [Wood 74]. However, the attempts to design multiferroics that combine ferromagnetism and ferroelectricity in the same phase, in particular those working at room temperature, have been unexpectedly difficult. The smallness of the ME effect and the rareness of ME materials has stagnated the investigations into this topic.

Recently, a flurry of research about ME effects has been triggered again, because of the improved characterization techniques and newly discovered compounds which have a strong ME coupling [Fiebig 05a]. The search for multiferroic magnetoelectric materials is categorized into two fields. One is the designed composite materials, such as multilayers. For instance, when ferroelectric and ferromagnetic layers are combined, a large magnetoelectric coefficient can be achieved through the interplay of these two layers [Ryu 01, Dörr 07, Ramesh 07]. The other is searching for single-phase materials. Since fundamental restrictions for the coexistence of ferroelectricity and magnetism have been revealed by theoretical works [Hill 00, Hill 02, Khomskii 06], further mechanisms for the ME effect have been

proposed [Ederer 04, Khomskii 06].  $\text{TbMnO}_3$  [Kimura 03] and  $\text{TbMn}_2\text{O}_5$  [Hur 04] are examples of single-phase multiferroics. These new candidates offer very good access to explore the fundamental nature of magnetoelectric interactions. The current trend for single phase multiferroics is summarized precisely in recent reviews [Prellier 05, Eerenstein 06, Cheong 07].

The hexagonal rare earth manganites with a chemical composition of  $\text{REMnO}_3$  ( $\text{RE}^{3+} = \text{Lu} - \text{Ho}, \text{Y}$ ) form one group of single-phase multiferroics. Among these,  $\text{HoMnO}_3$  attracts much interest because of its unusual interplay between the ferroelectric and magnetic properties.  $\text{HoMnO}_3$  turned out to be a promising single phase multiferroic due to its large magnetoelectric coupling. In this compound, it is observed that the magnetic phase can be reversibly controlled by an external electric field [Lottermoser 04b]. Furthermore, the dielectric permittivity is influenced by magnetic phase transitions [Lorenz 04a, Yen 05]. These observations reveal a strong coupling between the ferroic orders.

Recently, considerable experimental progress has been made in understanding the physical properties of hexagonal  $\text{HoMnO}_3$  in various ways, e.g. by neutron diffraction [Muñoz 01, Vajk 05], non-linear optics (Second Harmonic Generation; SHG) [Fröhlich 99, Fiebig 02, Fiebig 03], and magnetic and dielectric properties [Sugie 02, Lorenz 05] investigations. Most of these experiments have been done with single-crystal samples or bulk sintered polycrystalline samples.

The aim of this work is to prepare and to characterize multiferroic  $\text{HoMnO}_3$  thin films. When this work had been started in 2005, nothing was published about  $\text{HoMnO}_3$  films. Thus, the fabrication of high quality epitaxial thin films was the starting point. Investigations of the low temperature magnetic properties and magnetoelectric behavior of  $\text{HoMnO}_3$  thin films in comparison with single-crystals are the main objectives of this thesis work.

Chapter 1 and chapter 2 are devoted to background knowledge and a literature survey of  $\text{HoMnO}_3$ . In chapter 1, the fundamental concepts and definitions for multiferroics and magnetoelectrics are introduced. The symmetry classification of hexagonal  $\text{HoMnO}_3$  and the magnetic interactions are briefly addressed. Further, fundamentals of magnetic and magneto-optical properties studied in this work are described.

In chapter 2, the literature on the structural and physical properties of rare-earth manganites, especially  $\text{HoMnO}_3$  single-crystals, is examined. This chapter explains the hexagonal structure, the origin of ferroelectricity as well as magnetic orders. The magnetic phase diagram and direct proofs of magnetoelectric coupling in  $\text{HoMnO}_3$



are reviewed.

Chapter 3 describes the experimental methods from film preparation to magnetic and ferroelectric properties. The pulsed laser deposition chamber and the deposition conditions are discussed. The principles and set-ups of the various film characterization methods are explained.

From chapter 4 to chapter 7, the results obtained from the film investigations are summarized. In chapter 4, the process for finding the optimized deposition conditions and the structural properties of films of varied thickness are shown in detail. The lattice parameter variation with the film thickness is discussed. The superlattice structure of  $(\text{HoMnO}_3/\text{YMnO}_3)_{30}$  and a capacitor trilayer with a Pt bottom layer is introduced.

Magnetic properties of thin films are described and compared to single-crystals in chapter 5. In the end, an approximate diagram is constructed for both directions of the magnetic field. The differences between films and single-crystals with respect to the phase diagram are discussed.

In chapter 6, results from SHG investigations performed on the films in collaboration with the group of M. Fiebig are summarized.

The ferroelectric polarization measurements of  $\text{HoMnO}_3$  films at room temperature is followed in chapter 7. The ferroelectric switching is shown and the leakage current problem is discussed.



## Chapter 1

# Fundamentals

According to K.Aizu [Aizu 70], “a crystal is referred to as being *ferroic* when it has two or more orientation states in the absence of a magnetic field, electric field, or mechanical stress, and can shift from one state to another of these states by means of magnetic field, electric field, mechanical stress, or a combination of these”. The ferroic properties mentioned above are ferromagnetism, ferroelectricity and ferroelasticity, respectively, and are called *primary* ferroic properties. H. Schmid suggested one general nomenclature for the materials showing two or more primary ferroic properties, *multiferroics* [Schmid 94a]. These primary ferroic properties may couple more or less with each other. Among these multiferroics, when the ferroelectric order and the (anti-)ferromagnetic order are coupled to each other, i.e. ferroelectric order can be controlled by applied magnetic field  $\mathbf{H}$  or (anti-)ferromagnetic order can be controlled by electric field  $\mathbf{E}$ , then the materials are called *magnetoelectrics*.

## 1.1 Ferroic properties

### Ferromagnetism

Atoms contain many electrons, each spinning about its own axis and moving in its own orbit. Magnetic moment comes from two kind of electron motion; orbital and spin. The magnetic moment of the atom is the vector sum of all its electronic moments. The interaction between ferromagnetic moments of two ions (i and j) is often represented by a Heisenberg exchange Hamiltonian [Heisenberg 28]:

$$\mathbf{H}_{ij} = -2J_{ij}(\mathbf{S}_i \cdot \mathbf{S}_j) \quad (1.1)$$

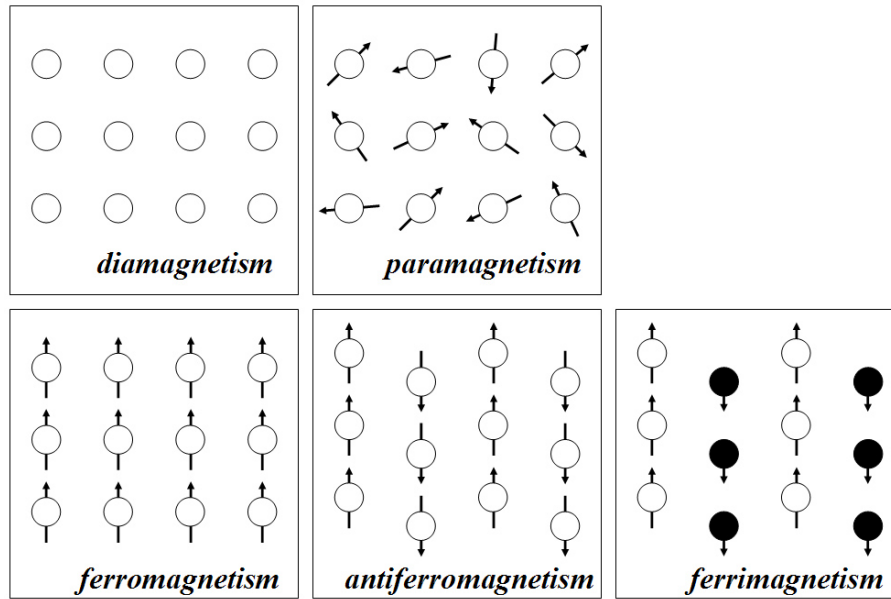


Figure 1.1: Five kinds of magnetic order systems.

where the exchange parameter  $\mathbf{J}_{ij}$  is positive for ferromagnetic, and negative for antiferromagnetic interaction.

Five different kinds of magnetic systems can be defined as in Fig.1.1. If the magnetic moments of all the electrons in one atom are such oriented that they cancel each other, then the atom as a whole has no net magnetic moment. This is called *diamagnetism*. The magnetization of a diamagnet originates from atomic electron currents according to Faraday's induction law and doesn't have a temperature or magnetic field dependence. If the cancelation of electronic moments is only partial, then the atom is left with a net magnetic moment. Materials composed of atoms of this kind are *para-*, *ferro-*, **antiferro-**, or *ferrimagnetic* (Fig.1.1). The last three have ordered arrays of magnetic moments.

Ferromagnets and ferrimagnets have a spontaneous magnetic moment. A ferrimagnet has a similar arrangement of magnetic moments as an antiferromagnet with two sublattices, but in a ferrimagnet the magnetic moments of the two sublattices do not completely cancel retaining a net magnetic moment. An antiferromagnet has ordered moments which align in an antiparallel arrangement, i.e. two sublattices of antiparallel direction, with zero net magnetic moment at temperatures below the order temperature or Néel temperature ( $T_N$ ). Also more complex arrangements are found such as *triangular* or *spiral* magnetic structures. Hexagonal  $\text{HoMnO}_3$  has a

triangular antiferromagnetic order, where the spins are located with an angle of  $120^\circ$  to each other. This will be discussed in chapter 2.

## Ferroelectricity

When an electric field is applied to an insulator, the material produces electric dipoles by polarization. The electric dipole moment  $\mathbf{p}$  can be expressed as the sum of all products between charge and distance of charges.

$$\mathbf{p} = \sum_i q_i \mathbf{r}_i \quad (1.2)$$

The dipole moment  $\mathbf{p}$  per unit volume or the density of the dipole moment is called the polarization  $\mathbf{P}$ . In some materials, the dipole moments exist without an applied electric field as so-called permanent dipoles, and these are the origin of spontaneous polarization  $\mathbf{P}_S$ . The material which exhibits spontaneous polarization, the direction of which can be switched by an external electric field, is called a ferroelectric. In ferroelectrics, an electric displacement  $\mathbf{D}$  can be defined when an external electric field  $\mathbf{E}$  is applied, as

$$\mathbf{D} = \varepsilon_0 \mathbf{E} + \mathbf{P} \quad (1.3)$$

where  $\varepsilon_0$  denotes the vacuum permittivity. In the ferroelectric state, for example in the perovskite structure, the center of positive charge is shifted relative to the negative charge. This displacement is essential to produce a polarization  $\mathbf{P}$ . Ferroelectrics have a transition temperature or Curie temperature  $T_C$  at which the crystal changes from the low temperature polarized state to the high temperature unpolarized state, since thermal motion tends to destroy the ferroelectric order.

## 1.2 Magnetoelectric effect

### History and definition

In 1894, Pierre Curie proposed a linear magnetoelectric (ME) effect based on symmetry arguments: materials may exist which can be polarized electrically by means of a magnetic field  $\mathbf{H}$ , and magnetically by means of an electric field  $\mathbf{E}$  [Curie 94]. Since then, several experimental investigations have been done to discover the ME effect [O'Dell 70]. Finally, Landau and Lifshitz came to the first detailed theoretical description, that a linear relationship between the electric and magnetic field in a

substance can in principle exist for certain types of magnetic crystal symmetries [Landau 84].

The ME effect can be described by the thermodynamic potential free energy  $\mathbf{F}$ , in which the magnetization  $\mathbf{M}$  and the electric polarization  $\mathbf{P}$  are replaced as independent variables by the magnetic field  $\mathbf{H}$  and the electric field  $\mathbf{E}$ , respectively [Bertaut 71, Rado 74, Fiebig 05a]. This thermodynamic description is an appropriate way to take into account the symmetry properties of the material. Expansion of the free energy in terms of  $\mathbf{E}$  and  $\mathbf{H}$  gives:

$$\begin{aligned} F(E, H) &= F_0 - P_i^S E_i - M_i^S H_i \\ &\quad - \frac{1}{2} \varepsilon_o \varepsilon_{ij} E_i E_j - \frac{1}{2} \mu_o \mu_{ij} H_i H_j - \alpha_{ij} E_i H_j \end{aligned} \quad (1.4)$$

where  $F_0$  is independent of  $\mathbf{E}$  and  $\mathbf{H}$ .  $\mathbf{P}^S$  and  $\mathbf{M}^S$  denote the spontaneous polarization and magnetization whereas  $\varepsilon_{ij}$ ,  $\mu_{ij}$  are electric permittivity and magnetic permeability, respectively.  $\alpha_{ij}$  indicates the linear ME susceptibility tensor.

The derivatives of  $\mathbf{F}$  with respect to  $\mathbf{E}_i$  and  $\mathbf{H}_i$  define the polarization and the magnetization, as

$$\begin{aligned} P_i(E, H) &= - \frac{\partial F}{\partial E_i} \\ &= P_i^S + \varepsilon_o \varepsilon_{ij} E_j + \alpha_{ij} H_j \end{aligned} \quad (1.5)$$

$$\begin{aligned} M_i(E, H) &= - \frac{\partial F}{\partial H_i} \\ &= M_i^S + \mu_o \mu_{ij} E_j + \alpha_{ij} E_i \end{aligned} \quad (1.6)$$

Eq.1.5 and Eq.1.6 show that polarization and magnetization both contain a linear ME susceptibility,  $\alpha_{ij}$ . The ME susceptibility tensor  $\alpha_{ij}$  corresponds to the induction of polarization by a magnetic field, or to magnetization by an electric field which is designated as the *linear* ME effect. The number of independent components of the ME susceptibility tensor is determined by the crystallographic and the magnetic symmetry considerations [Schmid 73].

Right after Landau and Lifshitz, Dzyaloshinskii [Dzyaloshinskii 60] predicted one specific example of antiferromagnetic chromium oxide,  $\text{Cr}_2\text{O}_3$ , which should show the ME effect from symmetry considerations. Astrov first observed the electrically induced ME effect in  $\text{Cr}_2\text{O}_3$  experimentally, i.e. the appearance of a magnetization  $\mathbf{M}$  after the application of an electric field  $\mathbf{E}$  (for  $T \geq 250$  K [Astrov 60] and  $T \geq 100$  K [Folen 61]). According to their measurements, the ME effect is zero at  $T \geq$

306 K. Since the Néel temperature of  $\text{Cr}_2\text{O}_3$  is known to be 307 K [McGuire 56], it appears that the ME effect does not exist in the paramagnetic region, in agreement with the symmetry considerations of Landau and Lifshitz [Landau 84]. In addition to the electric field induced ME effect, Rado *et al.* observed the magnetically induced ME effect for the first time [Rado 61]. Further, the first observation of ME effect switching with a strong ME coupling was observed in nickel-iodine boracite ( $\text{Ni}_3\text{B}_7\text{O}_{13}\text{I}$ ) [Ascher 66].

### Magnetoelectric coefficient: $\alpha_{ij}$

The linear ME coefficient  $\alpha_{ij}$  is the critical parameter for the interaction of magnetic and electric orders. W.F. Brown *et al.* calculated an upper bound for the magnitude of  $\alpha_{ij}$  from the ordinary electric and magnetic susceptibilities by considering the change in the free energy when electric and magnetic fields are simultaneously applied to a ME material [Brown 68]. The upper bound of the ME coefficient can be expressed by

$$\alpha_{ij} < (\varepsilon_{ii}\mu_{jj})^{1/2} \quad (1.7)$$

where  $\varepsilon_{ii}$  and  $\mu_{jj}$  are elements of the electric permittivity and magnetic permeability tensors, respectively. This inequality must be satisfied in order to insure that the system is thermodynamically stable.

As the upper bound is given by the geometric means of the magnetic and electric susceptibilities, it thus appears that the chances of finding substances with large ME susceptibilities will be better in ferromagnetic than in antiferromagnetic materials. It may also be concluded that materials which are both ferromagnetic and ferroelectric, or, at least, have a large permeability and permittivity at the same time may have relatively large ME susceptibilities.

Many attempts have been devoted to find single-phase ME materials with large ME coefficient. The most known examples of single-phase magnetoelectrics, however, are antiferromagnets. These antiferromagnets exhibit weak ferromagnetism. A slight canting of the spins or a slight distortion of the lattice structure leads to a net moment. These and other magnetically ordered materials may (or may not, depending on the magnetic point group symmetry [Birss 64]) exhibit the ME effect. The non-vanishing components of the ME susceptibility tensor  $\alpha_{ij}$  indeed can be predicted on the basis of the magnetic point group of a given crystal, which is why symmetry considerations on magnetoelectrics are crucial.

### 1.3 Symmetry considerations

According to the crystal's lattice structure, every crystal can be classified into 32 point groups. In addition, with the consideration of the magnetic symmetry, 90 magnetic point groups can be distinguished. Therefore, there are 122 point groups (also known as Shubnikov magnetic point groups) as a whole including non-magnetic point groups [Landau 84]. The magnetic point groups are written in bold face to distinguish from non-magnetic point groups.

Among these 122 magnetic point groups, it is known that 31 point groups display spontaneous polarization  $\mathbf{P}_S$  (pyro-, ferri-, and ferroelectricity) and 31 point groups allow spontaneous magnetization  $\mathbf{M}_S$  (ferri- and ferromagnetism). To show multi-ferroic properties, i.e.  $\mathbf{P}_S$  as well as  $\mathbf{M}_S$  simultaneously in the same phase, only 13 intersecting point groups can be candidates as listed below [Birss 64, Schmid 94b].

**1, m, m, 2, 2, mm2, mm2, 4, 4mm, 3, 3m, 6, 6mm**

However, according to symmetry considerations it is not necessary to have a spontaneous polarization  $\mathbf{P}_S$  or a spontaneous magnetization  $\mathbf{M}_S$  to show ME coupling. So it is possible to distinguish the ME magnetic point groups besides the limitations for simultaneous  $\mathbf{P}_S$  and  $\mathbf{M}_S$ . There are a total of 58 magnetic point groups in which the linear ME effect is allowed (refer to [Birss 64, O'Dell 70, Schmid 73]).

#### Space group, $P6_3cm$

Hexagonal  $\text{HoMnO}_3$  has a space group  $P6_3cm$  with a point group  $6mm$ . This space group  $P6_3cm$  can represent five magnetic space groups depending on the spin order of the atoms. Among these five, four different space groups have been detected in  $\text{HoMnO}_3$ , i.e.  $P6_3cm$ ,  $P\bar{6}_3cm$ ,  $P\bar{6}_3cm$  and  $P6_3cm$  (see §2.2). Here, the underbar denotes the time reversal transformation. Phase transitions between these four magnetic space groups are distinguished by in-phase and anti-phase rotations of the spins of the magnetic Mn lattice.

According to the symmetry considerations, this space group has a spontaneous electric polarization for all magnetic point groups. The spontaneous magnetization, however, can exist only in  $P\bar{6}_3cm$ , not in the others. Thus, the magnetic order is ferromagnetic in  $P\bar{6}_3cm$  and antiferromagnetic in the other magnetic space groups. The ME susceptibility does not vanish in two magnetic point groups,  $P\bar{6}_3cm$  and  $P6_3cm$ . Even though the linear ME susceptibility can exist only in two point



groups, the higher-order or non-linear ME effects can exist in all above mentioned point groups by symmetry [Birss 64, Schmid 73].

## 1.4 Curie-Weiss extrapolation

Magnetic materials become paramagnetic above the ordering temperature. Pierre Curie found that the susceptibility  $\chi$  varies inversely with the absolute temperature for paramagnets, as

$$\chi_p = C/T \quad (1.8)$$

This is the famous *Curie's law*, and  $C$  is the Curie constant. It was later shown that Curie's law is only a special case of a more general law, the so-called *Curie-Weiss law*, which many paramagnets obey:

$$\chi_p = C/(T - \theta) \quad (1.9)$$

where  $\theta$  is the paramagnetic Curie temperature, with the dimension of the absolute temperature and equal to zero for paramagnetic substances. If  $1/\chi$  is plotted vs.  $T$  for a paramagnet, extrapolating to  $1/\chi = 0$  gives  $\theta$ . The  $\theta$  is proportional to the molecular field [Cullity 72]. Therefore  $\theta$  can be postulated as a measure of the strength of the interaction of magnetic moments.

A positive value of  $\theta$  indicates that the molecular field tends to align the magnetic moments parallel to one another (ferromagnetism dominant) and to the applied field. If  $\theta$  is negative, the molecular field opposes the applied field and tends to decrease the susceptibility (antiferromagnetism dominant). When  $\theta$  is zero, the molecular field constant is also supposed to be zero. This means that the interactions between atoms effectively vanish or compensate [Cullity 72].

## 1.5 Nonlinear optics: Second Harmonic Generation

Nonlinear optics deal with nonlinear interactions of light with matter. Nonlinear optical processes reveal novel information about the details of the electronic and magnetic structures of solids [Fiebig 05b]. A Second Harmonic Generation (SHG) is the simplest case of nonlinear optics. It has arisen as an effective technique for the investigation of magnetoelectrics, because it is sensitive to the symmetry of a magnetic structure as well as to the ferroelectric polar order. With this ability, it is often applied to the investigation of multiferroics in which more than two ferroic

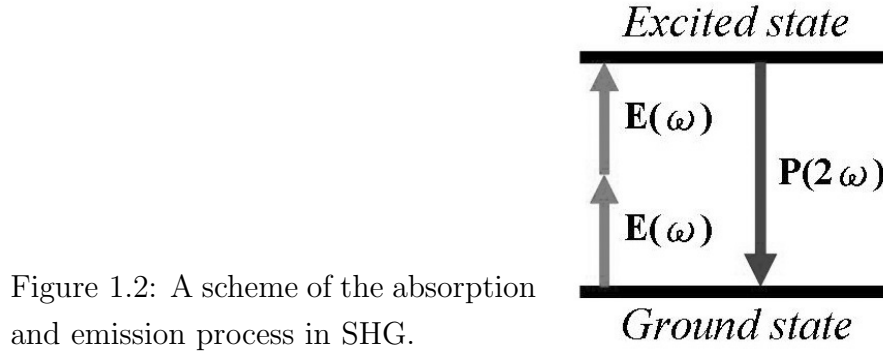


Figure 1.2: A scheme of the absorption and emission process in SHG.

orders coexist. How the SH signal arises from the interaction of a light wave with material is described below.

Electromagnetic waves traveling through a material induce an electric polarization  $\mathbf{P}_i$ . It can be expressed by the electric field  $\mathbf{E}_i$  and the frequency  $\omega_i$  of the incident light as:

$$P_i(\omega_i) = \underbrace{\varepsilon_0 \chi_{ij}^{(1)} E_j(\omega_j)}_{P_i^L} + \underbrace{\varepsilon_0 \chi_{ijk}^{(2)} E_j(\omega_j) E_k(\omega_k) + \dots}_{P_i^{NL}} \quad (1.10)$$

$P_i^L$  and  $P_i^{NL}$  denote the linear polarization and the nonlinear polarization, respectively. For a small electric field, the linear polarization usually gives a good approximation to describe the phenomenon. In contrast, for a large field (more than  $10^4$  V/m) the higher order terms or nonlinear terms become dominant [Shen 03].

In a nonlinear process, the frequency  $\omega_i$  of the polarization  $\mathbf{P}_i^{NL}$  has the following relation:

$$\omega_i = \omega_j \pm \omega_k \pm \dots \quad (1.11)$$

In SHG, the two electric fields  $\mathbf{E}_j$  and  $\mathbf{E}_k$  have the same frequency. As a result, the frequency of the polarization  $\mathbf{P}_i^{NL}$  is twice the frequency of the incoming light. It is expressed as

$$\omega_i = \omega_j + \omega_k \quad (1.12)$$

where  $\omega_j = \omega_k = \omega$  and therefore  $\omega_i = 2\omega$  [Shen 03]. This leads to  $\mathbf{P}_i^{NL} = \mathbf{P}_i(2\omega)$ .

The SHG signals macroscopically originate from the two-photon absorption and one-photon emission process as shown in Fig.1.2. In the two-photon absorption processes, two photons are simultaneously absorbed by an electron to reach an excited state. The incoming light, with an electric field  $\mathbf{E}$  of frequency  $\omega$ , undergoes interactions inside the material, giving SHG signals, for instance, an electrically induced polarization  $\mathbf{P}_i(2\omega)$  and a magnetically induced polarization  $\mathbf{M}_i(2\omega)$  with

Table 1.1: The non-zero crystallographic and magnetic SHG tensor components allowed in hexagonal HoMnO<sub>3</sub> for the case of a point group  $6mm$  and a space group  $P6_3cm$  [Fiebig 05b].

Space group	Tensor components
For electric SHG , $\chi_{ijk}^{ED}$	
<b><math>P6_3cm</math></b>	$\chi_{xxz}=\chi_{xzx}=\chi_{yyz}=\chi_{yzy}$ , $\chi_{zxx}=\chi_{zyy}$ , $\chi_{zzz}$
For magnetic SHG , $\chi_{ijk}^{MD}$	
<b><math>P6_3cm</math></b>	$\chi_{yyy}=-\chi_{yxx}=-\chi_{xyx}=-\chi_{xxy}$
<b><math>P6_3cm</math></b>	$\chi_{xxx}=-\chi_{xyy}=-\chi_{yxy}=-\chi_{yyx}$
<b><math>P6_3cm</math></b>	$\chi_{xyz}=\chi_{xzy}=-\chi_{yxz}=-\chi_{yzx}$
<b><math>P6_3cm</math></b>	$\chi_{xxz}=\chi_{xzx}=\chi_{yyz}=\chi_{yzy}$ , $\chi_{zxx}=\chi_{zyy}$ , $\chi_{zzz}$

a doubled frequency. These interactions are sensitive to the crystal structure and magnetic order of the material.  $\mathbf{P}_i(2\omega)$  and  $\mathbf{M}_i(2\omega)$  are respectively expressed as:

$$P_i(2\omega) \propto \chi_{ijk}^{ED} E_j(\omega) E_k(\omega) \quad (1.13)$$

$$M_i(2\omega) \propto \chi_{ijk}^{MD} E_j(\omega) E_k(\omega) \quad (1.14)$$

$\mathbf{P}_i(2\omega)$  and  $\mathbf{M}_i(2\omega)$  are direct observables of the electric and magnetic order of the material, respectively. For this reason, SHG is a powerful technique for the investigation of magnetoelectrics, which have both electric and magnetic order. SHG can also distinguish antiferromagnetic ordering, that is generally present in most multiferroics. Magnetic SHG is especially useful in the case of antiferromagnets, where linear magneto-optical methods such as the Faraday effect and the Kerr effect fail because of the absence of a macroscopic magnetization.

In SHG, non-vanishing  $\mathbf{P}_i(2\omega)$  requires a breaking of space inversion symmetry, so it is allowed only in noncentrosymmetric materials.  $\mathbf{M}_i(2\omega)$  is sensitive to a breaking of time reversal symmetry. This contribution can be used to probe magnetic spin structures and magnetic phase transitions.

As shown in Eq.1.13 and Eq.1.14, the nonlinear third rank tensor susceptibilities  $\chi_{ijk}^{ED}$  and  $\chi_{ijk}^{MD}$  play an important role for the SHG signal.<sup>†</sup>  $\chi_{ijk}^{ED}$  is a time-invariant

<sup>†</sup>The indices  $i, j$  and  $k$  of  $\chi_{ijk}$  correspond to the crystal axes  $x, y$  and  $z$ . The first index means the polarization direction of the outgoing light. The last two indices indicate the polarization direction of the incoming light.

tensor which is responsible for the crystallographic contribution.  $\chi_{ijk}^{MD}$  is a time-noninvariant tensor responsible for the spin-dependent contribution to the nonlinear polarization. This contribution is allowed only below the magnetic ordering temperature where the time-reversal symmetry is broken by magnetic long range order. Since  $\chi_{ijk}^{MD}$  is related to the magnetic point group, it is possible to get information about the spin structure by means of polarization- and temperature-dependence SH spectroscopy [Fröhlich 99].

The tensor components of  $\chi_{ijk}^{ED}$  and  $\chi_{ijk}^{MD}$  are uniquely defined by the crystallographic and magnetic structure of a material. According to the von Neumann principle, the physical properties should be invariant when the crystal symmetry is invariant under the symmetry operations [Birss 64]. Therefore, the nonlinear susceptibility tensor component  $\chi_{ijk}$  should have certain forms of symmetry that reflect the structural symmetry of the material. The available tensor components of the hexagonal HoMnO<sub>3</sub> from the ferroelectric polar structure and the magnetic phases are listed in Tab.1.1. With the non-vanishing tensor components of each phase, the SHG experiment can investigate the electric polar order and magnetic structure as well as the phase transitions [Fiebig 05b].

## Chapter 2

# Hexagonal rare-earth manganites, $\text{HoMnO}_3$

The hexagonal rare-earth manganites with a chemical composition  $\text{REMnO}_3$  (RE = trivalent rare-earth cation, Ho-Lu, Y) possess a specific nature arising from the strong interplay between the  $3d$  electrons of the transition metal  $\text{Mn}^{3+}$  and the  $4f$  electrons of the rare earth ion  $\text{RE}^{3+}$ .  $\text{REMnO}_3$  both the hexagonal and the perovskite-type structure have attracted interest so far because of their two outstanding properties, i.e. colossal magnetoresistance (CMR) and multiferroicity.

The CMR effect is a phenomenon of spin-dependent electron transport that leads to conductivity changes by several orders of magnitude at the ferromagnetic Curie temperature. This has been the subject of intense research in (doped and undoped)  $\text{REMnO}_3$  manganites which have a distorted perovskite or orthorhombic structure [von Helmolt 93].

On the other hand, multiferroic properties, or the combination of ferroelectric and magnetic ordering was observed in  $\text{REMnO}_3$  (RE=Eu-Lu, Y, Bi). The mutual interference and the possible correlation between the order parameters are of an academic as well as an application research interest.

In this chapter, the various physical properties of the hexagonal rare-earth manganites will be discussed. Among the  $\text{REMnO}_3$  series,  $\text{HoMnO}_3$ , which turned out to be multiferroic showing strong magnetoelectric coupling [Lottermoser 04b] with large polarization ( $P = 5.6 \mu\text{C}/\text{cm}^2$ ) and effective magnetic moment ( $\mu_{eff} = 11.4 \mu_B$ ) [Fujimura 96, Lorenz 05], will be mainly addressed.

## 2.1 Crystal structure

### 2.1.1 Influence of $\text{RE}^{3+}$ radius on crystal structure

The rare-earth manganites,  $\text{RE}\text{MnO}_3$ , crystallize in the hexagonal or orthorhombic structure depending on the radius of the rare-earth ion  $\text{RE}^{3+}$ . The large ionic radius rare-earth ions (La and Ce-Dy) crystallize in an orthorhombic (distorted perovskite) structure. In contrast, the small ionic radius rare-earth ions (Ho-Lu and Y, Sc) crystallize in a hexagonal structure [Yakel 63]. This is because the decreasing size of the rare-earth series cations with increasing atomic number would decrease the stability of an orthorhombic lattice.

This tendency was shown quantitatively by the calculation of the thermodynamic free energy for crystallization by Graboy *et al.* [Graboy 03]. As it is shown in Fig.2.1, the  $\text{Ho}^{3+}$  ion is located at the border of the hexagonal and the orthorhombic structures. The potential energy difference between hexagonal and orthorhombic structure for  $\text{Ho}^{3+}$  is very small. This indicates that  $\text{HoMnO}_3$  can also crystallize in the orthorhombic structure as a metastable state [Brinks 01, Lorenz 04b]. The

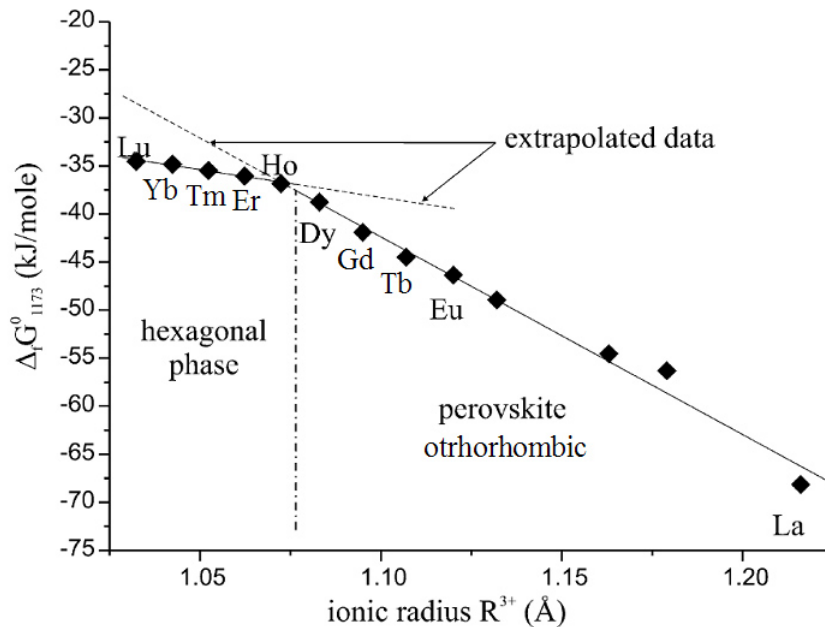


Figure 2.1: Free energy of bulk  $\text{RE}\text{MnO}_3$  formation from  $\text{RE}_2\text{O}_3$  and  $\text{Mn}_2\text{O}_3$  at 1173 K. The change of crystal structure depending on the radius of the  $\text{RE}^{3+}$  ion is quantitatively shown [Graboy 03].

scope of this dissertation is confined to the thermodynamically stable hexagonal structure.

### 2.1.2 Hexagonal $\text{HoMnO}_3$

Hexagonal  $\text{HoMnO}_3^\dagger$  is ferroelectric with a high ferroelectric Curie temperature  $T_{CE} = 875$  K [Fujimura 96]. In the ferroelectric state,  $\text{HoMnO}_3$  has a space group  $P6_3cm$ . Figure 2.2 shows the crystal structure of  $\text{HoMnO}_3$  in the ferroelectric state.

In this structure, one Mn atom and five adjacent oxygen atoms form a  $\text{MnO}_5$  trigonal bipyramid. Each Mn atom occupies the center of a triangular bipyramid whose vertices are oxygen atoms. The rare-earth ions are located in layers between the bipyramid sheets. The crystal structure is an alternative stacking of  $\text{MnO}_5$  and rare-earth atom layers along the hexagonal  $c$ -axis.

The  $\text{MnO}_5$  bipyramids share their corners with neighboring bipyramids to form a triangular lattice in the basal  $ab$  plane, where, each oxygen ion links three Mn ions, and each Mn ion is surrounded by three oxygens (Fig.2.2 (left)). In this triangular

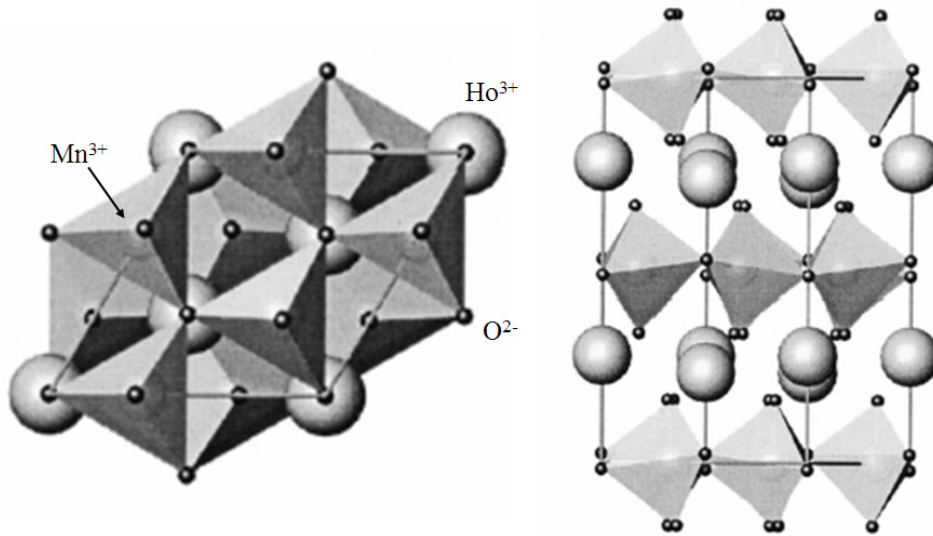


Figure 2.2: Hexagonal structure of  $\text{HoMnO}_3$  in the ferroelectric state [Lonkai 03]. (left) Top view ( $ab$  plane), (right) side view (along  $c$ -axis). The big spheres indicate  $\text{Ho}^{3+}$ , the small spheres  $\text{O}^{2-}$ .  $\text{Mn}^{3+}$  lies in the middle of the trigonal bipyramids.

<sup>†</sup>In this dissertation from now on, if the term ‘ $\text{HoMnO}_3$ ’ stands alone, it basically indicates hexagonal  $\text{HoMnO}_3$ .

arrangement the Mn atoms constitute a frustrated spin ordering (see §2.2.1). The Mn sublattice has a six-fold symmetry as a whole. This is because one Mn layer (at  $z = 0$ ) forms one triangle and the next Mn layer (at  $z = c/2$ ) forms a triangle rotated by  $60^\circ$ .

### 2.1.3 Ferroelectricity in hexagonal $\text{REMnO}_3$

The ferroelectricity in hexagonal  $\text{REMnO}_3$  was firstly discovered by Bertaut *et al.* in 1963 [Bertaut 63a]. Since then, precise structural investigations have been employed to find the origin of ferroelectricity in hexagonal rare-earth manganites [Yakel 63, Van Aken 01, Van Aken 04, Nénert 07]. As a result, it is known that ferroelectricity is geometrically driven by the displacement between  $\text{RE}^{3+}$  and  $\text{O}^{2-}$  as a result of a structural phase transition.

Hexagonal  $\text{REMnO}_3$  undergoes a structural phase transition from a high tem-

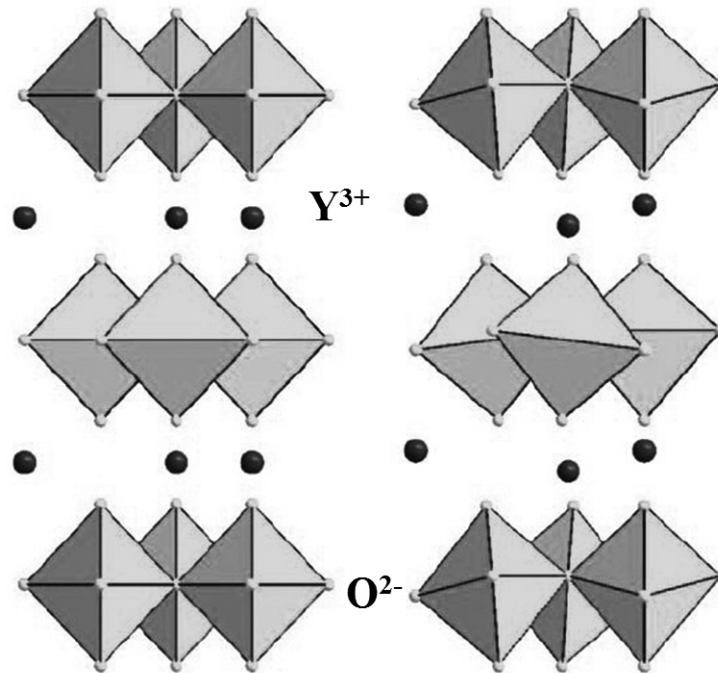


Figure 2.3: High-temperature centrosymmetric (left) and low-temperature ferroelectric structure (right) of  $\text{YMnO}_3$ . At low temperatures, the oxygen-polyhedra are rotated collectively, accompanying the displacement of  $\text{Y}^{3+}$  along the  $c$ -axis. The displacement of  $\text{Y}^{3+}$  ions relative to the oxygen anions produces an electric dipole moment [Ederer 05].



perature paraelectric phase (space group  $P6_3/mmc$ ) to the low temperature ferroelectric phase (space group  $P6_3cm$ ) as the temperature decreases. Figure 2.3 shows the structures of these two states in  $YMnO_3$ .  $YMnO_3$  may serve as representative of all hexagonal rare-earth manganite systems, especially for  $HoMnO_3$  with its similar size of rare-earth ion and lattice parameters.

In the paraelectric phase (above the ferroelectric Curie temperature,  $T_{CE}$ ), all ions are confined to planes parallel to the  $ab$  plane. This arrangement of atoms makes the structure centrosymmetric. Below the ferroelectric transition temperature, however, two major atomic displacements take place in the crystal structure from the centrosymmetric  $P6_3/mmc$  to the ferroelectric  $P6_3cm$ . The first change is the collective rotation of the  $MnO_5$  bipyramids. The second change is the vertical shift of the rare-earth ions away from the high-temperature mirror plane [Lonkai 04, Van Aken 04]. In this distortion, the Mn ions remain very close to the center of the oxygen bipyramids, giving no significant contributions to the polarization. The displacement of the rare-earth ions along the  $c$ -axis plays a crucial role for inducing ferroelectricity. The polar direction, therefore, is parallel to the  $c$ -axis. The value of the spontaneous polarization of hexagonal  $HoMnO_3$  is known to be  $5.6 \mu C/cm^2$  [Fujimura 96].

## 2.2 Magnetic structure

The magnetic structure of  $REMnO_3$  was first investigated in the middle of the 1960's by Bertaut *et al.* [Bertaut 63b] and Koehler *et al.* [Koehler 64] by neutron diffraction experiments. Before these experiments, a theoretical work of the magnetic structure of the nickel-arsenide type crystals was published [Hirone 57]. Because  $NiAs$  has a compatible structure with  $REMnO_3$ , i.e. a hexagonal structure with six-fold sublattices, this work was a guideline for early magnetic structure studies. Hirone *et al.* suggested four possible spin orders in this structure: ferromagnetic, uniaxial antiferromagnetic and two triangular antiferromagnetic orders. Bertaut *et al.* and Koehler *et al.* argued that, among these four spin orders, only the two triangular antiferromagnetic ones could be possible in  $REMnO_3$  according to neutron diffraction experiments (Fig.2.4). These two triangular arrangements were named model  $\alpha$  and  $\beta$  depending on how the Mn layers at  $z = 0$  and  $z = c/2$  are coupled to each other.

As shown in Fig.2.4, model  $\alpha$  has a parallel arrangement between the  $z = 0$  and  $z = c/2$  layers, whereas model  $\beta$  has an antiparallel arrangement. The magnetic

space groups are determined by the combination of the relative spin directions in the two layers. The corresponding magnetic space groups of model  $\alpha$  are  $\underline{P6}_3\mathbf{cm}$  and  $\underline{P6}_3\mathbf{cm}$ . On the other hand,  $\underline{P6}_3\mathbf{cm}$  and  $\underline{P6}_3\mathbf{cm}$  belong to model  $\beta$ .

Even though the magnetic structure has been predicted theoretically and the triangular structure could be confirmed by neutron diffraction, the precise magnetic structure was controversial. Because it could not be distinguished easily by neutron diffraction whether the coupling between the  $z = 0$  and  $z = c/2$  layers is ferromagnetic or antiferromagnetic. Furthermore, it was not possible to properly discriminate the directions of the magnetic moments of the two triangular arrangements, e.g. the magnetic space groups  $\underline{P6}_3\mathbf{cm}$  and  $\underline{P6}_3\mathbf{cm}$ .

In recent years, magnetic structure determination became possible by new techniques of statistical analysis of neutron powder diffraction data [Muñoz 01, Lonkai 02, Vajk 05] or by the non-linear optical method of second harmonic generation (SHG)

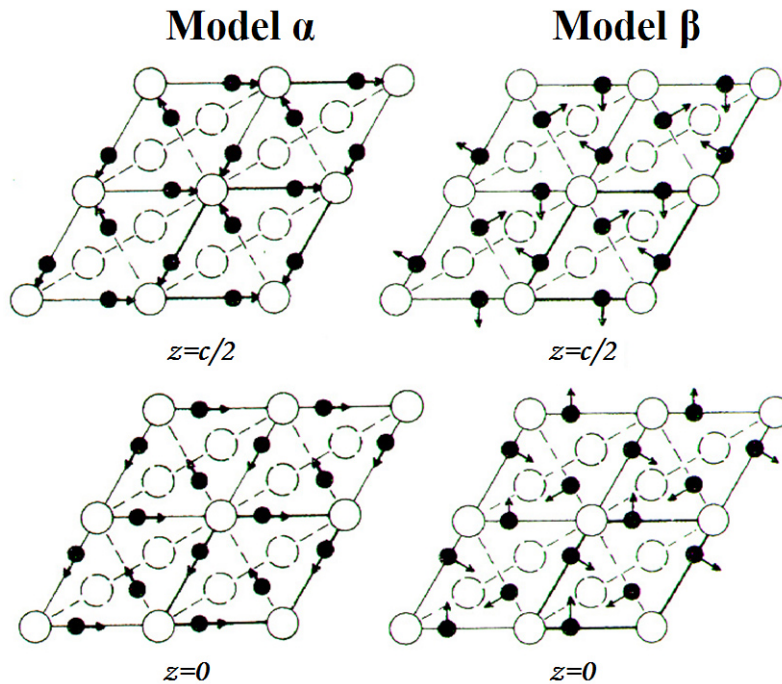


Figure 2.4: Two possible spin models named model  $\alpha$  and  $\beta$  by Bertaut *et al.* according to Mn spin ordering. Model  $\alpha$  has a parallel spin order in adjacent planes ( $z = 0$  and  $c/2$ ) and model  $\beta$  has an antiparallel spin order. Open and solid circles indicate rare-earth ions and Mn ions, respectively. Arrows mean spin order [Bertaut 63b].

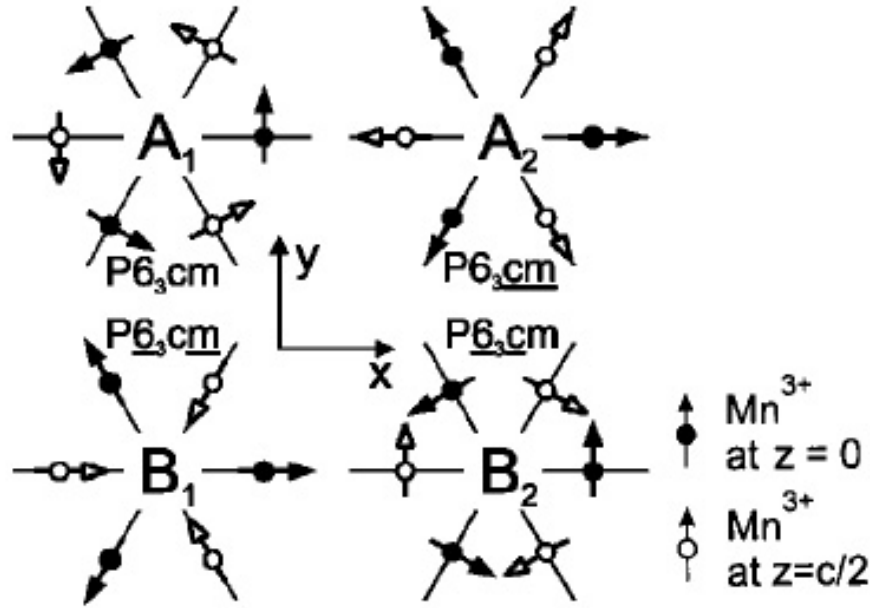


Figure 2.5: Four different types of magnetic ordering of the Mn sublattice in hexagonal  $\text{HoMnO}_3$  of the crystallographic space group of  $P6_3cm$  [Fiebig 02]. The magnetic space groups of  $P6_3cm$  ( $B_2$ ) and  $P6_3cm$  ( $B_1$ ) are coupled ferromagnetically (model  $\alpha$ ), on the other hand,  $P6_3cm$  ( $A_1$ ) and  $P6_3cm$  ( $A_2$ ) are coupled antiferromagnetically (model  $\beta$ ). The A and B representations correspond to the  $\beta$  and  $\alpha$  model, respectively.

[Fröhlich 99, Fiebig 02, Fiebig 03].

### 2.2.1 Spin arrangements

At the Néel temperature  $T_N = 76$  K, the antiferromagnetic long-range order of  $\text{Mn}^{3+}$  ions is established. The triangle structure of the  $\text{Mn}^{3+}$  sublattice produces *frustrated* antiferromagnetic order with a tilting angle of  $120^\circ$  between next-neighbor spins as depicted in Fig.2.4 and Fig.2.5.

Figure 2.5 shows possible arrangements of  $\text{Mn}^{3+}$  sublattices in  $\text{HoMnO}_3$ . The spins in all configurations are ordered antiferromagnetically but the symmetries are different. These spin arrangements (i.e. magnetic structures) are determined by the relative angle between the  $\text{Mn}^{3+}$  magnetic moment and the local  $x$ - or  $y$ -axis. For instance, the difference between  $P6_3cm$  and  $P6_3cm$  is that the spin orientation

is tilted by  $90^\circ$  [Fröhlich 99]. With this relative angle equal to  $0^\circ$  or  $90^\circ$  and two opposite relative orientations of the  $\text{Mn}^{3+}$  spins in adjacent planes at  $z = 0$  and  $z = c/2$  along the  $z$ -direction, the four principal magnetic structures of  $\text{HoMnO}_3$  are constructed as shown in Fig.2.5.

The spin rotation between the magnetic structures can occur through an *in-phase* or an *anti-phase* rotation of the  $\text{Mn}^{3+}$ , for which the direction of rotation is equal or opposite, respectively, in the adjacent basal  $\text{Mn}^{3+}$  planes. The rotation would be *in-phase* between the same model class, otherwise, it would be *anti-phase*.

$\text{HoMnO}_3$  shows successive magnetic structures as the temperature decreases. As investigated by SHG [Fiebig 02], the symmetry of  $P6_3cm$  is present above  $T_N$ . Just below  $T_N$ , the magnetic moments are aligned along the  $x$ -direction (i.e.  $\underline{P6_3cm}$ ) with anti-phase rotation. A spin reorientation transition of  $\text{Mn}^{3+}$  occurs at a certain temperature  $T_{SR} \sim 32 - 45$  K depending on the quality of samples or the experimental set-ups [Lorenz 04a]. At  $T_{SR}$ , the moments rotate in-phase within the basal plane towards the  $y$ -direction (i.e.  $\underline{P6_3cm}$ ). Below the ordering temperature of the Ho magnetic moments  $T_{Ho} \sim 5$  K, the magnetic moments rotate again anti-phase giving rise to the magnetic structure of  $\underline{P6_3cm}$  in zero electric or magnetic field.

Phase transitions take place when the magnetic structure changes. These phase transitions are not accompanied by a structural transition, the hexagonal structure remains stable. They are only related to the magnetic order which influences some physical properties, such as magnetization, the dielectric constant or the SH intensity.

## 2.2.2 Magnetic interactions

Although there may be some direct overlap of metal  $d$  orbitals, in a majority of metal oxides the magnetic coupling is mostly a result of indirect interactions, involving two metal atoms with an intervening oxygen atom. This indirect overlap is generally responsible for magnetic interactions in antiferromagnetic insulators and is known as *superexchange*. In many metal oxides the most significant interaction is that between two metal ions and an oxygen ion in a linear configuration.

Several superexchange paths exist in the  $\text{HoMnO}_3$  structure. First of all, the  $\text{Mn}^{3+}$  ( $3d^4$ ) sublattice exhibits  $\text{Mn}^{3+}-\text{O}^{2-}-\text{Mn}^{3+}$  *superexchange* paths in the basal  $ab$  plane and  $\text{Mn}^{3+}-\text{O}^{2-}-\text{O}^{2-}-\text{Mn}^{3+}$  inter-plane *super-superexchange* paths. The in-plane exchange coupling is about 2 – 3 orders of magnitude stronger than the inter-plane exchange which occurs via two oxygens [Lonkai 03]. For the  $\text{Ho}^{3+}$  ( $4f^{10}$ )

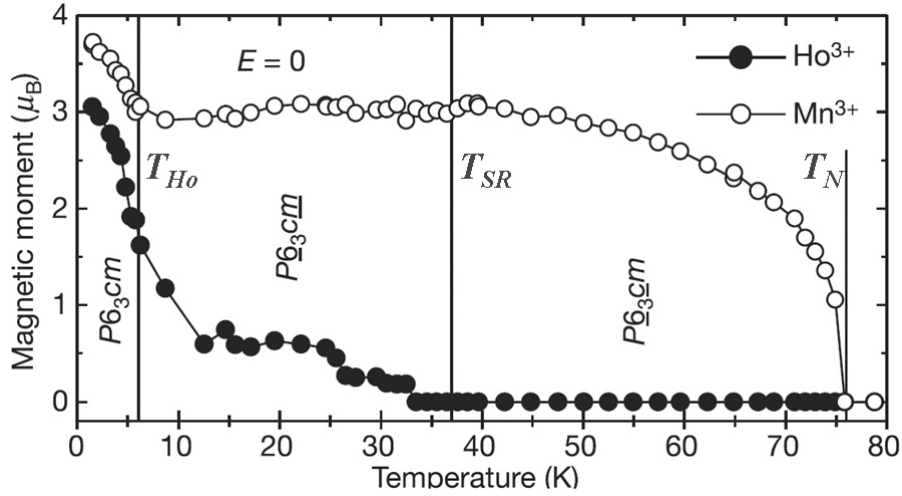


Figure 2.6: Temperature dependence of ordered  $\text{Mn}^{3+}$  and  $\text{Ho}^{3+}$  magnetic moments in  $\text{HoMnO}_3$  [Lottermoser 04b].

sublattice,  $\text{Ho}^{3+}-\text{O}^{2-}-\text{Mn}^{3+}$  and  $\text{Ho}^{3+}-\text{O}^{2-}-\text{Ho}^{3+}$  superexchange paths via the  $ab$  plane and/or  $c$ -axis can be considered.

With these interaction paths, the rare-earth ion  $\text{Ho}^{3+}$  also orders magnetically. Below  $T_{Ho} = 4.2 \text{ K} - 6 \text{ K}$ , long-range ordering of the rare-earth sublattice occurs antiferromagnetically or ferrimagnetically along the  $c$ -axis [Lottermoser 04b]. As discussed in §2.1.2, the  $\text{Mn}^{3+}$  spins arrange in a triangular antiferromagnetic order in the basal plane below  $T_N$ . Due to this frustrated order, the magnetic moments of the  $\text{Mn}^{3+}$  ions essentially cancel each other. In this condition, only the  $\text{Ho}^{3+}$  ion's magnetic moment contributes to the magnetization measured in magnetic field at low temperature.

Additionally, a coupling between  $\text{Ho}^{3+}$  and  $\text{Mn}^{3+}$  can affect the magnetic order. For instance, the spin reorientation of  $\text{Mn}^{3+}$  seems to be related to the ordering of  $\text{Ho}^{3+}$ . Figure 2.6 shows the temperature dependence of the ordered  $\text{Mn}^{3+}$  and  $\text{Ho}^{3+}$  magnetic moments in  $\text{HoMnO}_3$  measured by neutron diffraction. The  $\text{Mn}^{3+}$  ions' magnetic moments start to order below  $T_N$  and keep ordering till  $T_{SR}$ . In the temperature range,  $T_{Ho} < T < T_{SR}$ , the magnetic order of  $\text{Mn}^{3+}$  remains constant, but shows a steep increase below  $T_{Ho}$ . For the case of  $\text{Ho}^{3+}$ , the  $\text{Ho}^{3+}$  magnetic ordering sets in below  $T_{SR}$ . Below  $T_{Ho}$ , the  $\text{Ho}^{3+}$  order steeply rises. The increasing ordered moment of  $\text{Ho}^{3+}$  at  $T_{SR}$  indicates the influence of the  $\text{Mn}^{3+}$  spin order on that of  $\text{Ho}^{3+}$ . On the other hand, the step increase for  $\text{Mn}^{3+}$  below  $T_{Ho}$  is an

evidence of the  $\text{Ho}^{3+}$  spin order influencing the  $\text{Mn}^{3+}$  order. As this graph shows, obvious correlations exist between the  $\text{Ho}^{3+}$  and the  $\text{Mn}^{3+}$  sublattice in  $\text{HoMnO}_3$ .

## 2.3 Phase diagrams

The above mentioned superexchange paths and the interactions between  $\text{Ho}^{3+}$  ( $4f^{10}$ ) and  $\text{Mn}^{3+}$  ( $3d^4$ ) play the major role of the rich magnetic behavior. The magnetic phase diagram of hexagonal  $\text{HoMnO}_3$  has been investigated so far by neutron diffraction [Vajk 06], non-linear optics [Fiebig 02] and magnetic / dielectric measurements [Lorenz 05]. The suggested phase diagrams differ slightly from one another, but agree in the general features. They show an abundance of phases at low temperatures.

Figure 2.7 is a phase diagram established based on SHG [Fiebig 02]. This phase diagram shows magnetic symmetry changes as a function of temperature and applied magnetic field. It is clear that magnetic phase transitions can occur not only by change of temperature, but also by an applied magnetic field. As the magnetic field

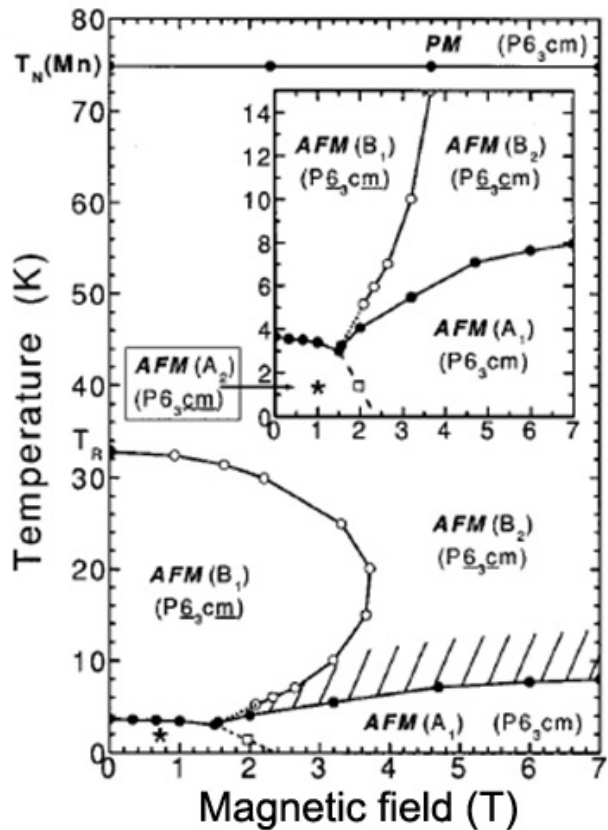


Figure 2.7: Magnetic phase diagram of  $\text{HoMnO}_3$  determined by SHG for a magnetic field  $H \parallel c$ . Closed and open circles denote data points gained in temperature decreasing measurements and in field increasing or decreasing measurements, respectively [Fiebig 02]. The A and B phases are from Fig.2.5.

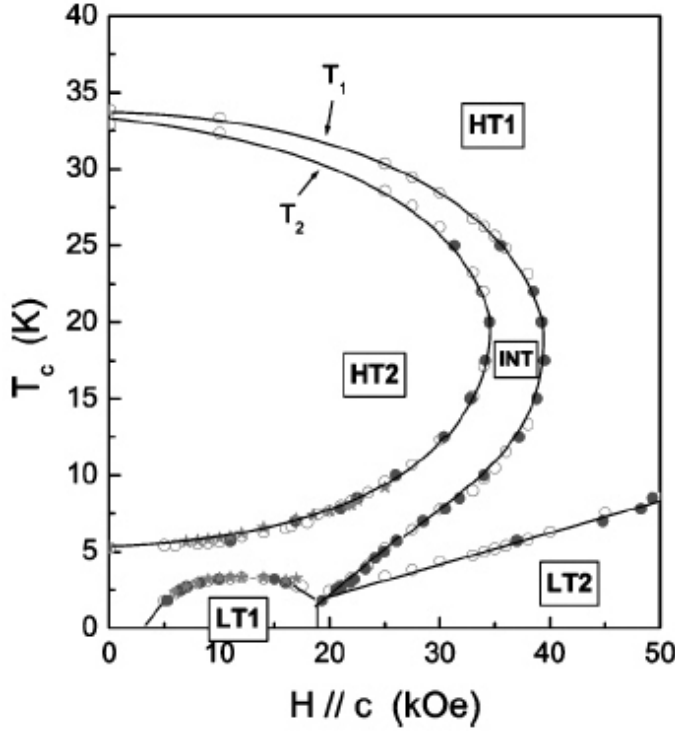


Figure 2.8: Magnetic phase diagram of single-crystal  $\text{HoMnO}_3$  below the Néel temperature. Different phase boundaries are determined by anomalies of the dc magnetization (open circles), ac susceptibility (solid circles), and heat capacity (stars) [Lorenz 05].

increases, the spin-reorientation temperature of the Mn sublattice,  $T_{SR}$  shifts to lower temperature and a field-induced phase transition takes place, i.e.  $\mathbf{P}\underline{\mathbf{6}}_3\mathbf{cm}$  phase changes to  $\mathbf{P}\underline{\mathbf{6}}_3\mathbf{cm}$ . At low temperature, the four magnetic symmetries meet at a tetracritical point ( $\mu_0 H = 1.5 - 2.0$  T,  $T = 3 - 4$  K). The hatched area indicates the presence of a very broad hysteresis. Note that  $T_N$ , where the  $\text{Ho}^{3+}$  moments are paramagnetic, is not influenced by the magnetic field. On the other hand,  $T_{SR}$ , which is related to  $\text{Ho}^{3+}$  ordering, is varying considerably. This suggests that the field-induced magnetic transitions are mainly driven by  $\text{Ho}^{3+}$ . The complexity at low temperature may serve as another clue for the crucial role of  $\text{Ho}^{3+}$ . Fiebig *et al.* argued that the phase diagram is largely determined by magnetic contributions from the partially field  $4f$  shell of the rare-earth ions, probably on the basis of a strong  $\text{Mn}^{3+}(3d^4) - \text{Ho}^{3+}(4f^{10})$  superexchange interaction [Fiebig 02].

A slightly modified magnetic phase diagram of  $\text{HoMnO}_3$  was derived from magnetization, susceptibility and heat capacity measurements as shown in Fig.2.8. HT1, HT2 and LT1, LT2 denote high temperature and low temperature phases, respectively. This phase diagram is rather similar to that from SHG. However, it shows a more complex nature with an intermediate (INT) phase which separates the  $\mathbf{P}\underline{\mathbf{6}}_3\mathbf{cm}$  and  $\mathbf{P}\underline{\mathbf{6}}_3\mathbf{cm}$  phases below  $T_{SR}$  and a dome-shaped LT1 phase. The intermediate phase is observed only below  $T_{SR}$ , where  $\text{Ho}^{3+}$  ordering becomes significant. The

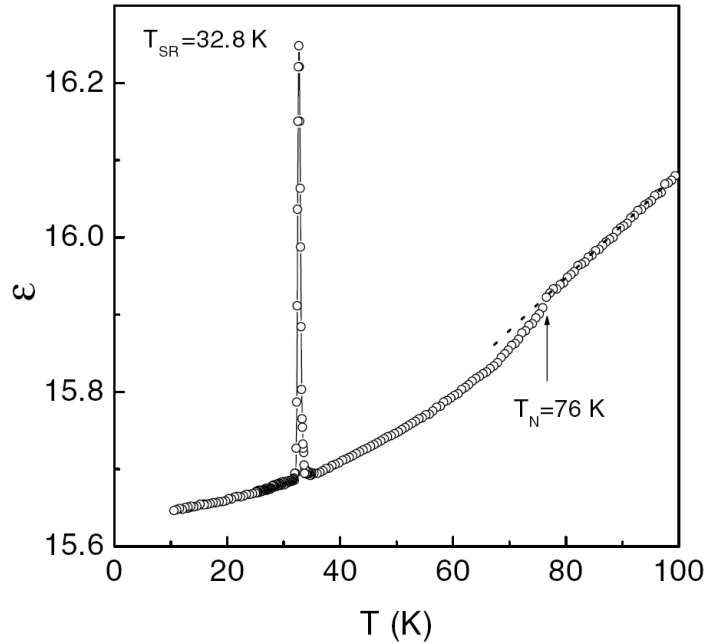


Figure 2.9: Temperature dependence of the dielectric permittivity of a  $\text{HoMnO}_3$  single-crystal at 100 kHz along the  $c$ -axis [Lorenz 04a].

transition into the LT1 phase is supposed to be related to the ordering of  $\text{Ho}^{3+}$  magnetic moments.

## 2.4 Magnetolectric coupling

Hexagonal  $\text{HoMnO}_3$  is multiferroic with coexisting ferroelectric and antiferromagnetic orders at low temperature.  $\text{HoMnO}_3$  becomes ferroelectric below  $T_{CE} = 875$  K, and antiferromagnetic order sets in at  $T_N = 76$  K.

Magnetolectric (ME) properties of  $\text{HoMnO}_3$  were observed in various ways. In ME crystals, as a result of the coupling between electric and magnetic ordering, the magnetic (electric) properties should display changes at those temperatures where electric (magnetic) order changes.

According to this idea, the ME effect of  $\text{HoMnO}_3$  was confirmed recently by dielectric constant measurements [Iwata 98, Lorenz 04a, Yen 05]. As shown in Fig.2.9, the dielectric constant shows two distinct anomalies at  $T_N$  and  $T_{SR}$ . This clearly shows that the ferroelectric order is affected by the onset of the long-range antiferromagnetic order and the spin-reorientation of  $\text{Mn}^{3+}$ . Furthermore, these anomalies exhibit no dispersion with respect to measurement frequency indicating that they do not originate from ferroelectric but from magnetic order. This experiment clearly



reveals a coupling between magnetic and electric orders [Lorenz 04a].

As a second example, magnetic phase control by an applied electric field has been reported [Lottermoser 04b]. In this paper, it was demonstrated that the anti-ferromagnetic order of  $\text{Ho}^{3+}$  ions can be switched to ferromagnetic *reversibly* by an applied electric field of 100 kV/cm along the  $c$ -axis. Additionally, the SHG signal, from the magnetic order of the Mn sublattice, changed from symmetry  $\mathbf{P6}_3\mathbf{cm}$  to  $\mathbf{P6}_3\mathbf{cm}$ , indicating an electrically controlled magnetic transition in the Mn sublattice below  $T_N$ . This obviously means that both Ho and Mn magnetic sublattices are influenced by applying an electric field, and  $\text{HoMnO}_3$  has a strong magnetoelectric coupling.

With its magnetoelectric nature and its rich variety of low-temperature magnetic phases,  $\text{HoMnO}_3$  became a prototype multiferroic magnetoelectric for fundamental studies.



## Chapter 3

# Experimental methods

In this chapter, the experimental details of the film growth with pulsed laser deposition, and ex-situ characterization methods will be described.

### 3.1 Sample preparation

#### Pulsed Laser Deposition

During the recent years, pulsed laser deposition (PLD) has emerged as a suitable method for thin film growth. The reason for using PLD in preference to other deposition techniques lies primarily in its pulsed nature, the possibility of growing films far from thermal equilibrium, and, under favorable conditions, the ability to reproduce in thin films the same composition as that of the bulk compound targets [Willmott 00]. In addition, PLD gives high instantaneous deposition rates, clean surfaces and good crystalline quality of the films.

A schematic diagram of the film preparation is shown in Fig.3.1. In the PLD process, an intense laser pulse of few ns duration passes through the optical window of a vacuum chamber and is projected onto a solid target surface, where it is partially absorbed. The surface temperature increases rapidly due to the absorbed laser energy, giving significant material ablation above a critical power density. The critical power density needed for the ablation depends on the target material, its morphology, and the laser pulse wavelength and duration [Willmott 00]. It is of the order of  $1 - 10 \text{ J/cm}^2$  per pulse for complex oxide materials. The ablated material from the target forms a plasma, the so-called *laser plume*, perpendicular to the target surface. The plasma contains ions, electrons and clusters and interacts with the background gas and the laser light. Material from the laser plume is then

deposited on a substrate. Regarding the direction of the laser plume axis to the substrate normal, the deposition geometry is called *on-axis* (laser plume  $\parallel$  substrate normal) or *off-axis* (laser plume  $\perp$  substrate normal). It is known that the off-axis geometry guarantees smoother film surfaces and fewer *droplets* [Holzapfel 92]. On-axis geometry, for the same reason, gives a higher growth rate than off-axis geometry. During deposition, the targets and substrate holder are rotated and moved by a target/substrate manipulator, respectively.

Film growth and chemistry may be supplemented by an ambient background gas, which may affect the plasma plume species in the gas phase or during the surface reaction. Gases are often used either to thermalize the plasma through multiple collisions or to compensate for the loss of a constituent element of the target such as oxygen in ceramics [Gupta 91]. For instance, in-situ processing of oxide superconductors requires a certain amount of background oxygen in the chamber during deposition [Chrisey 94].

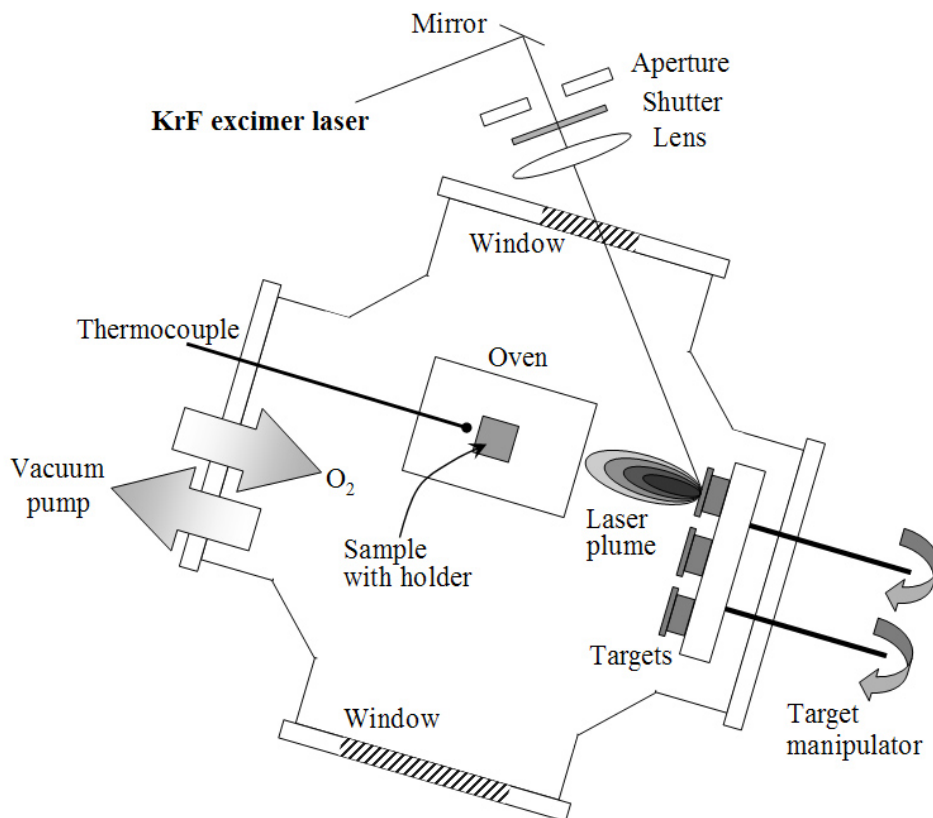


Figure 3.1: Scheme of the pulsed laser deposition chamber used for this work.

With the fact that the stoichiometry of the target material is well reproduced in the film, PLD can be used for the deposition of a wide variety of materials [Chrisey 94]. Multicomponent compounds can be deposited in combination with various pure element targets [Krebs 93] under variation of the composition, e.g. Sm-Co [Singh 05], Pr-Co [Patra 07] and Nd-Fe-B [Kwon 07]. Compound targets are often employed in PLD. This is perhaps PLD's greatest advantage over other deposition techniques and has been most famously exploited in the thin film growth of ceramic superconductors [Roas 88, Gross 90, Kwon 93].

In this work, a KrF excimer laser with a wavelength  $\lambda = 248$  nm (35 ns pulse width) was employed as a PLD source (Lambda Physik LPX305). The laser energy is measured precisely by an energy meter (Molelectron 3sigma with J50 detector) before each film deposition. It ranges from 500 mJ to 640 mJ ( $3 - 5$  J/cm<sup>2</sup>) depending on which targets are used.

To achieve the vacuum, a conventional rotary pump is used which can provide a base pressure of  $\sim 10^{-3}$  mbar. Pure oxygen gas flows with a controlled rate during deposition.

As a substrate, yttrium-stabilized zirconia (Y:ZrO<sub>2</sub>, YSZ) with (111) orientation is used (size of  $10 \times 10 \times 0.5$  mm<sup>3</sup> or  $5 \times 5 \times 0.5$  mm<sup>3</sup>). The in-plane lattice parameter of the YSZ (111) substrate is  $a_{110} = 3.623$  Å. A one-side polished substrate is generally used. However, for optical investigations (SHG) in transmission geometry, transparent both-side polished substrates are also necessary.

The substrate is located in a ceramic oven wound with Kanthal wire. In the oven, the temperature can be controlled from 400 °C to 900 °C. The substrate temperature is controlled accurately by a thermocouple located ca. 5 mm away from substrate. The target to substrate distance is maintained at ca. 3.5 cm for the HoMnO<sub>3</sub> deposition.

Polycrystalline HoMnO<sub>3</sub> targets (Chem Co GmbH) with a purity of 99.9 % and a density of  $3.5 - 4.07$  g/cm<sup>3</sup> are used. The lattice parameters of HoMnO<sub>3</sub> are  $a = 3.515$  Å and  $c = 11.412$  Å [Muñoz 01]. The in-plane lattice mismatch between substrate and HoMnO<sub>3</sub> is about 3 % giving rise to a tensile force in the film layer. The size of the pellet-shaped target is 20 mm in diameter and 6 mm in thickness. To deposit a metal bottom electrode for the capacitor trilayer (see §4.4) a platinum (Pt) metal target is also employed.

Both *on*-axis and *off*-axis deposition geometries are used for HoMnO<sub>3</sub> film growth. The growth rate with off-axis deposition geometry was too low in consideration of the expense of the HoMnO<sub>3</sub> target erosion. Therefore, only thin HoMnO<sub>3</sub>

Table 3.1: Deposition conditions for HoMnO<sub>3</sub> films and the Pt bottom electrode.

Parameters	HoMnO <sub>3</sub>	Pt electrode
Substrate temperature ( $T_S$ )	850 °C	400 °C
Oxygen pressure ( $p_{O_2}$ )	$1 \times 10^{-1}$ mbar	$1 \times 10^{-2}$ mbar
Laser energy ( $E$ )	ca. 515 mJ	ca. 600 mJ
Frequency ( $f$ )	1 – 2 Hz	10 – 15 Hz

films ( $\lesssim 30$  nm) were deposited by off-axis, otherwise, most films were grown with on-axis deposition. The growth rates of HoMnO<sub>3</sub> are roughly estimated to be 2.5 nm per 100 pulses (on-axis) at 850 °C,  $p_{O_2} = 1 \times 10^{-1}$  mbar and one order of magnitude lower for off-axis deposition geometry. The Pt bottom layer is deposited in the on-axis geometry. To pattern a structure, for a step for thickness measurement or a capacitor layer, various deposition masks were used during deposition.

The optimized deposition condition parameters for HoMnO<sub>3</sub> films and the Pt bottom electrode are summarized in Tab.3.1.

## 3.2 Sample characterization

### Structural analysis

The film's epitaxial growth and phase purity have been confirmed by x-ray diffraction (XRD) using *Bragg-Brentano* ( $\theta-2\theta$ ) geometry,  $\phi$ -scans and *pole figure* measurements.

The out-of-plane orientation is investigated using the Bragg-Brentano diffraction geometry. In Bragg-Brentano diffraction, x-ray reflections can be obtained only from the planes parallel to the sample surface satisfying Bragg's law written as

$$n\lambda = 2d \sin \theta \quad (3.1)$$

where  $n$  is integer,  $\lambda$  is the wavelength of the x-ray source,  $d$  is the distance between the adjacent atomic planes and  $\theta$  is the so-called *Bragg* angle, i.e. the angle between the incident beam and the atomic planes. From Eq.3.1 the  $d$ -lattice spacing can be calculated knowing  $\lambda$  and  $\theta$ . A lattice parameter variation with thickness will be shown in §4.2.

In epitaxially grown films, the intensities of the preferred orientation become strong. Hence, the relative intensity of the diffraction peaks is a measure of the de-

gree of texture of the samples. Furthermore, the degree of texture can be qualified by measuring the angular spread of the preferred orientations around the substrate normal axis. The angular spread can be measured by a rocking curve scan (also known as  $\omega$ -scan), where the incident beam is moved (rocked) through the Bragg angle  $\theta$ , while the counter, which collects the reflected beam, is fixed at the angle  $\omega$ . The *full width at half maximum* (FWHM) value of the rocking curve is a direct measure of the angular spread of the orientation present in the irradiated area [Cullity 78]. A sharp rocking curve, therefore, indicates a high quality texture.

In addition to the out-of-plane texture, *pole figure* measurements are needed for in-plane texture confirmation. Pole figure means a stereographic projection with a specified  $\{hkl\}$  orientation. The appearance of distinct sets of poles indicates an in-plane texture in the sample. For films, favored specific crystallographic directions are generally substrate-dependent.

For the pole figure measurements the angles  $\theta$  and  $\psi$  are meaningful. The former is a Bragg angle which indicates the distinct position of the selected  $\{hkl\}$  plane and the latter is the tilting angle between the substrate normal and the  $\{hkl\}$  plane normal. Thus, for Bragg-Brentano measurements,  $\psi = 0$ . With constant  $2\theta$  and  $\psi$  angles, one  $\phi$  scan (in-plane rotation) is measured usually through  $0 - 360^\circ$ . Pole figures are a collective picture of the  $\phi$  scans with regularly stepped  $\psi$  and fixed  $2\theta$  angles.

The  $2\theta$  of the chosen plane can be optimized by finding the maximum intensity. With this  $2\theta$  value, the in-plane lattice parameter ( $a$ ) of the hexagonal lattice can be calculated by [Cullity 78]

$$\frac{1}{d^2} = \frac{4}{3} \left( \frac{h^2 + hk + k^2}{a^2} \right) + \frac{l^2}{c^2} \quad (3.2)$$

where  $a$  and  $c$  indicate the lattice parameters of hexagonal  $\text{HoMnO}_3$ .  $h$ ,  $k$  and  $l$  are the Miller indices of the chosen plane, in this work the (112) plane - in hexagonal notation the  $(11\bar{2}2)$  plane - which is inclined  $61.7^\circ$  (theoretical value) with respect to the hexagonal  $c$ -axis.  $d$  is the distance between adjacent  $\{hkl\}$  planes.

In this work, Bragg-Brentano diffraction and rocking curves are performed by using  $\text{Co } K\alpha$  ( $\lambda = 1.789 \text{ \AA}$ ) radiation as x-ray source (Philips X'pert, XRD), whereas  $\text{Cu } K\alpha$  ( $\lambda = 1.541 \text{ \AA}$ ) radiation is used for the pole figure measurements (Philips X'pert, texture). The voltage and current of the x-ray tube are 40 kV and 40 mA, respectively. All XRD measurements are done at room temperature. The details of the XRD measurement conditions are shown in Tab.3.2.

Table 3.2: *X-ray* diffraction measurement conditions. The in-plane parameters of  $2\theta$  and  $\psi$  are specified with theoretical values because these can vary with the strain state of the films.

	YSZ/(Pt)/HoMnO <sub>3</sub>			rocking curves of HoMnO <sub>3</sub> (000 <i>l</i> )		
Out-of-plane	$2\theta$ range	step	time	$2\theta$ range	step	time
parameters	10–95°	0.05°	3s	±5° of (000 <i>l</i> )	0.005°	1s
	YSZ(111)		HoMnO <sub>3</sub> (0001)		Pt(111)	
In-plane	$2\theta_{100}$	$\psi$	$2\theta_{11\bar{2}2}$	$\psi$	$2\theta_{100}$	$\psi$
parameters	34.8°	54.7°	32.8°	61.7°	46.1°	54.7°

## Surface morphology and thickness measurement

The surface morphology and the roughness of the films are investigated by atomic force microscopy (AFM, Digital Instruments 3100 scanning probe microscope, Nano scope III software). AFM uses the atomic forces (electrostatic force, Van der Waals force, etc.) between the tip atoms and the sample surface atoms at extremely short distances. The change in oscillation amplitude due to these interaction forces acting on the cantilever is used to construct a surface image.

AFM images were recorded in *tapping mode* where a non-magnetic tip mounted on a Si cantilever is maintained at constant distance over the sample surface without touching the sample surface to avoid surface damage. The surface roughness of the sample is often expressed by the root-mean-square roughness ( $R_{rms}$ ), i.e.:

$$R_{rms} = \sqrt{\frac{1}{N} \sum_{i=1}^N (Z_i - \bar{Z})^2} \quad (3.3)$$

where  $N$  is the number of measurement points,  $Z_i$  are the individual heights at the measurement points, and  $\bar{Z}$  is the average height. With the rms roughness the fluctuation of the surface height can be quantified.

As well as a surface image, the film thickness can also be measured by AFM at steps produced by deposition masks. More accurately, however, a depth profilometer (DEKTAK, in the clean room of IFW) was used with a precision of 5 % by measuring the step profiles.



## Magnetic properties

Magnetization measurements have been carried out in a conventional superconducting quantum interference device (SQUID) magnetometer (Quantum Design, MPMS XL, MPMS-5S). SQUID is a very sensitive magnetometer based on the Josephson effect [Barone 82, Ibach 95, Kittel 96]. It has a very high resolution for magnetic moments of the order of  $\sim 10^{-7}$  emu.

The magnetic moment was measured in both out-of-plane ( $H \parallel c$ ) and in-plane ( $H \parallel a$ ) field directions. The temperature ranged from 1.8 K to 300 K controlled by liquid helium flow and an internal heater. The applied magnetic fields are  $-7 \text{ T} \leq \mu_0 H \leq +7 \text{ T}$ .

Magnetization under electric field has been measured by using a voltage sourceme-ter (Keithley 2410) and a special sample holder (Fig.3.3).

## Nonlinear optics experiment

An experimental setup of SHG (refer to §1.5) is shown in Fig.3.2. As a laser source, a Nd:YAG (Y-Al-garnet) laser has been used. The repetition rate can be varied from 0.1 Hz to 100 Hz. The 3 ns pulse has a pulse energy of up to 600 mJ and a wavelength

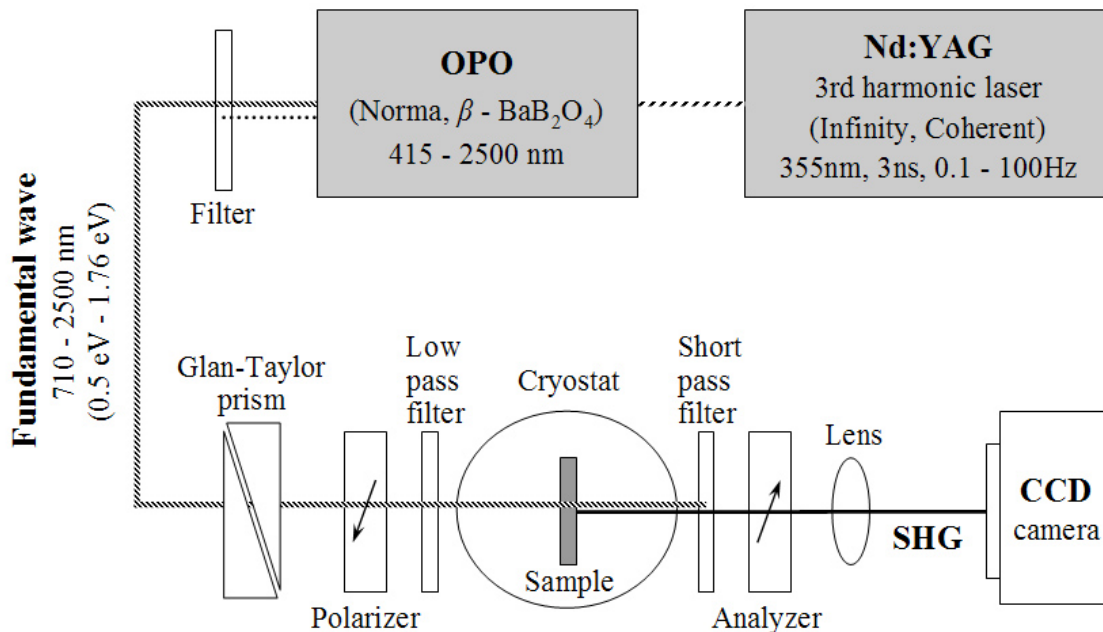


Figure 3.2: Scheme of the SHG measurement setup.

of 1064 nm. The third harmonic of a Nd:YAG laser with a wavelength of 355 nm goes into the optical parametric oscillator (OPO). A  $\beta$ -BaB<sub>2</sub>O<sub>4</sub> (BBO) crystal is used for the OPO. In the OPO, the laser light undergoes two-stage nonlinear-optical processes. In the first stage, the laser is spatially narrowed by passing through a monochromator. The light from the first stage is synchronized spatially, temporally, and spectrally with the BBO in the second stage. The wavelengths achievable with the OPO range from 415 nm to 2500 nm, for corresponding energies from 3 eV to 0.5 eV. For the SHG measurements of HoMnO<sub>3</sub> films, light with energies systematically varied between 0.5 eV and 1.76 eV was taken as incident wave. A Glan-Taylor prism was used in order to obtain a uniform linear polarization direction. With the polarizer, the polarization direction can be rotated. A low pass filter was used to block higher harmonics generated in the optical components. The sample was located in a cryostat equipped with a quartz window. The sample temperature controlled by He gas flow ranged from 4.2 K to 325 K. During the temperature-dependent measurement the temperature was changed with 1 K/min. The short pass filter was used to suppress the fundamental wave behind the sample. An analyzer is used to select a certain polarization of the out-coming light. In the anisotropy measurements, the polarizer and the analyzer were rotated with the same steps at the same time. The polarizations of polarizer and analyzer were generally set parallel or perpendicular to each other. The SHG signal goes through a lens with 135 mm focal length. The resolution of the lens is  $\sim 20 \mu\text{m}$ . Finally, the SHG signal is recorded by a CCD camera. The camera is cooled to  $-105 \text{ }^\circ\text{C}$  by liquid nitrogen in order to reduce noise [Fiebig 96, Fiebig 05b, Kordel 08].

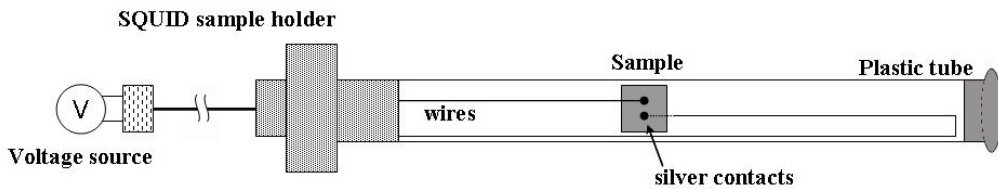


Figure 3.3: Scheme of the sample holder for low-temperature polarization measurements.

## Ferroelectric polarization

The electrical properties, i.e. the ferroelectric polarization of thin films, were measured applying a *Sawyer-Tower circuit* [Kim 91, Yoshimura 03] in a TF analyzer 1000 (aixACCT) with high voltage amplifier (up to 400 V). For the low temperature measurements under the influence of a magnetic field, the TF analyzer is combined with a SQUID magnetometer (MPMS-5S). A specially prepared sample holder is used for the low temperature polarization measurements to apply the voltage as shown in Fig.3.3. The voltage is varied depending on the thickness of the sample to reach 30 – 60 kV/cm (100 kV/cm for bulk  $\text{HoMnO}_3$  [Lottermoser 02]). The measurement temperature ranges usually from 5 K to 80 K (sometimes to 300 K). Hysteresis loops are measured with an *ac* voltage with a frequency of 10 Hz.



## Chapter 4

# Epitaxially grown $\text{HoMnO}_3$ thin films and capacitor layers

Even though hexagonal  $\text{HoMnO}_3$  is presently one of the most studied multiferroics, the knowledge of the behavior and properties of  $\text{HoMnO}_3$  thin films is scarce. In order to investigate the structural and magnetic properties, epitaxially grown  $\text{HoMnO}_3$  thin films have been prepared. A control of the crystal orientation is vitally important, because the ferroelectric polarization of  $\text{HoMnO}_3$  appears along the hexagonal  $c$ -axis.

Additionally, superlattices with the isostructural  $\text{YMnO}_3$  have been deposited on YSZ(111) substrates. A capacitor trilayer with platinum bottom electrode has been prepared for the investigation of ferroelectric and magnetoelectric properties.

## 4.1 Crystal structure

With the deposition conditions shown in Tab.3.1, a series of films with varied thickness between 25 nm and 1000 nm has been grown. Figure 4.1 shows the x-ray diffraction results of the series. The films clearly show  $\text{HoMnO}_3$  (000 $l$ ) reflections. This means that the  $c$ -axes of the hexagonal  $\text{HoMnO}_3$  grains coincide with the film normal. Impurity phases were barely detected in most films. In larger thickness films, for instance 700 nm and 1000 nm, however, small peaks were detected even with fairly low intensity.

Figure 4.2 shows the FWHM values of rocking curves of the (0002) and (0004) peaks. The FWHM values increase with decreasing film thickness. Thinner films show relatively larger FWHM values, i.e. broader diffraction peaks. This is attributed to the finite thickness of the films, since 50 nm thick films contain less than

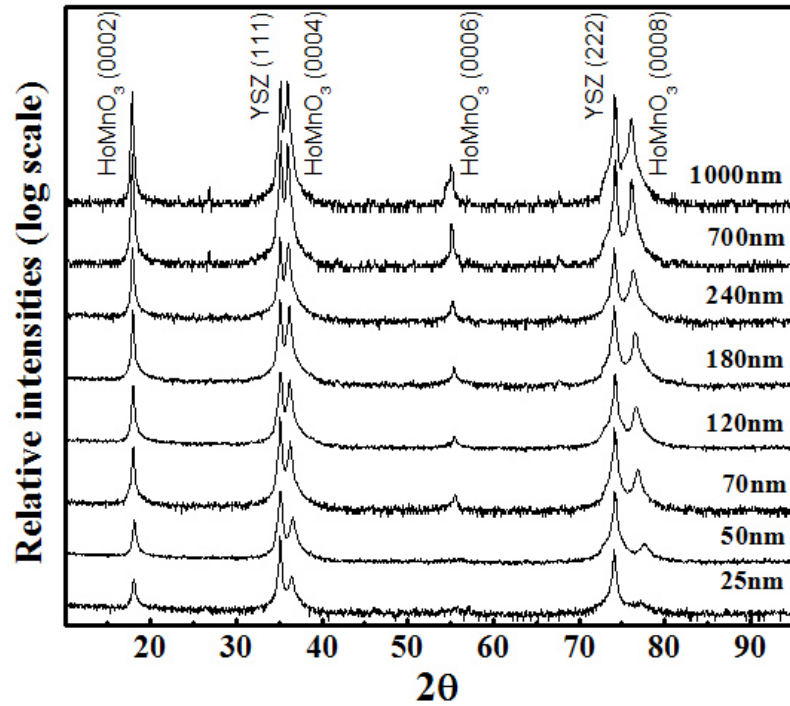


Figure 4.1:  $\theta$ - $2\theta$  x-ray diffraction patterns for various film thickness at optimized deposition parameters.

50 unit cells. The finite thickness effect is related to the well known *Scherrer formula* [Cullity 78] which shows a relationship between the particle size of very small crystals and diffraction peak broadening. The value for the (0002) reflection is only  $0.1^\circ$  for films of more than 100 nm thickness. The reasonably small FWHM values certify a good out-of-plane film crystallinity.

In addition to the out-of-plane crystallinity, the in-plane texture has been investigated in order to confirm the epitaxial growth. It has been measured by using

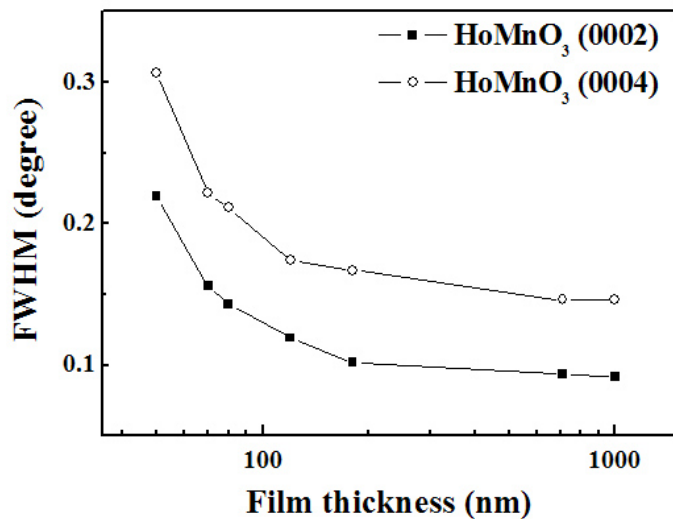


Figure 4.2: Full width at half maximum (FWHM) values of the (0002) and (0004) peaks of  $\text{HoMnO}_3$  films vs. film thickness. Small values of the FWHM at any thickness indicate a good out-of-plane orientation.

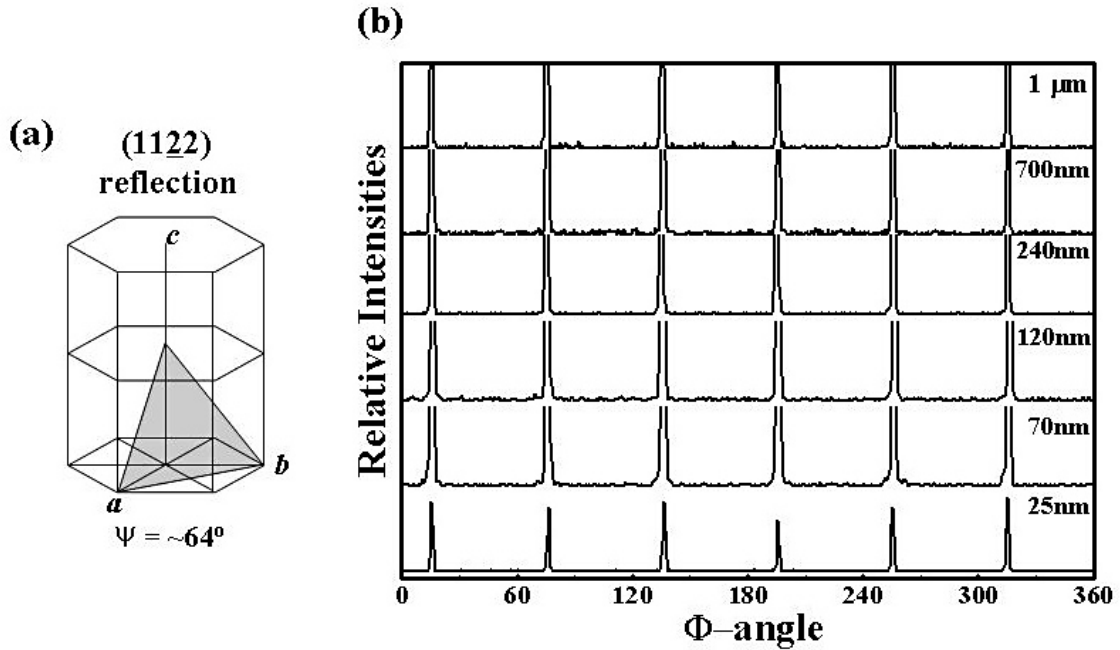


Figure 4.3:  $\phi$  scans were measured with the reflection of  $(11\bar{2}2)$  plane. Six-fold symmetry indicates the hexagonal structure. (a) scheme of  $(11\bar{2}2)$  plane and (b)  $\phi$  scans.

the  $(11\bar{2}2)$  plane reflection inclined  $64^\circ$  relative to the  $c$ -axis as shown in Fig.4.3(a). Figure 4.3(b) shows the  $\phi$  scans of the  $\text{HoMnO}_3$  films. The six-fold symmetry indicating a hexagonal phase without twinning has been observed over the whole thickness range. In this work, as shown, the pure hexagonal phase is well maintained even up to  $1 \mu\text{m}$  thick film. This result, together with the out-of-plane XRD, confirms that a twin-free hexagonal phase has been epitaxially grown.

Figure 4.4 represents typical pole figures of the  $\text{HoMnO}_3$  films with a clear six-fold symmetry for different deposition oxygen pressures  $p_{\text{O}_2}$ . In a previous study, twinning within the hexagonal  $c$ -plane has been observed for isostructural  $\text{YMnO}_3/\text{YSZ}(111)$  films above  $1.3 \times 10^{-2}$  mbar oxygen pressure [Dho 04]. In contrast to that study, no twinning in the hexagonal  $ab$  plane occurred even for  $p_{\text{O}_2}$  as high as 0.5 mbar in this work.

Besides the good crystalline quality, the  $\text{HoMnO}_3$  films generally have a smooth surface. Figure 4.5 shows a superb surface morphology for a  $1 \mu\text{m}$  thick film measured by AFM. Impressively, the root-mean-square surface roughness rms is only 0.8 nm, and the maximum peak-to-valley distance is 6.7 nm. Hence, this film has a

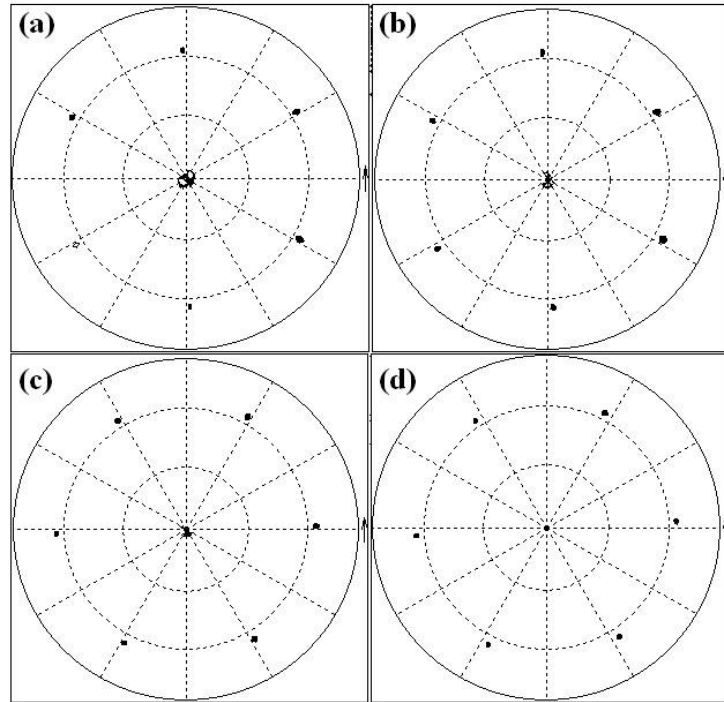


Figure 4.4: Pole figures of the  $(11\bar{2}2)$  plane reflection for different deposition oxygen pressures ( $p_{O_2}$ ). (a)  $1 \times 10^{-2}$  mbar, (b)  $5 \times 10^{-2}$  mbar, (c)  $1 \times 10^{-1}$  mbar and (d)  $5 \times 10^{-1}$  mbar, respectively.

very smooth surface despite its large thickness.

## 4.2 Lattice parameters

The in-plane lattice parameters of bulk  $\text{HoMnO}_3$  and the YSZ(111) substrate are  $a = 3.515 \text{ \AA}$  and  $a_{110} = 3.623 \text{ \AA}$ , respectively. The substrate has a larger lattice parameter than that of the film by  $\sim 3 \%$ . Therefore, a tensile stress is expected in the  $\text{HoMnO}_3$  films.

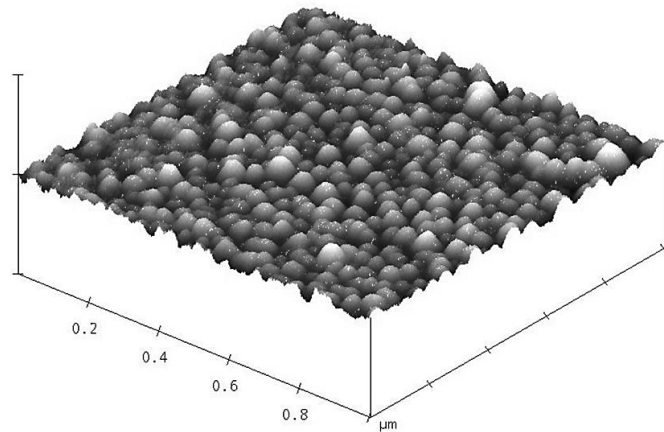


Figure 4.5: A surface morphology image of a  $1 \mu\text{m}$  thick  $\text{HoMnO}_3$  film by atomic force microscopy with lateral and height scales of  $1 \mu\text{m}$  and  $10 \text{ nm}$ , respectively [Kim 09].



YMnO<sub>3</sub> has the same lattice as HoMnO<sub>3</sub>. According to Dho *et al.* [Dho 04], the YMnO<sub>3</sub> films on YSZ(111) substrates deposited by PLD show a slightly enlarged  $c$  lattice parameter at thin thicknesses. Then, the  $c$  parameter gradually decreases with increasing film thickness and approaches the lattice constant of the bulk material at 250 nm thickness. This surprising result reveals a behavior that cannot solely originate from elastic strain.

A somewhat different lattice parameter variation has been revealed by Dubourdieu *et al.* [Dubourdieu 07]. They deposited various REMnO<sub>3</sub> films by metal organic chemical vapor deposition. In that work, the  $c$  parameter of both YMnO<sub>3</sub>/YSZ (111) and HoMnO<sub>3</sub>/YSZ(111) increases rapidly in the  $d < 30$  nm thickness range and moves towards the bulk parameter for larger thickness with a small increment. However, the  $c$  parameter does *not* exceed the bulk lattice parameter in both cases.

In this work, the  $c$  lattice parameter shows smaller values than that of the bulk below  $\sim 50$  nm thickness as shown in Fig.4.6. The smallest value for the 25 nm thick film is  $\sim 3$  % smaller than the bulk value. It increases rather rapidly for film thickness up to  $d = 240$  nm. Above 240 nm, it reaches a steady value. The in-plane lattice parameter ( $a$  lattice parameter) shows a gradual tendency for increase, which is maintained linearly throughout the whole thickness range.

The small  $c$  lattice parameter of the thinnest films in comparison with that of bulk HoMnO<sub>3</sub> is attributed to the in-plane tensile stress that elastically induces a contraction of the out-of-plane lattice parameter of the epitaxial films. On the other hand, the  $c$  parameter exceeding that of bulk HoMnO<sub>3</sub> for  $d > 50$  nm by  $\sim 1$  % is a less expected observation. The  $a$  parameter, too, is enlarged by  $\sim 1.5$  % for the thicker films. Since this is no relaxation towards the bulk values for both  $c$  and  $a$  of thick films, a substrate strain is unlikely as origin for the enlarged lattice parameters. A number of oxide materials grow with larger unit cells in thin films. Defects in the crystal lattice (such as the nanoscale inclusions described in [Kordel 09]) or slight compositional variations are possible reasons for this. The expanded in-plane lattice parameter may result in the weakening of the inter-plane ionic bond strength as well. The elongated  $c$  lattice parameter, as will be discussed in chapter 5, may serve as a reason for the weakened Ho<sup>3+</sup> antiferromagnetic order.

### 4.3 HoMnO<sub>3</sub>/YMnO<sub>3</sub> superlattices

Superlattices have been grown with the isostructural YMnO<sub>3</sub> on a YSZ(111) substrate. Figure 4.7 shows x-ray diffraction patterns of a typical (HoMnO<sub>3</sub>/YMnO<sub>3</sub>)<sub>30</sub>

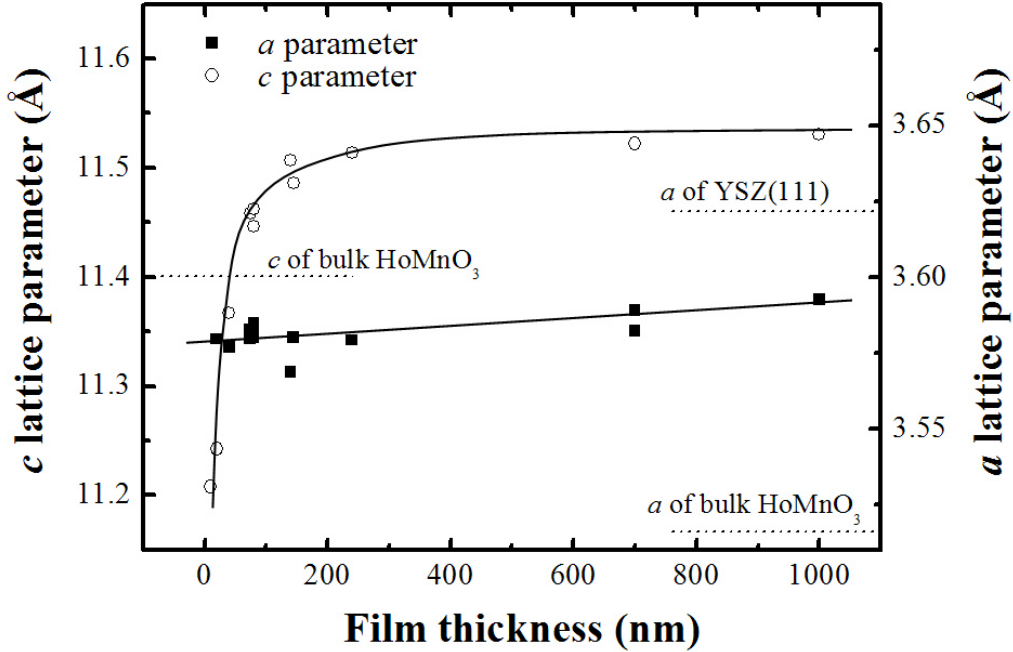


Figure 4.6: The  $a$  and  $c$  lattice parameter variation with film thickness. The lattice parameters are calculated from the  $2\theta$  angles of the (0002) and the (11 $\bar{2}$ 2) peaks, respectively.

multilayer. The multilayer starts with  $\text{HoMnO}_3$ . Superlattice peaks are observed near the  $\text{HoMnO}_3$  (000 $l$ ) peaks. With these superlattice peaks, the thickness of the layer can be calculated by [Ohring 91]:

$$\Lambda = \frac{(n_i - n_j)\lambda}{2(\sin \theta_i - \sin \theta_j)} \quad (4.1)$$

where  $\Lambda$  is the thickness of a pair of  $\text{HoMnO}_3 + \text{YMnO}_3$  film layers, i.e. the period of the superlattice,  $n_i$  and  $n_j$  are superlattice diffraction orders,  $\lambda$  means the wavelength of the x-ray source (here  $\lambda_{\text{Co}} = 1.789 \text{ \AA}$ ), and  $\theta_i$  and  $\theta_j$  are the diffraction angles for  $n_i$  and  $n_j$ , respectively.

Figure 4.8 shows examples of thickness fringes and superlattice peaks. Thickness fringes (Fig.4.8(a)) rather than superlattice peaks have been observed when the film thickness is thin (generally less than 50 nm) and the surface roughness is smooth enough. When the number of pulses per layer is too small to deposit one unit cell ( $c = 11.4 \text{ \AA}$ ), thickness fringes are observed. In this case,  $\text{HoMnO}_3$  and  $\text{YMnO}_3$  mix inside each unit cell layer.

Figure 4.8(b) shows diffraction patterns of superlattices for samples of various

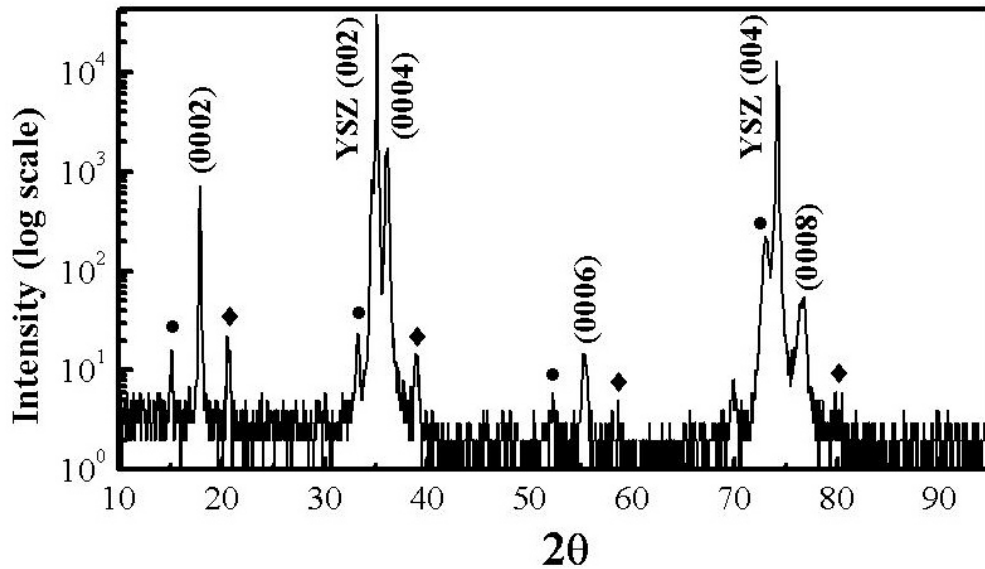


Figure 4.7:  $\theta$ - $2\theta$  x-ray diffraction patterns of hexagonal  $(\text{HoMnO}_3/\text{YMnO}_3)_{30}$  superlattices on a YSZ(111) substrate.

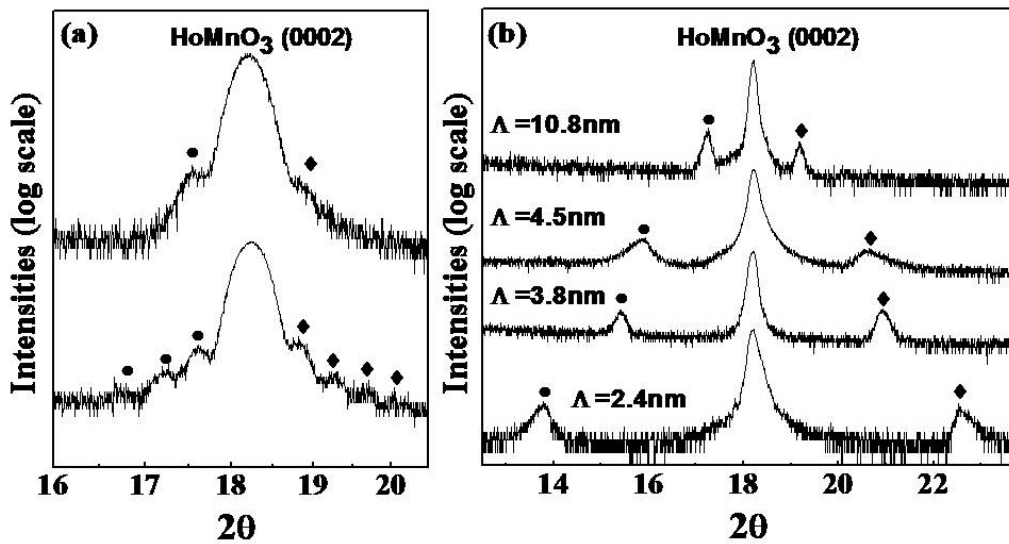


Figure 4.8: (a) Thickness fringes of hexagonal  $\text{HoMnO}_3$  and  $\text{YMnO}_3$ . (b) Epitaxial superlattices of hexagonal  $\text{HoMnO}_3$  and  $\text{YMnO}_3$ . The thickness of the upper and the bottom film in panel (a) is ca. 15 nm and 22 nm, respectively.  $\Lambda$  indicates the superlattice period.

period. Next to the HoMnO<sub>3</sub>(0002) peak, superlattice peaks exist clearly at both sides with equal distance. This distance is decreasing as the period of the superlattice is increasing. By Eq.4.1, the period of the superlattice ( $\Lambda$ ) is calculated. The minimum  $\Lambda$  is ca.  $2.4 \pm 0.1$  nm indicating one unit cell thickness of each HoMnO<sub>3</sub> and YMnO<sub>3</sub> layer.

The in-plane texture of these superlattices shows a clear six-fold symmetry. The FWHM values of the (11 $\bar{2}$ 2) plane of (HoMnO<sub>3</sub>/YMnO<sub>3</sub>)<sub>30</sub> is slightly increased (ca. 1.85°) compared to those of the HoMnO<sub>3</sub> films (FWHM  $\sim$  1.63°–1.76°) but still indicates a good quality of the in-plane texture.

## 4.4 Capacitor trilayer

In order to study the ferroelectric and magnetoelectric properties of HoMnO<sub>3</sub> films electrically, a bottom and an upper electrode are needed for the application of the electric field. For this, a capacitor layer of HoMnO<sub>3</sub>/Pt/YSZ(111) is grown.

Figure 4.9 shows a  $\theta$ - $2\theta$  x-ray diffraction pattern and  $\phi$  scans of the layer.  $\phi$  scans were measured with the reflection of the (11 $\bar{2}$ 2) plane for HoMnO<sub>3</sub> and the (100) reflection of the Pt layer. A clear Pt(222) reflection along with HoMnO<sub>3</sub> (000 $l$ ) reflections is obvious in Fig.4.9(a). This indicates that both the Pt and the HoMnO<sub>3</sub> layer grow with a well-defined orientation on the YSZ(111) substrate. The in-plane texture investigated by  $\phi$  scans shows that the platinum bottom layer grows with epitaxial orientation on YSZ(111), with a small amount of twins seen at the 3 small peaks. The  $\phi$  scan of the HoMnO<sub>3</sub> (0001) layer confirms the six-fold symmetry indicating the hexagonal phase [Kim 07a]. This means that the platinum bottom layer does not disturb the epitaxial growth of hexagonal HoMnO<sub>3</sub> even though small amounts of twins exist in the bottom electrode layer.

In spite of the epitaxial growth of the capacitor layer, an unexpected problem related with the bottom Pt electrode occurred. The Pt electrode lost its conductivity after the HoMnO<sub>3</sub> film layer deposition in a number of samples. To figure out the reason, annealing experiments were performed. Figure 4.10(a) shows AFM images of a Pt bottom electrode which was deposited at 400 °C and (b) after annealing at 850 °C for 90 min (i.e. at the same conditions as for the HoMnO<sub>3</sub> deposition). In Fig.4.10(a) a continuous Pt layer is observed before annealing, whereas, after annealing, separate islands of Pt are present for the same sample as shown in Fig.4.10(b). It is concluded that during the deposition of HoMnO<sub>3</sub> at 850 °C, which takes 1 – 2 hours, the bottom electrode recrystallized into Pt islands and, therefore, lost its

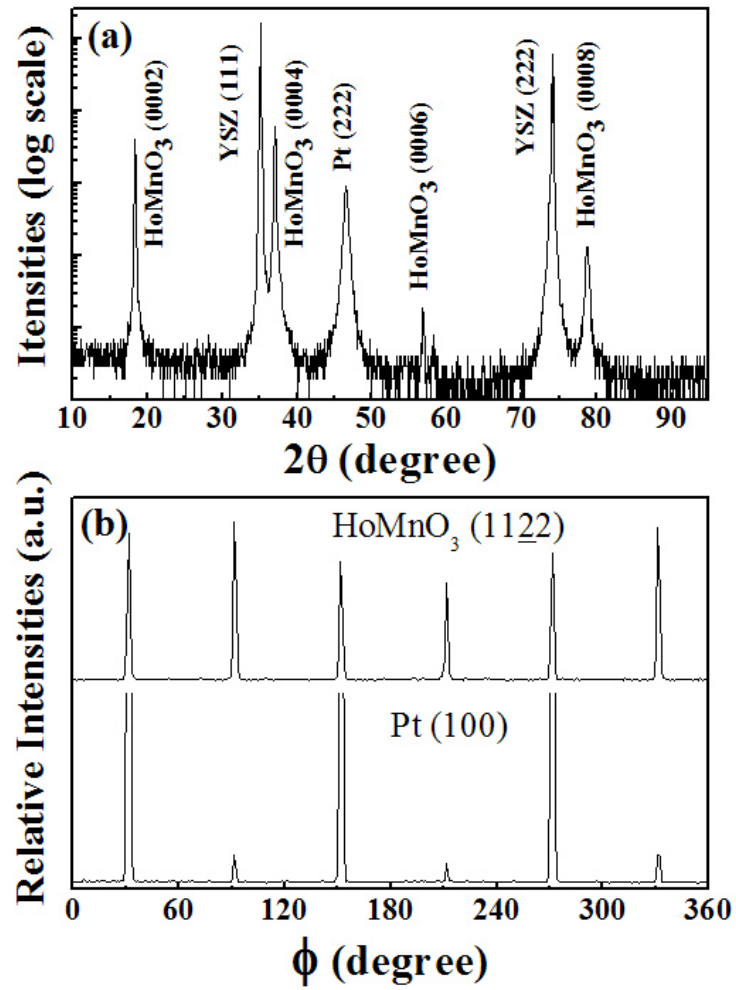


Figure 4.9: (a)  $\theta$ - $2\theta$  x-ray diffraction pattern and (b)  $\phi$  scans of a capacitor layer.  $\phi$  scans were measured with  $\text{HoMnO}_3(11\bar{2}2)$  and  $\text{Pt}(100)$  reflections.

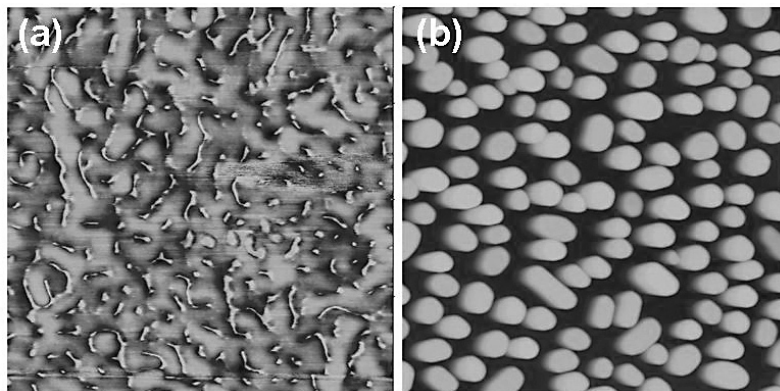


Figure 4.10: Pt bottom electrode images by AFM (a) as deposited at 400 °C and (b) after annealing at 850 °C for 90 min [Kim 07b].

connectivity and conductivity.

In order to obtain a conducting Pt bottom electrode after  $\text{HoMnO}_3$  film deposition, the Pt electrode thickness was enhanced. It was found that a Pt bottom electrode of more than 30 – 50 nm thickness could maintain conductivity avoiding recrystallization into separated islands after  $\text{HoMnO}_3$  layer deposition [Kim 07b]. For this reason, the Pt electrode is deposited using the on-axis deposition geometry to insure a sufficiently thick layer.

## 4.5 Summary

The preparation of multiferroic hexagonal  $\text{HoMnO}_3$  films on YSZ(111) substrates was done for the first time. By using the optimized deposition conditions, hexagonal  $\text{HoMnO}_3$  films of 25 – 1000 nm thickness were grown by pulsed laser deposition. Conventional x-ray diffraction shows the epitaxial growth with (000 $l$ ) orientation and good crystalline quality. The pole figure measurements indicate a twin-free hexagonal phase. The surface morphology imaged by AFM revealed a reasonably smooth surface (rms < 1 nm) even for the considerable thickness of up to 1  $\mu\text{m}$ .

The hexagonal lattice parameters varies with the film thickness. The  $c$  lattice parameter increases rapidly with thickness for  $d < 50$  nm and remains stable in films thicker than 240 nm. The  $a$  lattice parameter increases linearly with thickness. Thicker films ( $d \geq 100$  nm) thus show enlarged lattice parameters both in the hexagonal plane as well as along the hexagonal axis. This cannot be understood as a result of elastic strain from the somewhat larger YSZ(111) substrate. Whereas such an observation of enlarged volume in oxide films is not unusual, it may have a strong impact on the magnetic properties of the highly frustrated  $\text{HoMnO}_3$ .

Superlattice structures of  $(\text{HoMnO}_3/\text{YMnO}_3)_{30}$  have been deposited on YSZ(111) substrates. With the isostructural  $\text{YMnO}_3$  superlattice peaks are clearly observed around the  $\text{HoMnO}_3$  (000 $l$ ) peaks. The superlattices grow coherently in the hexagonal phase. Single layers as thin as one unit cell lead to a well-defined superlattice.

For the investigation of the ferroelectric and the magnetoelectric properties, a capacitor trilayer structure with a Pt bottom electrode to the  $\text{HoMnO}_3$  layer has been prepared. In  $\phi$  scan measurements, the Pt bottom electrode on a YSZ(111) substrate exhibits a small amount of twins. Nevertheless,  $\text{HoMnO}_3$  grows epitaxially on the Pt bottom electrode, with the same orientation as without the Pt layer. The Pt electrode should be thick enough to ensure its connectivity / conductivity after the  $\text{HoMnO}_3$  deposition.

## Chapter 5

# Magnetic properties and phase diagram of films and single-crystals

Magnetic structure investigations on hexagonal  $\text{HoMnO}_3$  have so far been carried out mainly by neutron scattering [Muñoz 01, Vajk 05] and non-linear optics [Fröhlich 99, Fiebig 02, Fiebig 03].

Meanwhile, magnetization data of  $\text{HoMnO}_3$  single-crystals are still quite scarce [Sugie 02, Lorenz 05], with the situation being worse for thin films. To understand the fundamental magnetic properties of hexagonal  $\text{HoMnO}_3$ , more magnetic property investigations are required.

In this chapter, the magnetization of epitaxially grown  $\text{HoMnO}_3$  thin films has been investigated in detail by SQUID magnetometry. The magnetization of single-crystals is measured additionally for comparison with that of the thin films. With the results, an approximate phase diagram of  $\text{HoMnO}_3$  has been constructed.

## 5.1 Temperature dependence of magnetization

### 5.1.1 Curie-Weiss law

From the inverse susceptibility data ( $\chi^{-1} = H/M$ ) vs. temperature, Curie-Weiss extrapolations have been done to calculate the paramagnetic Curie temperatures ( $\theta$ ). As discussed in §1.4, the paramagnetic Curie temperature  $\theta$  is a direct measure of the strength of the spin interactions. A positive value of  $\theta$  indicates a ferromagnetism-dominant interaction. On the other hand, if  $\theta$  is negative, it can be postulated that antiferromagnetism is the dominant interaction. When  $\theta$  is zero, all the interactions between magnetic moments cancel out, i.e. the Weiss mean field is zero in this

direction.

In  $\text{HoMnO}_3$  the magnetization at low temperature can be assumed to essentially originate from the  $\text{Ho}^{3+}$  moments, since the triangular ordering of the  $\text{Mn}^{3+}$  spins results in a zero net moment. Therefore, the paramagnetic Curie temperature recorded below  $T_N$  can serve as a measure of  $\text{Ho}^{3+}$  interactions as suggested by Lorenz *et al.* [Lorenz 05]. (Below the Néel temperature of the  $\text{Mn}^{3+}$  sublattice,  $\text{Ho}^{3+}$  ions can still be treated as paramagnetic, since they order at much lower temperature  $T_{Ho}$ .)

Figure 5.1 shows the temperature-dependent inverse susceptibility of a thin film (left) and a single-crystal (right). For the films, as the magnetic field becomes stronger, the substrate influence also becomes stronger. As a result, the inverse susceptibility seems not to follow the Curie-Weiss law anymore. However, in low magnetic field the behavior is Curie-Weiss-like, i.e. curves are approximately linear nearly down to  $T_{Ho}$  for both in-plane ( $\mathbf{H} \parallel \mathbf{a}$ ) and out-of-plane ( $\mathbf{H} \parallel \mathbf{c}$ ) field directions.

By linear extrapolation, the film reveals an in-plane paramagnetic Curie temperature  $\theta_a = 0$  K within the error limit which is less than  $\pm 1$  K, confirming that the total exchange field acting on the  $\text{Ho}^{3+}$  moments in the  $ab$  plane vanishes. This is a consequence of the geometrically frustrated triangle sublattice structure perpendicular to the  $c$ -axis. The value  $\theta_a$  agrees with bulk data (Fig.5.1(b) and [Lorenz 05]). On the other hand, along the  $c$ -axis, the value  $\theta_c = -5$  K is derived below 50 K. Since the  $\theta_c$  value of a single-crystal is about  $-10$  K (Tab.5.1), the films reveal a weakened antiferromagnetic coupling of  $\text{Ho}^{3+}$  moments as compared to single-crystals

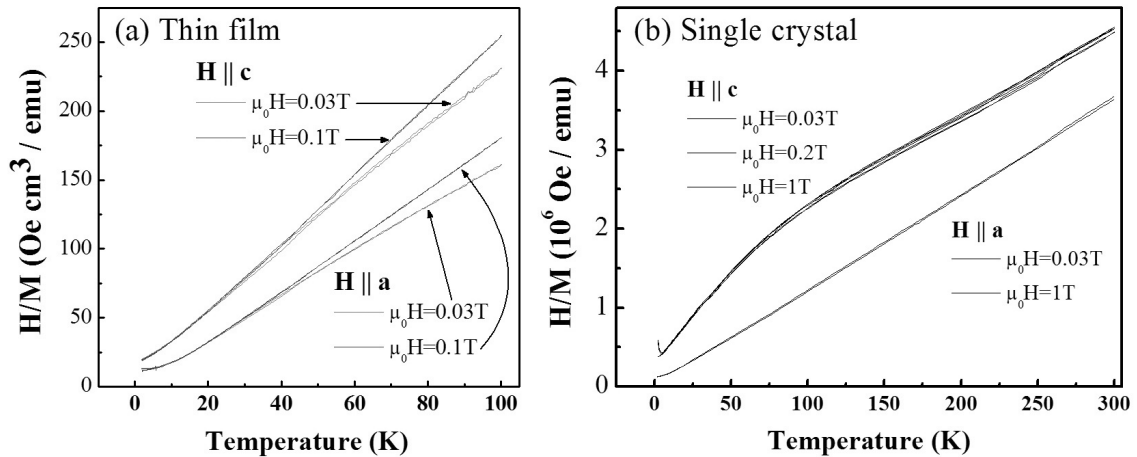


Figure 5.1: Inverse susceptibility of a 240 nm thick  $\text{HoMnO}_3$  thin film (left) and single-crystal (right) measured along  $\mathbf{H} \parallel \mathbf{a}$  and  $\mathbf{H} \parallel \mathbf{c}$  directions.



Table 5.1: The paramagnetic Curie temperature deduced by an extrapolation of the H/M vs. T curve. The literature values of a single-crystal are taken from Lorenz *et al.* [Lorenz 05].

Paramagnetic Curie temperatures ( $\theta$ )			
Field direction	Thin films	Single-crystal	Literature (Crystal)
H    a	0K	0K	0K
H    c	-5K	-10K	-12K

[Kim 07c].

The reason why the antiferromagnetic Ho coupling in films is weakened is most likely the enlarged lattice parameters. As shown in §4.2 the lattice parameters of the films vary with film thickness. The  $c$  and the  $a$  lattice parameters of a 240 nm thick film are 0.9 % and 1.8 % larger, respectively, than those of a single-crystal. These enlarged lattice parameters are likely to reduce the superexchange interactions, because the superexchange sensitively depends on bond lengths.

### 5.1.2 Spin reorientation temperature, $T_{SR}$

By magnetization measurements, the spin reorientation temperature  $T_{SR}$  has been detected in a single-crystal with H||c. Figure 5.2 shows the inverse susceptibility H/M at  $\mu_0H = 0.1$  T. These data form a straight line in agreement with the Curie-Weiss law, but, at one point, a tiny cusp (circle) is seen at around 33 K. The H/M line exhibits an abrupt jump (right inset) and the derivative (left inset) shows a clear discontinuity at  $T_{SR}$ . The discontinuity at 33 K becomes small and smeared out as the magnetic field increases beyond 1 T. The magnetic field dependence of  $T_{SR}$  is shown in Fig.5.3.  $T_{SR}$  shows a decreasing tendency as the magnetic field rises. Similarly, a decrease of  $T_{SR}$  with magnetic field has been revealed recently by dela Cruz *et al.* [dela Cruz 05]. Their results approximately fall onto the solid line in Fig.5.3.

In contrast to  $T_{SR}$  of single-crystals,  $T_N$  could not be detected.  $T_N$  and  $T_{SR}$  of single-crystals have been reported so far measured by various other methods. However, by magnetization measurements, it is known to be difficult to observe  $T_N$  because of the large paramagnetic contribution of the rare-earth ions.

During the measurements of thin films, neither  $T_N$  nor  $T_{SR}$  of the  $Mn^{3+}$  sublattice have been observed. In the case of films, the determination of  $T_N$  and  $T_{SR}$

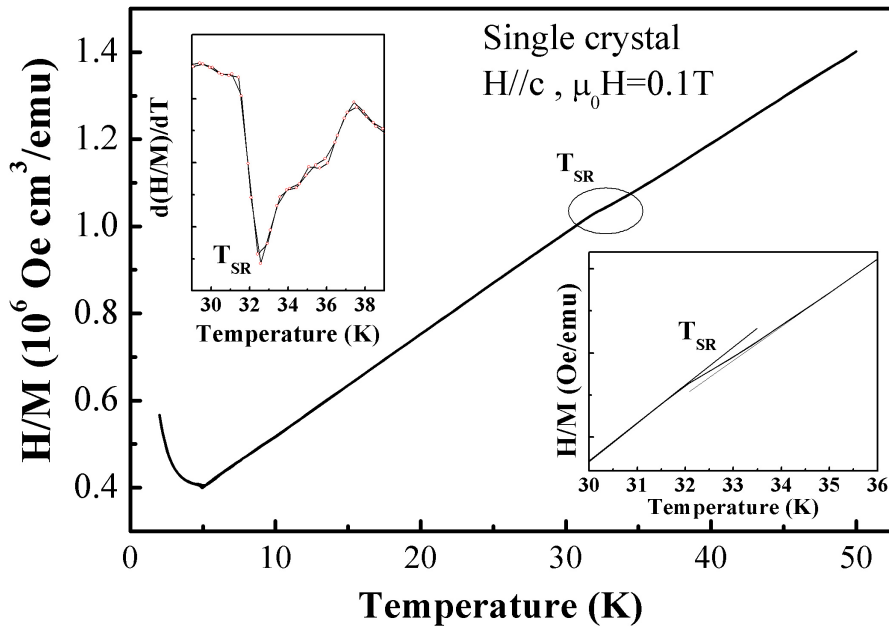


Figure 5.2: Inverse susceptibility of a single-crystal measured with  $H \parallel c$  (left inset: derivative of  $H/M$ , right inset: enlargement of a cusp). The spin reorientation temperature ( $T_{SR}$ ) is detectable with a small cusp.

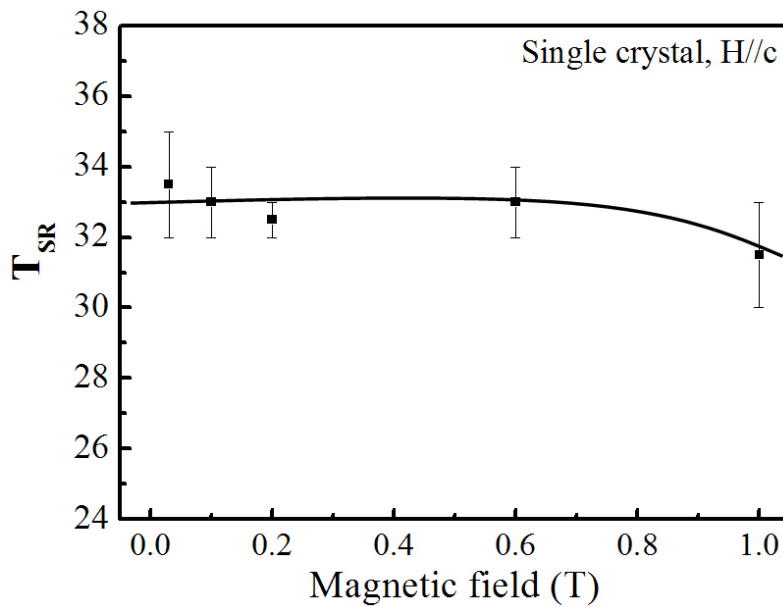


Figure 5.3: Magnetic field dependence of  $T_{SR}$ . Above 1 T, the anomaly becomes unclear in magnetization measurements.

from magnetization data is supposed to be even more difficult due to the substrate contribution and the small film volume. This may be due to the resolution limit of the SQUID measurements, i.e. a small signal change due to the  $\text{Mn}^{3+}$  spin rotation cannot be detected. In a recent study on neutron scattering for  $\text{HoMnO}_3$  films it has also been argued that the variation of the susceptibility at  $T_N$  is quite low and hardly detectable for thin films [Gélard 08].

### 5.1.3 Low temperature anomalies

#### Thin films

Although  $T_N$  and  $T_{SR}$  are not visible in films, low temperature anomalies below 5 K related to the  $\text{Ho}^{3+}$  ordering have been detected.

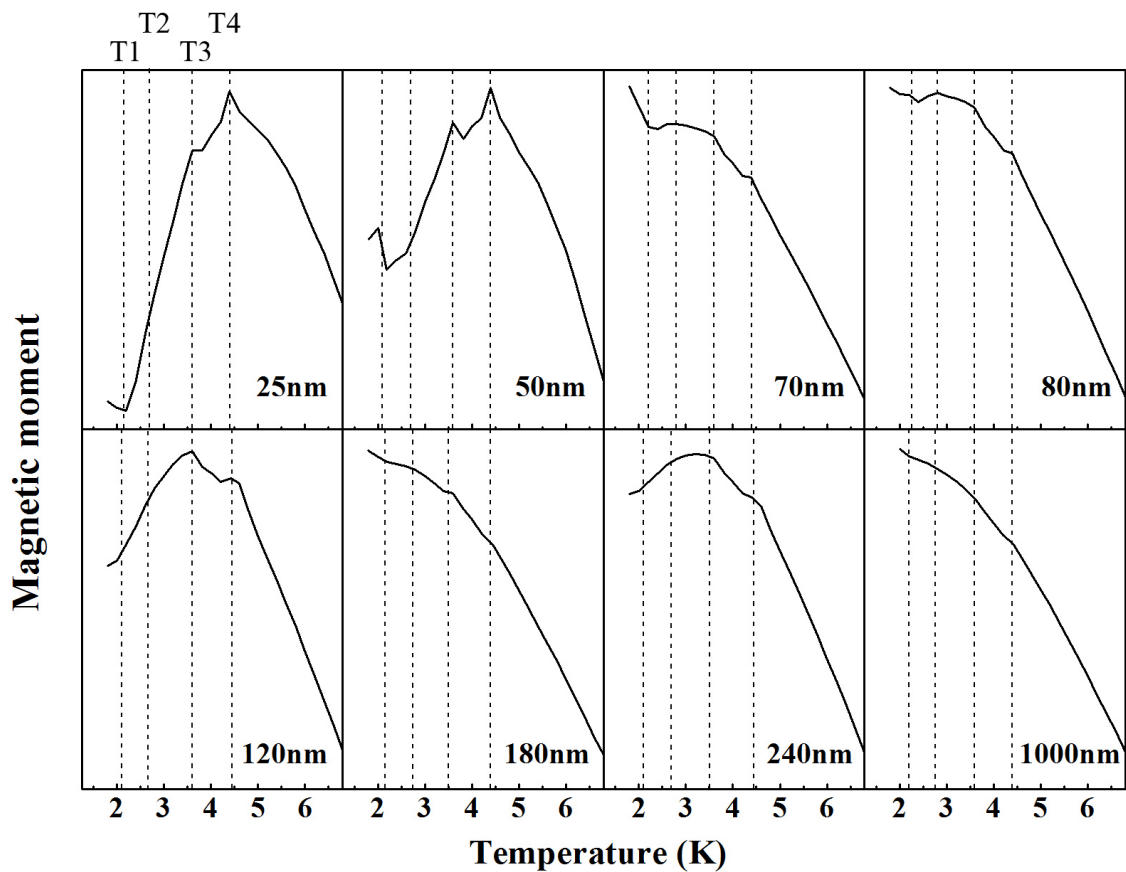


Figure 5.4: Low temperature magnetization of films of various thicknesses. The four distinct anomalies below 5 K are clearly distinguishable.  $\mu_0 H = 0.1$  T,  $H \parallel a$

Figure 5.4 shows magnetization measurements  $M(T)$  of films of various thickness, measured at  $\mu_0 H = 0.1$  T in in-plane direction ( $H \parallel a$ ). The four distinct anomalies, which are named T1, T2, T3 and T4 from low to high temperature, respectively, can be seen. As discussed earlier, the total magnetic moment is assumed to essentially originate from  $\text{Ho}^{3+}$  ions at low temperature, because the  $\text{Mn}^{3+}$  magnetic moments are strongly coupled in the complicated antiferromagnetic triangular structure and may only slightly tilt out of the hexagonal plane. Hence, the anomalies shown in Fig.5.4 are supposed to reflect  $\text{Ho}^{3+}$  spin ordering and/or reorientation. Since the magnetic  $\text{Ho}^{3+}$  sublattice shows a very rich low temperature phase diagram for bulk samples, it is not surprising to find different phases in thin films (refer to the phase diagrams, Fig.2.7 and Fig.2.8).

The four anomalies are located approximately at  $T1 = 2.15$  K,  $T2 = 2.7$  K,  $T3 = 3.5$  K and  $T4 = 4.5$  K. These points are distinguished by the change in slope of the magnetization curve  $M(T)$ . In all samples, above  $T4$ , the magnetization slope ( $dM/dT$ ) is maximum. At  $T4$ , the slope decreases somewhat in a way as expected

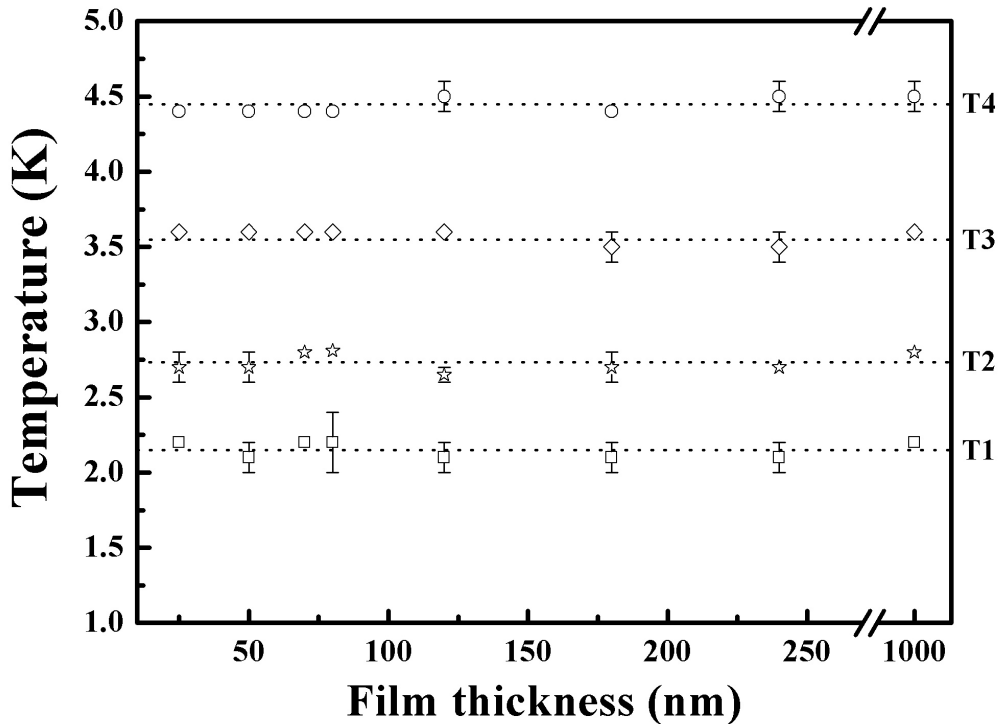


Figure 5.5: Thickness dependence of the four anomalies. The low temperature anomalies do not vary with film thickness.

for an antiferromagnetic ordering of  $\text{Ho}^{3+}$  ions. The slope changes again at T3 with a further reduction and a third time in the same way at T2. Finally, at T1, the slope ( $dM/dT$ ) increases again.

The reduced magnetic moment at T4 is consistent with the fact that  $\text{Ho}^{3+}$  is known to order antiferromagnetically below this temperature [Lonkai 02], even though the bulk  $T_{\text{Ho}} \sim 5\text{K}$  is slightly larger than T4. Likewise, the further diminutions at T3 and T2 indicate that the  $\text{Ho}^{3+}$  order becomes more antiferromagnetic. In contrast, at T1 the  $\text{Ho}^{3+}$  order becomes *less antiferromagnetic*.

The magnitude of the slope change at the anomalies varies with the film thickness (Fig.5.4). At a small thickness, the slope changes more strongly than at a large thickness. The thickness dependence of the anomaly temperatures is shown in Fig.5.5. The temperatures T1, T2, T3 and T4 vary slightly among the films, but it seems hard to find a clear tendency. Rather, the anomaly temperatures only slightly fluctuate with film thickness.

## Field dependence of the anomalies

At low temperatures, the magnetization depends strongly on the measurement conditions, i.e. zero-field-cooling (ZFC) or field-cooling (FC) and in-plane ( $H\parallel a$ ) or out-of-plane ( $H\parallel c$ ) magnetic field directions. The low temperature anomalies are suppressed after field-cooling. Typically, they are more pronounced for low magnetic fields with  $H\parallel a$ . Figure 5.6 shows the differences depending on the conditions.

The  $M(T)$  measurements show a splitting between the ZFC and the FC curves, while no difference between ZFC and FC has been found in bulk  $\text{HoMnO}_3$  polycrystalline samples [Muñoz 01]. The splitting depends on the magnetic field. It is dominantly visible at low magnetic fields. The divergence starts at higher temperature as the magnetic field decreases. As the magnetic field increases, the difference between ZFC and FC becomes smaller and vanishes at about  $\mu_0 H = 1\text{ T}$  for both magnetic field directions. This tendency is summarized in Fig.5.7.

A similar ZFC and FC divergence has been recently reported in hexagonal  $\text{REMnO}_3$  thin films, e.g.  $\text{DyMnO}_3$  [Lee 07] and  $\text{HoMnO}_3$  [Murugavel 07], both on YSZ(111) substrates, even though the temperature range is rather different. In these reports, the ZFC and the FC splitting start at a much higher temperature, i.e. 50 – 60 K. Furthermore, the ZFC curve shows an additional kink at 38 – 40 K in these studies. The authors of both papers assigned the splitting starting point to  $T_N$  and the successive kinks to  $T_{SR}$  of  $\text{Mn}^{3+}$  sublattice.

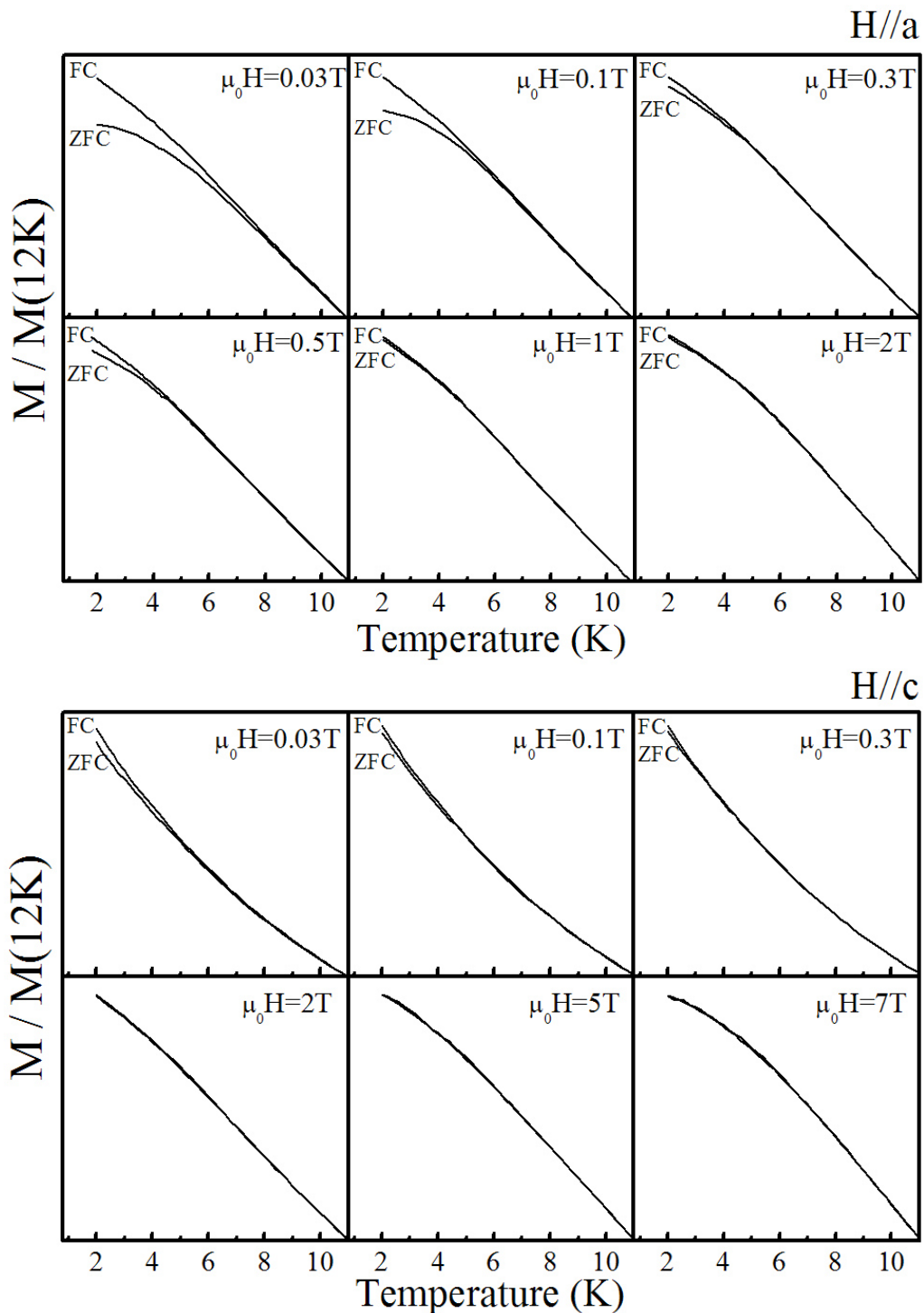


Figure 5.6: Magnetization for the 1000 nm thick film after zero-field-cooling (ZFC) and field-cooling (FC) in both  $H\parallel a$  (upper panel) and  $H\parallel c$  (lower panel) field directions. The low temperature anomalies are pronounced in ZFC with  $H\parallel a$ .

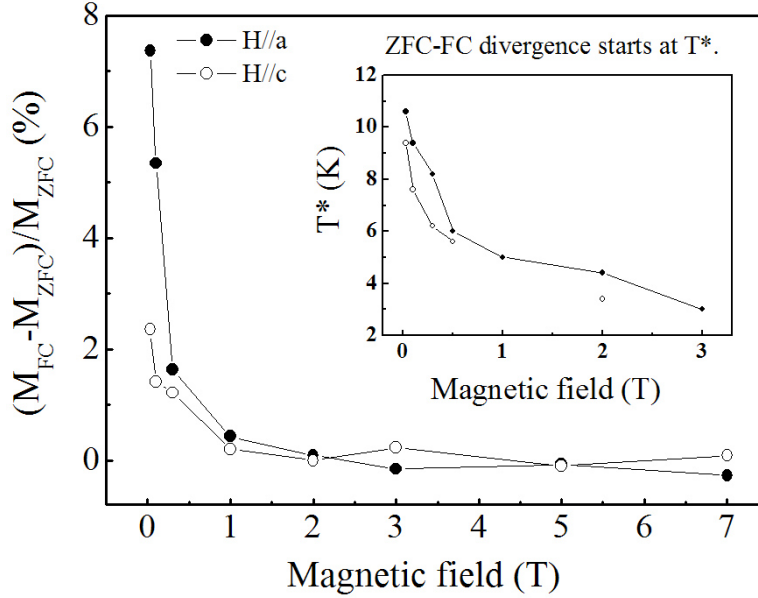


Figure 5.7: Magnetic field dependence of the difference between ZFC and FC magnetization at 2 K for the 1000 nm thick film. Inset: temperature  $T^*$  where the ZFC and the FC curves split.

Murugavel *et al.* [Murugavel 07] proposed a *spin-glass* behavior due to some structural disorder which produces local variations of exchange interactions as possible origin of the divergence between ZFC and FC magnetization at low temperature. The assumption may be valid in this work, too, however, one inconsistency is that the field-dependent magnetization loops of the films recorded at 2 K for both field directions have zero remanence (no spontaneous magnetization, see Fig.5.13(a)) which is not typical for a spin glass state. The mechanism of the divergence of the magnetization curves is not fully understood yet.

Besides the ZFC / FC difference, the magnetization curves depend on the magnetic field direction (Fig.5.6). The splitting between ZFC and FC is more pronounced in H//a than in H//c. Likewise, the low temperature anomalies are more pronounced in H//a than in H//c. This implies that the phase diagram would be different for different magnetic field directions. Actually, films as well as single-crystals have a somewhat different phase diagram depending on the field direction (see §5.3).

To construct a  $(T, H)$  phase diagram, the magnetic field dependence of the low temperature anomalies has been measured. The anomalies are detected at the low field range,  $\mu_0 H \leq 0.5$  T, but become unclear at a higher magnetic field. With these measurements, the traces of T1, T2, T3 and T4 have been confirmed. These anomalies vary slightly according to the applied magnetic field as shown in Fig.5.8. T4 can be assigned as  $T_{Ho}$  with a slightly reduced value compared to single-crystals. In consideration of the magnetization curves, the antiferromagnetic interactions be-

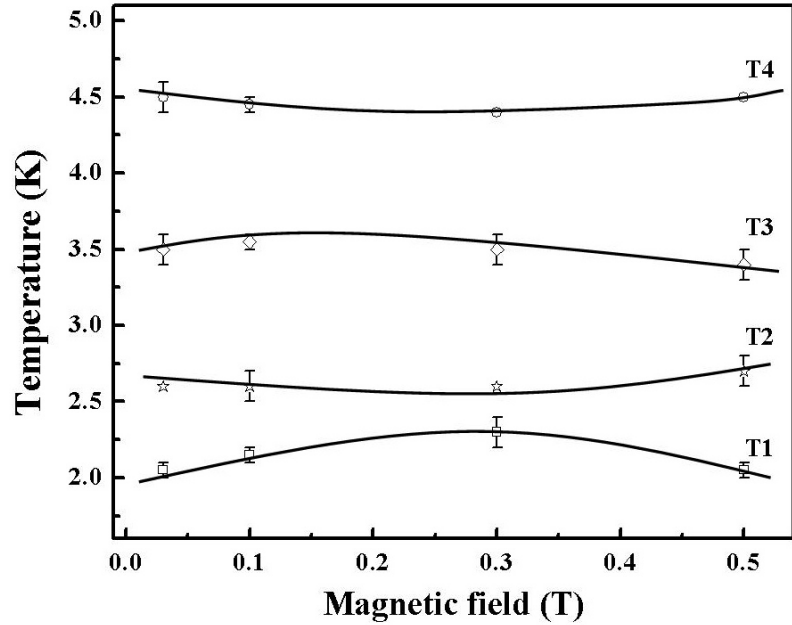


Figure 5.8: The low temperature phase diagram is constructed by variations of the four anomalies below 5 K, i.e. T1, T2, T3 and T4.

come stronger as the temperature goes down from T4 to T2. On the other hand, at T1, the AFM interactions of the  $\text{Ho}^{3+}$  change to be weaker.

Only few results are published on the magnetization measurements of single-crystals so far. Sugie *et al.* [Sugie 02] showed low temperature anomalies only at  $\mu_0 H = 1$  T. Lorenz *et al.* [Lorenz 05] published the field dependence of the anomalies in the magnetic field range from 0.5 T to 2 T. In comparison with the single-crystals' data, the T3 and T4 anomalies seem to resemble those in Sugie's paper [Sugie 02], but T1 and T2 are missing in that paper. The traces of T1 and T4 seem compatible with those in Lorenz's paper [Lorenz 05], however, here the T2 and T3 anomalies are missing. Interestingly, in films, the four anomalies show up together and exhibit a magnetic field dependence.

## Single-crystals

Figure 5.9 shows the low temperature magnetization of a single-crystal at various magnetic fields. The magnetization curves are normalized with the magnetic moment at 8 K, respectively. For the case of a single-crystal, the magnetization anomalies have been detected only in  $H \parallel c$  in contrast to the film's case. No ZFC and FC curve splitting has been observed except for a small hysteresis at about 5 K in a low magnetic field. Between 5 K and 8 K, the curves of all magnetic fields roughly coincide following a Curie-Weiss-type behavior. The curves start to deviate



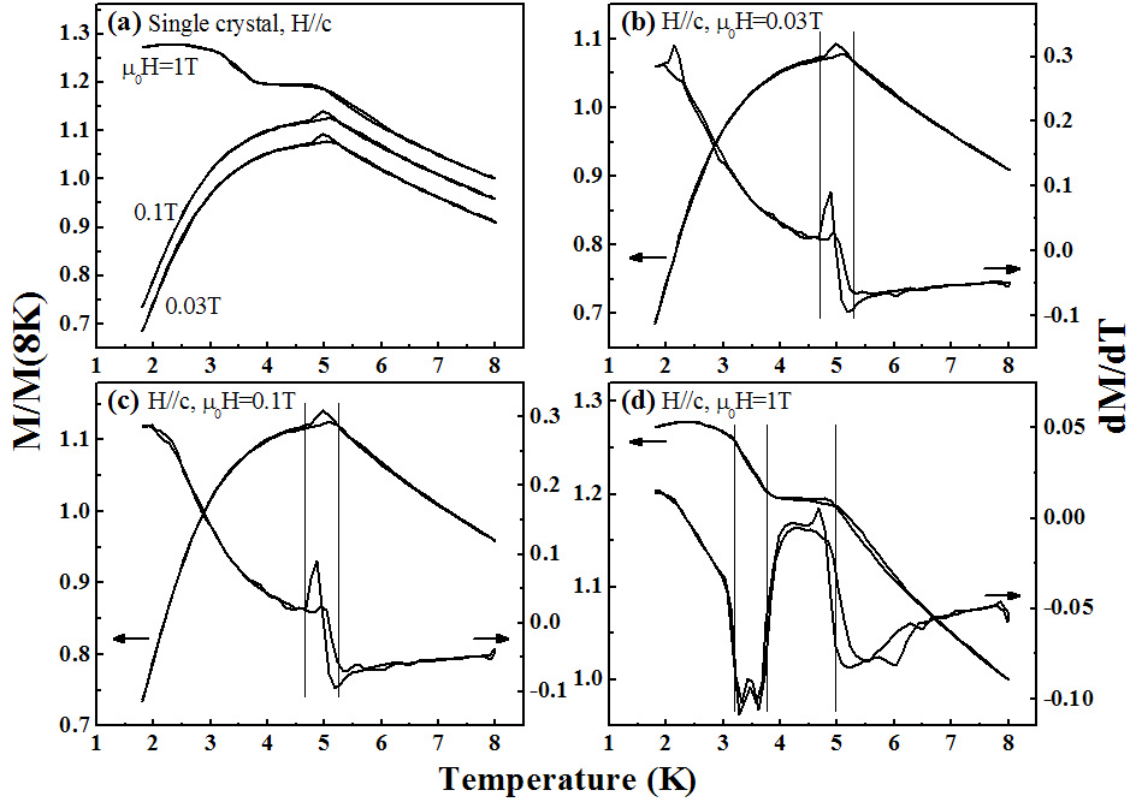


Figure 5.9: Low temperature magnetization measured in different magnetic fields for a  $\text{HoMnO}_3$  single-crystal. Magnetization curves in panel (a) are shifted for clarity.

from 5 K where long-range  $\text{Ho}^{3+}$  magnetic moment comes into play. This can be a direct proof of the  $\text{Ho}^{3+}$ 's influence on the magnetization behavior below  $T_{Ho}$ .

The magnetization curves behave differently depending on the magnetic field. The data measured at  $\mu_0H = 0.03$  T and 0.1 T show a small hysteresis around 5 K and decrease continuously towards low temperature, revealing the antiferromagnetic order of the  $\text{Ho}^{3+}$  magnetic moments. On the other hand, the data recorded at higher field ( $\mu_0H = 1$  T) reveal a plateau of  $M$  at  $3.8 \text{ K} < T < 5 \text{ K}$  followed by another rise of  $M$  to another plateau below 3.8 K.

These observations are in agreement with the bulk phase diagram measured in the  $H\parallel c$  field direction (Fig.2.8). According to the phase diagram, the hysteresis observed at 5 K is expected due to the phase transition from the HT2 to the INT phase. The anomalies at  $\mu_0H = 1$  T are related to a dome-shaped low-temperature (LT1) phase, present below 4 K in the field range of about 0.5 – 2 T. The transitions from the HT2 phase to the INT phase and to the LT1 phase correspond to 5 K

and 3.8 K, respectively. According to the measurements, the LT1 phase is expected to have a larger magnetization than the HT2 and the INT phase in single-crystals [Kim 07b].

The crystal data for  $H||a$  (not shown) exhibit a continuous increase of  $M$  towards low  $T$  for both applied magnetic fields ( $\mu_0H = 0.01$  T, 1 T) without any clear anomalies. This finding indicates that the field-induced in-plane magnetization from tilting  $\text{Ho}^{3+}$  moments towards the plane is weakly affected by the antiferromagnetic  $\text{Ho}$  ordering along the  $c$ -axis below 5 K [Kim 09].

## 5.2 Magnetic field dependence of the magnetization

The magnetic field dependence  $M(H)$  has been investigated up to 7 T in both field directions. For comparison, the single-crystal has also been measured. A magnetic-field-induced phase transition has been detected in films as well as in the single-crystal. Below 5 K, such a transition is expected in agreement with the phase diagram (Fig.2.8).

### 5.2.1 Magnetic field-induced phase transition

#### In-plane field direction ( $H||a$ )

Figure 5.10 shows  $M(H)$  magnetization loops of the single-crystal recorded at various temperatures  $T \leq 8$  K in the  $H||a$  direction. A transition is observed at 2 K and 4 K, although Lorenz *et al.* [Lorenz 05] stated that no distinct anomaly could be detected in  $H||a$ . The  $M(H)$  loop measured at 2 K exhibits a small hysteretic transition in the range of  $\mu_0H = 2$  T – 3.2 T. This hysteresis becomes smaller as the temperature increases. At 4 K, the hysteresis takes the narrowed range of  $\mu_0H = 2.2$  T – 2.6 T. At higher temperature, i.e.  $T \geq 6$  K, the transition is absent.

On the other hand, for the measurement of thin films (Fig.5.11) no anomalies, not even tiny cusps, have been detected for any temperature in the  $H||a$  field direction. This is in line with the fact that films show somewhat suppressed interactions than single-crystals.

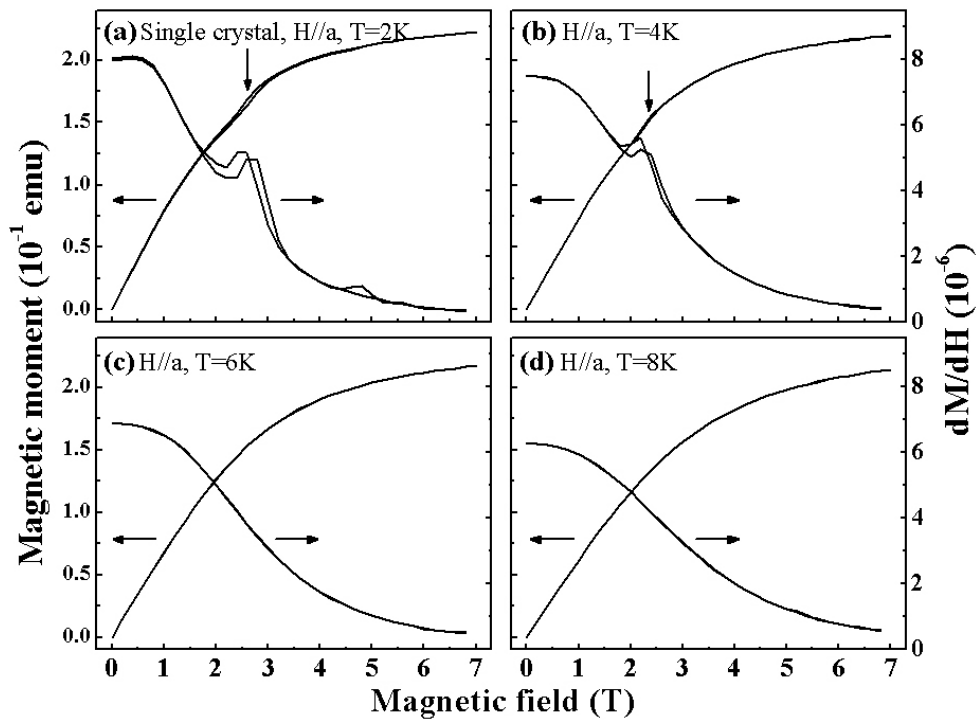


Figure 5.10: Magnetic field dependence of the magnetic moment and its field derivative for a single-crystal in  $H||a$ .

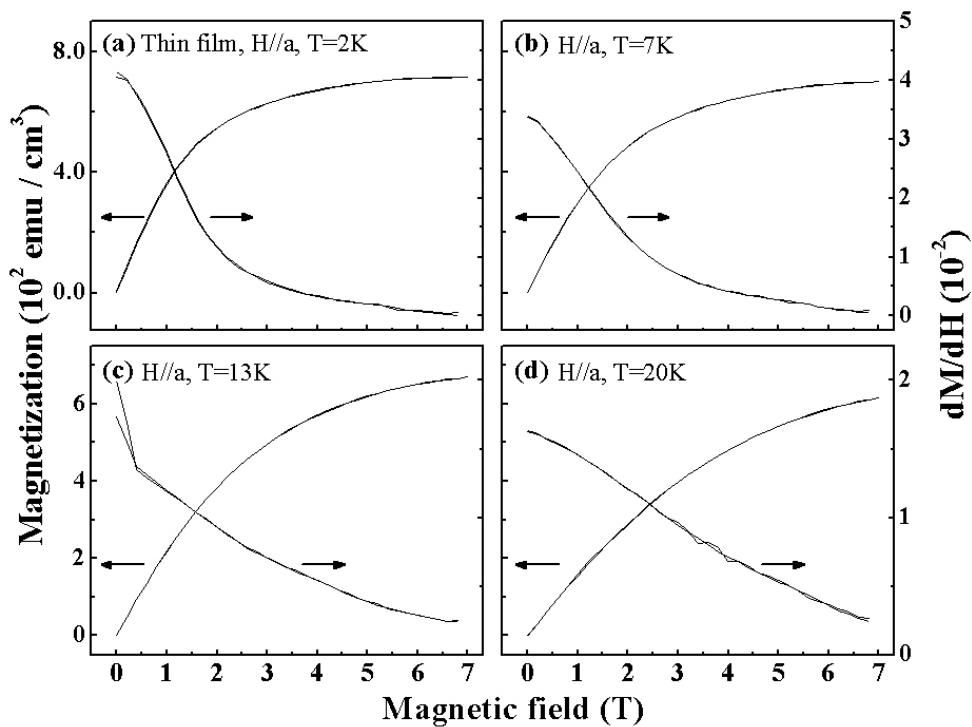


Figure 5.11: Magnetic field dependence of the magnetization and its field derivative for a 1000 nm thick film in  $H||a$ .

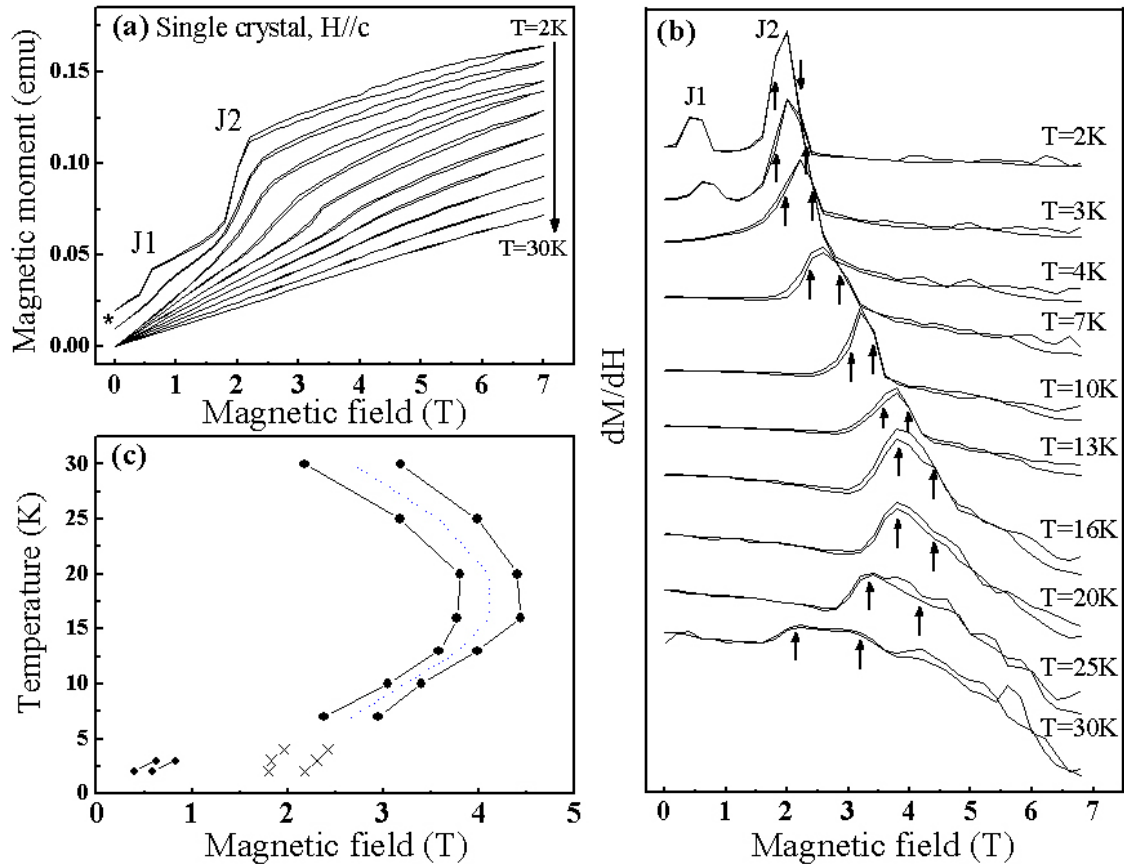


Figure 5.12: Magnetic field dependence of the (a) magnetic moment and (b) its field derivative for a single-crystal in  $H||c$ . The panel (c) shows the trace of J1 and J2. The \* mark in panel (a) indicates a shift for clarity, all curves start at  $M=0$ .

### Out-of-plane field direction ( $H||c$ )

The field-induced phase transitions are more profound for the  $H||c$  direction. Figure 5.12 shows the results of the single-crystal. It shows clear meta-magnetic transitions which change their positions with temperature. At low temperature ( $T \leq 3\text{K}$ ), the magnetization loop shows two distinct jumps (denoted as J1 and J2). As the temperature increases, J1 appears at a little bit higher magnetic field and disappears above 4 K. The other jump, J2, moves towards higher magnetic fields till  $T = 16\text{K}$  and fades away as the temperature increases. This result is more detailed than in the work of Sugie *et al.* [Sugie 02], who showed only one meta-magnetic transition (J2).

With the derivative  $dM/dT$  (Fig.5.12(b)), the shift of J1 and J2 can be clearly

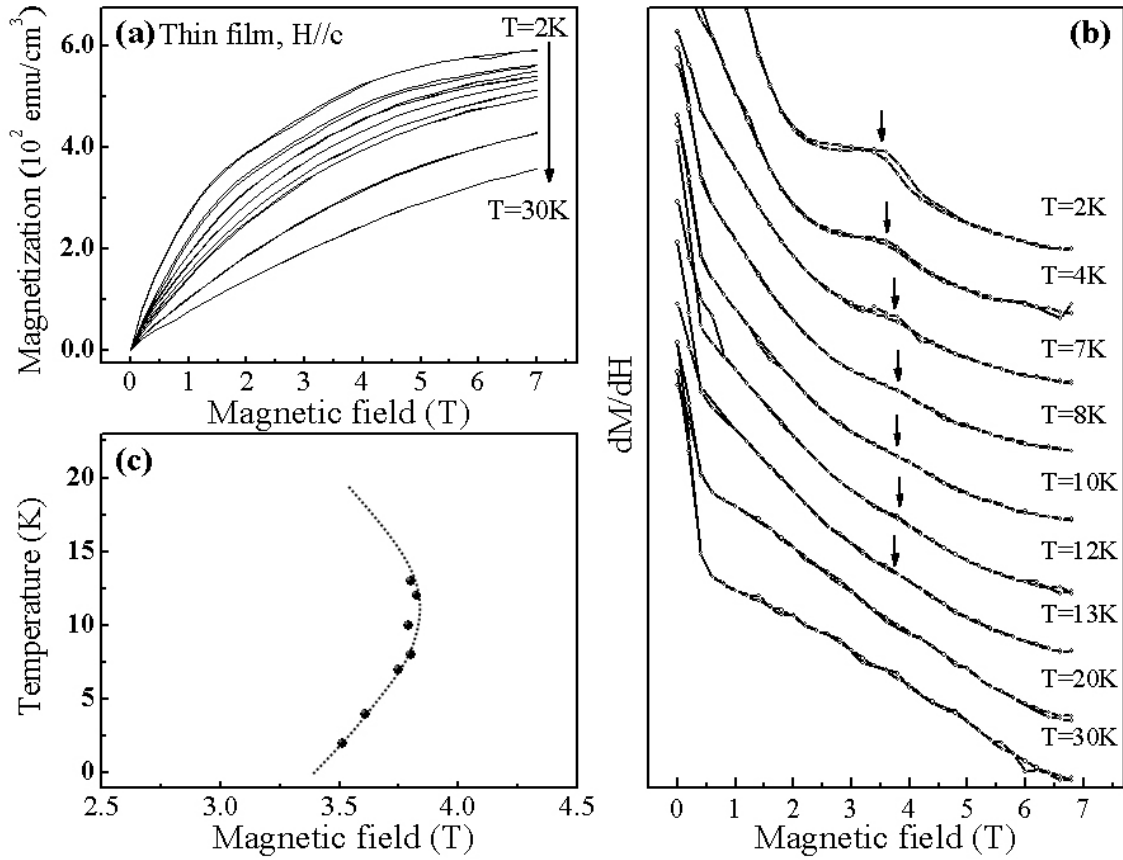


Figure 5.13: Magnetic field dependence of the (a) magnetization and (b) its field derivative for a 1000 nm thick film in H||c. Anomalies from  $dM/dH$  are summarized in the panel (c).

figured out. Obviously, the meta-magnetic transition denoted as J2 describes a curve. As displayed in phase diagrams of single-crystals (see Fig.2.8),  $\text{HoMnO}_3$  has a concave phase in the temperature range of  $5 \text{ K} - T_{SR}$  and magnetic field range of  $0 - 4 \text{ T}$ . As depicted in Fig.5.12(c), the trace of J2 above 5 K confirms the concave phase with the intermediate (INT) phase. As the temperature increases, the boundary of this concave phase is expected to be joined to  $T_{SR}$  in the end. The low temperature region  $T \leq 5 \text{ K}$  seems rather complex. Figure 2.8 indicates the presence of a low-temperature dome-shaped phase (LT1) between  $\mu_0 H \sim 0.4 - 2 \text{ T}$ . The transitions J1 and J2 for  $T \leq 3 \text{ K}$  seem to reflect the entrance and exit for this phase.

For a representative rather thick film, these anomalies seem quite suppressed as shown in Fig.5.13. A weak anomaly appears near  $\mu_0 H = 3.5 \text{ T}$  at 2 K which may be

of the same nature as the 2 T transition in the crystal (J2). The low field transition of the single-crystal (J1) has not been detected for the films.

The field-induced phase transition fades away with increasing temperature more quickly than in the crystal. The trace of the phase transition is also concave, similar to that for the single-crystal (Fig.5.13(c)). The INT phase, observed in the single-crystal, is hard to observe in the film due to the tiny anomalies in  $M(H)$ . Assuming that the thin film also shows the concave phase (Fig.5.13), the phase is shifted *left-downwards* to lower temperature and slightly lower magnetic field if compared to the single-crystal's position. The absence of the J1 transition hints towards a suppressed and/or shifted LT1 phase in thin films. Thus, the films show a modified magnetic phase diagram with respect to single-crystals.

## 5.2.2 High-field transition of single-crystals

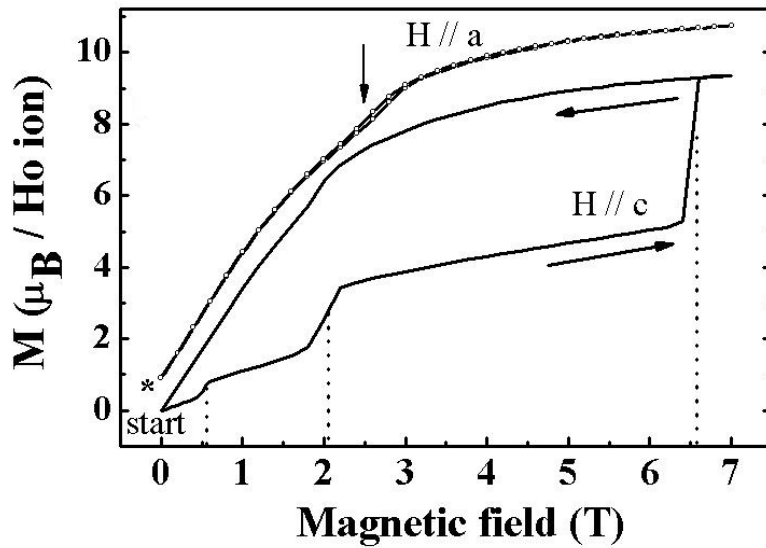


Figure 5.14: Magnetization in dependence on applied magnetic field direction for a single-crystal [Kim 09]. (\* indicates a shift for clarity, all curves start at  $M=0$ .)

Figure 5.14 compares  $M(H)$  loops for both  $H||a$  and  $H||c$  field directions of another single-crystal measured at 2 K. The in-plane magnetization ( $H||a$ ) shows a tiny anomaly with a weak hysteresis at about  $\mu_0 H = 2.5$  T which is identical to that in Fig.5.10. For  $H||c$ , *three* distinct steps of the magnetization can be seen at 0.5 T, 2 T and 6.5 T. The first two are well-matched with the previous measurements (Fig.5.12), by the way, the last one is remarkable. After the third phase transition at 6.5 T, the out-of-plane magnetization becomes almost equal to the in-plane magnetization of the crystal and adopts a value of  $9.5 \mu_B / \text{Ho ion}$  which is not far from the ionic magnetic moment of  $\text{Ho}^{3+}$  of  $10.6 \mu_B$ . Hence, the sample is close to the

ferromagnetic alignment of the Ho magnetic moments along the  $c$ -axis above 6.5 T. This is, to our knowledge, the first observation of a third field-induced transition in HoMnO<sub>3</sub>, that leads to the full alignment of Ho moments along the hexagonal  $c$ -axis. With decreasing field the ferromagnetic alignment is reduced gradually, showing no transition back to an antiferromagnetically ordered Ho sublattice. No remanent magnetization is observed, as is the case for all investigated samples. The transition at 6.5 T is not exactly reproducible, but slightly changes with different measurement runs, and for different single-crystal samples [Kim 09].

### 5.3 The HoMnO<sub>3</sub> phase diagram

With the magnetization data discussed above, a rough phase diagram of HoMnO<sub>3</sub> has been constructed (Fig.5.15). Measurement results for single-crystals (variation of  $T_{SR}$  (Fig.5.3), low temperature anomalies (Fig.5.9), field-induced phase transitions (Fig.5.10, Fig.5.12) and high-field phase transitions (Fig.5.14)) and films (low-temperature anomalies (Fig.5.8) and field-induced phase transitions (Fig.5.13)) are included.

For the single-crystal the known phase diagram (Fig.2.8) is confirmed. Additionally, a new transition at 2 K and  $\sim 6.5$  T has been detected in this work. The high-field phase is characterized by a ferromagnetic alignment of the Ho<sup>3+</sup> magnetic moments.

The direction of the magnetic field has some influence on the transition between the two low-temperature phases, LT1 and LT2, as visible in Fig.5.15(b). The transition shifts to a higher field for the in-plane field direction ( $H||a$ ).

For the HoMnO<sub>3</sub> films the spin reorientation transition ( $T_{SR}$ ) of the Mn<sup>3+</sup> sublattice could not be detected. In low fields  $\mu_0H < 0.5$  T, an antiferromagnetic transition of Ho<sup>3+</sup> moments at  $T_{Ho}$  is obvious in temperature-dependent magnetization measurements (zero-field cooled), revealing a somewhat lowered antiferromagnetic ordering temperature compared to the single-crystal. Several transitions follow for  $T < 4.5$  K in a systematic way as shown in Fig.5.15(c). Possibly, the LT1 phase region that contains several phases in crystals, is shifted to lower fields in the films. Field-dependent data ( $M(H)$ ) between 2 K and 13 K reveal a curved phase boundary that is similar to that of the concave HT2 phase below  $T_{SR}$  in single-crystal. Therefore, the HT2 phase may be present in the films (even though a detection of  $T_{SR}$  failed), and it is shifted to lower temperatures and slightly lower fields.

All magnetic phase transitions in the films have been found to be less pronounced

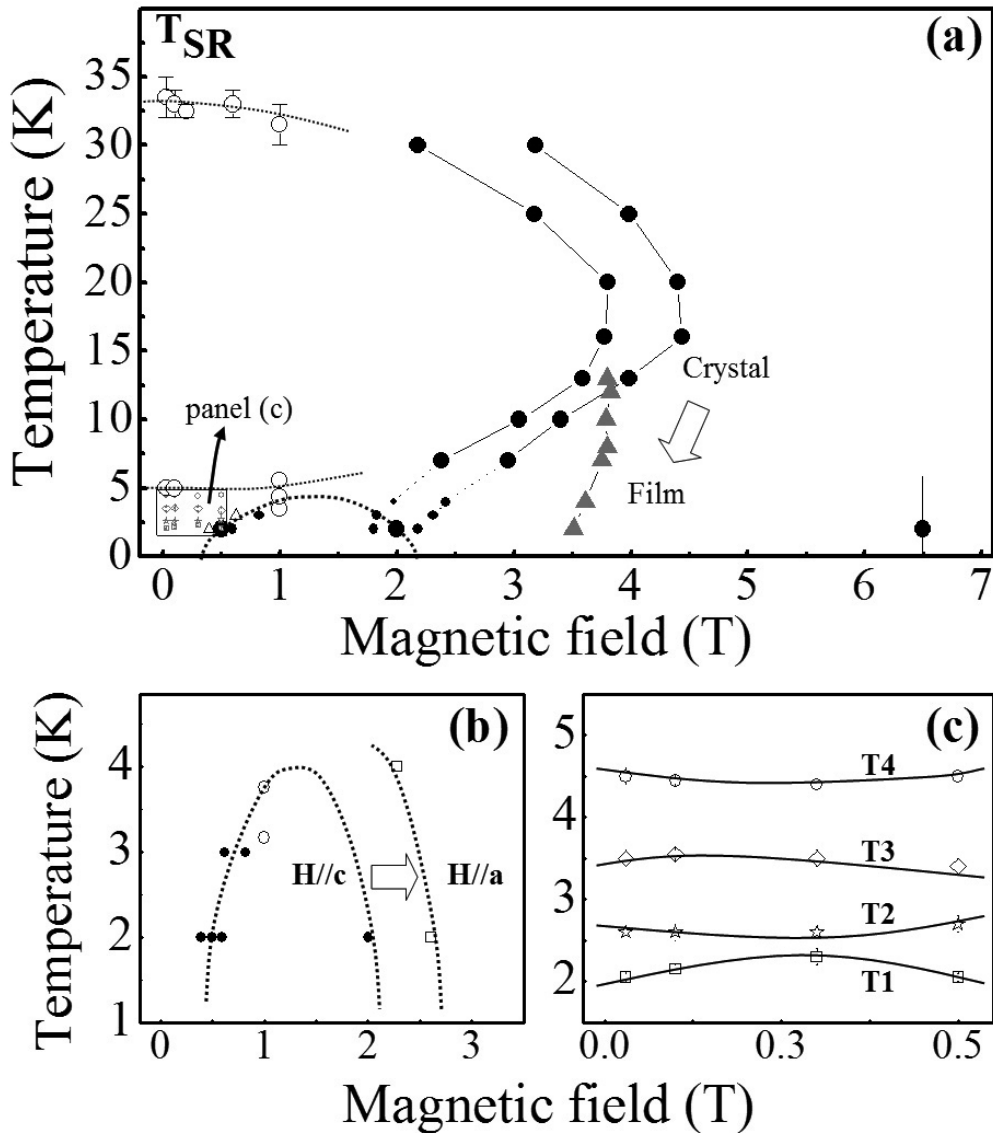


Figure 5.15: A rough phase diagram of  $\text{HoMnO}_3$ . (a) single-crystal (circle) and film (triangle) data from temperature-dependent (open symbols) and field-dependent (closed) magnetization measurements. (b) Comparison of low-temperature data of the single-crystals for both field directions. (c) Low-temperature low-field ( $\text{H}\parallel\text{a}$ ) anomalies of films (replotted from Fig.5.8)



(a smaller change of magnetization is observed) than in the single-crystals. For this reason, some of the phase boundaries could not be detected. It is difficult to understand the modified phase diagram of films based on magnetization data alone. The shifts of  $T_{Ho}$  and the HT2 phase towards lower temperature and lower field are in agreement with a weaker antiferromagnetic  $\text{Ho}^{3+}$  interaction in films, as also observed from the reduced paramagnetic Curie temperature (§5.1.1).

## 5.4 Summary

The low temperature magnetization of hexagonal  $\text{HoMnO}_3$  films as well as of single-crystals has been investigated. Some distinct differences between films and single-crystals have been revealed. The differences are likely to arise essentially from the lattice parameter enhancement in the films that affects all magnetic superexchange interactions in this highly frustrated material.

The Néel temperature and the spin reorientation temperature of  $\text{Mn}^{3+}$  could not be observed in thin films. The magnetization of the single-crystal shows very weak anomalies at these transitions; so the low volume of the films, the additional substrate contribution and the resolution limit of the SQUID measurements have prevented the detection of such transitions.  $T_{SR}$  has been found in single-crystals in the  $\text{H}\parallel\text{c}$  field direction at 33 K.

In contrast to the  $\text{Mn}^{3+}$  antiferromagnetic ordering, the  $\text{Ho}^{3+}$  magnetic ordering is clearly visible in magnetization measurements. According to the Curie-Weiss extrapolation, it turned out that the films have a weakened antiferromagnetic interaction of  $\text{Ho}^{3+}$  moments along the  $c$ -axis. This may be due to the magnetic superexchange modification resulting from enlarged lattice parameters of the films. On the other hand, none of the films revealed a remanent magnetization for  $T \geq 2$  K, as checked for both orientations of the magnetic field ( $\text{H}\parallel\text{a}$  and  $\text{H}\parallel\text{c}$ ).

Splitting of ZFC and FC magnetization is observed at low magnetic fields. The origin of the splitting is not fully understood yet, but could be related to some structural disorder which leads to local variations of the exchange interactions. The magnetization exhibits a somewhat different behavior according to the magnetic field direction. This also forms a deviating phase diagram.

The films show four anomalies for low magnetic fields at  $T \leq 5$  K which are more clearly seen for  $\text{H}\parallel\text{a}$ . These anomalies show a magnetic field dependence with no confirmable film thickness dependence. The low-temperature anomalies are presumably related to a complex  $\text{Ho}^{3+}$  magnetic ordering and/or reorientation.

Single-crystal data show a hysteretic transition around 5 K corresponding to  $T_{Ho}$ , revealing antiferromagnetic ordering of  $Ho^{3+}$  moments. The different behavior of films and single-crystals implies that the phase diagram of films would differ from that of single-crystals.

Field-induced magnetic phase transitions have been found in single-crystals for in- and out-of-plane field directions. Generally, the transitions are more pronounced in the  $H||c$  than in the  $H||a$  direction. For the film, a field-induced phase transition has only been seen in the  $H||c$  measurements. A concave phase in the H–T phase diagram is observed. In comparison with single-crystals, the concave phase of the films is shifted *left-downwards* (to lower T and H). For the single-crystal, a high-field magnetic phase transition at 2 K and  $\mu_0H \sim 6.5$  T has been detected for the first time. Beyond the transition an almost full ferromagnetic alignment of the Ho magnetic moments is established.

With all results on magnetization, a rough phase diagram of  $HoMnO_3$  is constructed. The phase diagram of the single-crystal does not differ much from the published ones. A shift of the LT1 phase depending on the direction of the magnetic field is depicted. Furthermore, the magnetic field dependence of the four low temperature anomalies of films and the shift of the concave phase for the films have been visualized for the first time.

## Chapter 6

# Characterization by SHG

*“Physics would be dull and life most unfulfilling  
if all physical phenomena around us were linear.  
Fortunately, we are living in a nonlinear world.”  
- Y. R. Shen*

Second harmonic generation (SHG), one of the nonlinear optical methods, is a useful tool for investigating magnetoelectrics, because it is sensitive to the breaking of space inversion symmetry by ferroelectric order and the breaking of time reversal symmetry by magnetic order. With this nature, SHG can simultaneously probe two ferroic (electric and magnetic) orders. Furthermore, SHG is able to distinguish antiferromagnetic order which is hard to detect with other techniques. As it is discussed, magnetoelectrics often have antiferromagnetic order, and hexagonal HoMnO<sub>3</sub> has a frustrated triangular antiferromagnetic order of Mn<sup>3+</sup>. Therefore, SHG would be a suitable method for this material.

In this chapter, the results of SHG experiments on multiferroicity in HoMnO<sub>3</sub> thin films will be discussed. This work has been done in cooperation with the group of Prof. M. Fiebig at the University of Bonn, where the SHG measurements were carried out.

## 6.1 Electric polar order

The presence of ferroelectric polar order in the lattice of the HoMnO<sub>3</sub> films has been verified by SHG. As discussed in §1.5, the intensity of the polarized outgoing light produced by electric dipoles is expressed as Eq.1.13:

$$P_i(2\omega) \propto \chi_{ijk}^{ED} E_j(\omega) E_k(\omega).$$

$\chi_{ijk}^{ED}$  is a time invariant third rank tensor related to space inversion symmetry. The ferroelectric order in HoMnO<sub>3</sub> leads to nonzero components of  $\chi_{ijk}^{ED}$  with at least one in  $i$ ,  $j$  or  $k$ . In the ferroelectric state of hexagonal HoMnO<sub>3</sub> (point group  $6mm$ , space group  $P6_3cm$ ), the nonzero electric components are: [Birss 64, Shen 03]

$$\chi_{ijk}^{ED} : \chi_{xxz} = \chi_{xzx} = \chi_{yyz} = \chi_{yzy} ; \chi_{zxx} = \chi_{zzy} ; \chi_{zzz} .$$

With the light incident along the  $c$ -axis ( $\mathbf{k} \parallel z$ ), ferroelectric order contributions are not accessible, since the propagation vector of light  $\mathbf{k}$  and the electric field vector  $\mathbf{E}$  are perpendicular. Hence, the component  $\mathbf{E}_z$  would vanish. Accordingly there is no nonzero component of  $\chi_{ijk}^{ED}$  when  $\mathbf{k} \parallel z$ . To have a nonzero  $\mathbf{E}_z$  component, the HoMnO<sub>3</sub> sample should be rotated by an angle around the  $x$ -axis to get a condition  $\mathbf{k} \not\parallel z$ . In this measurement, the sample is rotated by  $45^\circ$  as shown in Fig.6.1(a) where the contribution of  $\chi_{ijk}^{ED}$  would be maximum.

Fig.6.1(b) shows an electric SH spectrum of a 240 nm film. It was measured slightly above the Néel temperature to avoid interference with the magnetic SH signal. The light polarized in the  $xz$  plane and along the  $y$  axis is denoted  $s$ - and  $p$ - polarized light, respectively. With these notations, four combinations can exist according to the directions of the incoming and outgoing light. In the ferroelectric state the  $s$ -polarized outgoing light ( $s^{out}$ ) is forbidden. In contrast, two  $p$ -polarized outgoing signals ( $p^{out}$ ) appear. One is the case of  $s^{in}-p^{out}$  which corresponds to the

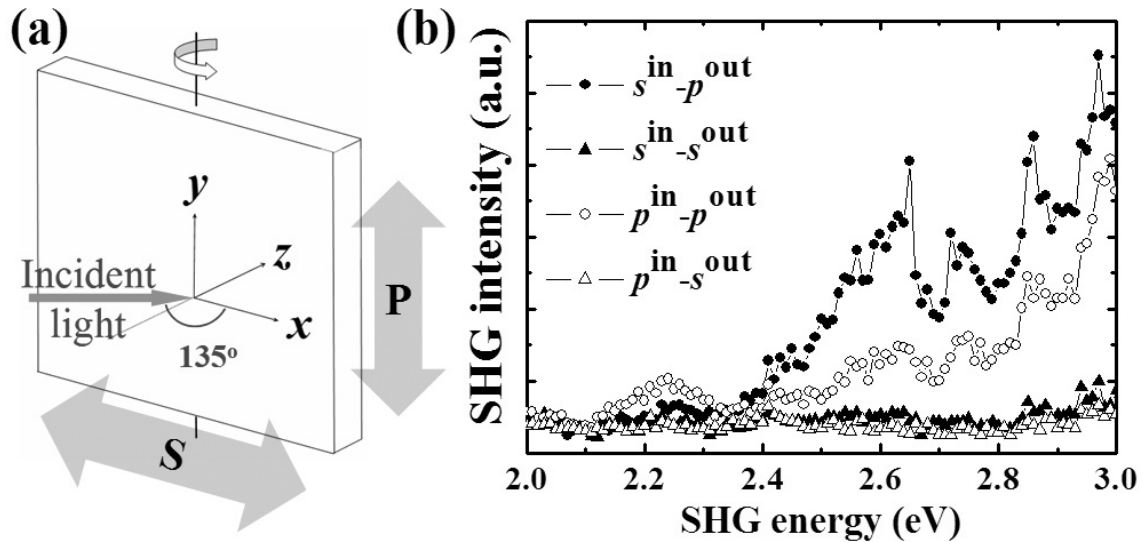


Figure 6.1: (a) A sample orientation scheme of the SHG measurement and (b) the electric second harmonic spectrum measured at 83 K [Kim 07c].

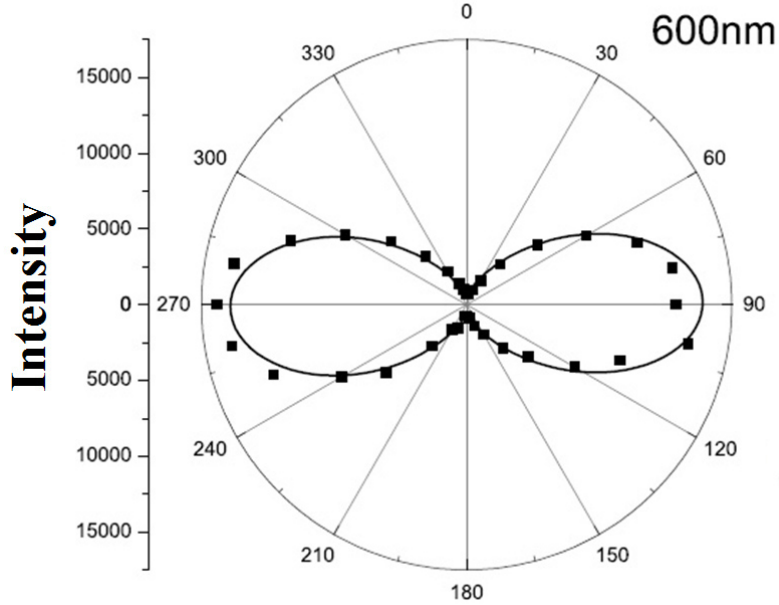


Figure 6.2: The angular-dependent anisotropy measurement of an electric second harmonic signal of a 600 nm HoMnO<sub>3</sub> film measured at  $E_{SH} = 2.75$  eV ( $T = 300$ K) [Kordel 08].

$\chi_{zxx}$  component, the other is the case of  $p^{in}-p^{out}$ , corresponding to a summation of the  $\chi_{zyy}$ ,  $\chi_{yyz}$  and  $\chi_{zzz}$  components.

The  $p^{out}$  spectra show the typical two-peak structure around  $E_{SH} = 2.7$  eV. This is analogous to the  $p^{in}-p^{out}$  SH spectrum of an HoMnO<sub>3</sub> single-crystal. With this similarity of the SH spectra, the ferroelectric polar order in the HoMnO<sub>3</sub> film has been confirmed [Kim 07c].

A 600 nm HoMnO<sub>3</sub> film was measured recently [Kordel 08]. In this measurement, the two-peak behavior around 2.7 eV has also been detected (not shown here). An additional anisotropy measurement shows the two-lobes shape of the SH intensity at  $E_{SH} = 2.75$  eV as shown in Fig.6.2. Here, the number indicates the angle between the  $x$ -axis of the measurement system and the direction of the incident light polarization  $\mathbf{E}$ , which is continuously rotated from 0° to 360°. The SH signal shows two maxima along the crystal  $z$ -axis where the breaking of the space-inversion symmetry takes place. This observation again confirms ferroelectric polar order in the HoMnO<sub>3</sub> films.

Considering the spectral, polarization, and symmetry analysis of the SHG data, and their analogy to the SHG data of the ferroelectric single-crystal, it can be

concluded that HoMnO<sub>3</sub> films do have ferroelectric order.

## 6.2 Magnetic order

Similar to the electrically induced light polarization  $\mathbf{P}_i(2\omega)$ , the SH signal induced magnetically is expressed as Eq.1.14:

$$M_i(2\omega) \propto \chi_{ijk}^{MD} E_j(\omega) E_k(\omega)$$

$\chi_{ijk}^{MD}$  is sensitive to the breaking of time-reversal symmetry or the magnetic order of the material. As it is shown in Tab.1.1, each magnetic space group has specific non-vanishing tensor components of  $\chi_{ijk}^{MD}$  according to the magnetic order. With these tensor components, SHG can investigate the presence and symmetry of magnetic and, in particular, antiferromagnetic order. Because the tensor components will change when the magnetic structure changes, SHG detects magnetic phase transitions by the tensor component changes. For bulk HoMnO<sub>3</sub> it was shown that Mn<sup>3+</sup> antiferromagnetism leads to a SHG signal for light incident along the *c*-axis. In an anisotropy measurement, where the linear polarization of the incident fundamental light and of the detected SHG light are rotated simultaneously from 0 to 360°, the magnetic SHG signal exhibits a six-fold symmetry due to the triangular arrangement of the Mn<sup>3+</sup> ions.

An angular-dependence anisotropy measurement of SHG in a 240 nm HoMnO<sub>3</sub> film is shown in Fig.6.3. This was measured at 10.5 K where the magnetic order should be established. With this measurement, a magnetically induced SHG signal was expected. The light is incident along the *c*-axis (film plane normal). In this direction, the SH signal by electric polar order is prohibited, and the SH signal originates from magnetic order only. The values around the circle in Fig.6.3 indicate the angles of the polarization direction relative to a certain in-plane axis. The SH signal shows six-fold symmetry with an additional signal with 2-fold symmetry. These symmetries of SHG signal were considered that the six-fold symmetry was attributed to antiferromagnetic Mn<sup>3+</sup> order as in bulk crystals and the additional 2-fold symmetry was of ferroelectric origin due to a small tilting between  $\mathbf{k}$  and the *z*-axis. However, some recent temperature-dependent SHG measurements of HoMnO<sub>3</sub> thin films propose a different origin of the “*magnetic*” signal.

If the signal in Fig.6.3 originates from the magnetic order of Mn<sup>3+</sup> ions, it would show a temperature dependence and phase transitions like the single-crystal. Lottermoser and Fiebig [Lottermoser 04a] reported the temperature dependence of the

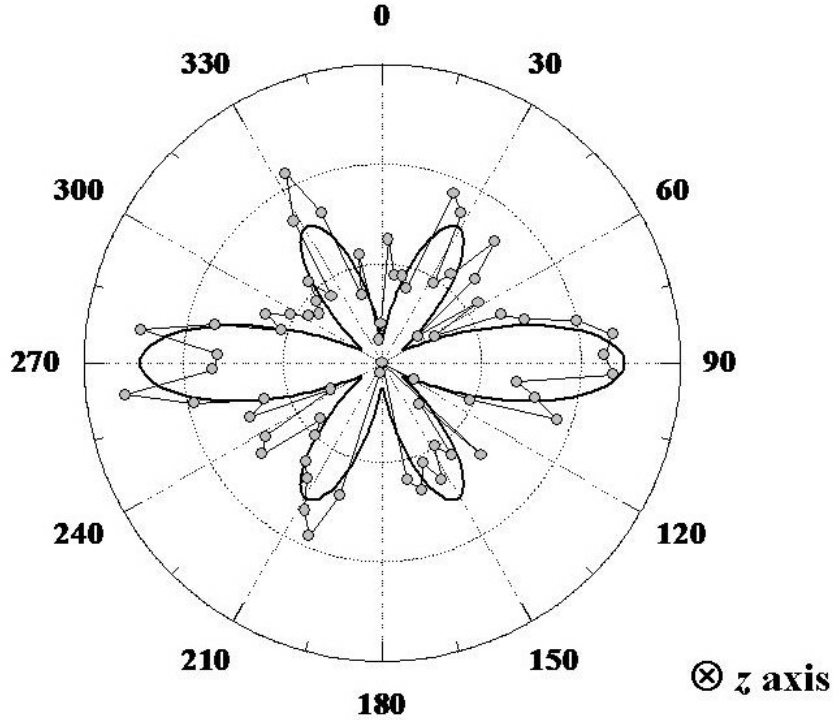


Figure 6.3: Angular-dependence anisotropy measurement of SHG in a  $\text{HoMnO}_3/\text{YSZ}(111)$  film (240 nm) measured at 10.5 K with light incident along the  $c$ -axis ( $\mathbf{k}||z$ ) [Kim 07c].

SH signal in a  $\text{HoMnO}_3$  single-crystal (Fig.6.4). The results show a clear Néel temperature  $T_N = 75$  K, and an abrupt magnetic phase transition at  $T_{SR} = 41$  K of the  $\text{Mn}^{3+}$ . As the magnetic phase changes, the six-fold magnetic SH signal turns its direction by  $90^\circ$  in accordance with the  $90^\circ$  rotation of the spins of the  $\text{Mn}^{3+}$  ions. The two antiferromagnetic orders can be clearly distinguished in a single-crystal. This six-fold symmetry of the signal and the anomalies at  $T_N$  and  $T_{SR}$  prove that these features arise from the magnetic order of the  $\text{Mn}^{3+}$  sublattice.

Figure 6.5 shows the temperature dependence of the SH signal in a  $\text{HoMnO}_3$  film (600 nm). In contrast to the single-crystal, the film doesn't show any anomalies at  $T_N$  or  $T_{SR}$ . The SH signal measured at  $0^\circ$  ( $\chi_{yyy}$ ) increases linearly as the temperature decreases, while the  $90^\circ$  SH signal ( $\chi_{xxx}$ ) does not change much. No magnetic phase transitions with a change of SHG tensor components have been detected. This implies that a  $\text{Mn}^{3+}$  spin reorientation has not happened in the film. Furthermore, it is remarkable that the finite signal observed up to 300 K.

With these facts, the origin of the SH signal measured along the  $c$ -axis should not be concluded as being from magnetic order of  $\text{Mn}^{3+}$ . Two questions arise at this point.

- 1) Why is the magnetic SH signal not observed?
- 2) What is the real origin of the signal with six-fold symmetry?

These questions can not be fully answered at this moment. However, some possible reasons can be considered.

For the first question, these are:

- The SH signal may be too weak to be detected because the size of the anti-ferromagnetic domains in  $\text{HoMnO}_3$  films may be small. When the lateral size of the domains is small, the magnetic SH signal becomes weaker due to a destructive interference between domains.
- The film might have a single ferroelectric domain. Domain imaging by piezo response force microscopy (PFM) indicates a possible single-domain state in thin films in contrast to the multidomain state of single-crystals. It is a matter of ar-

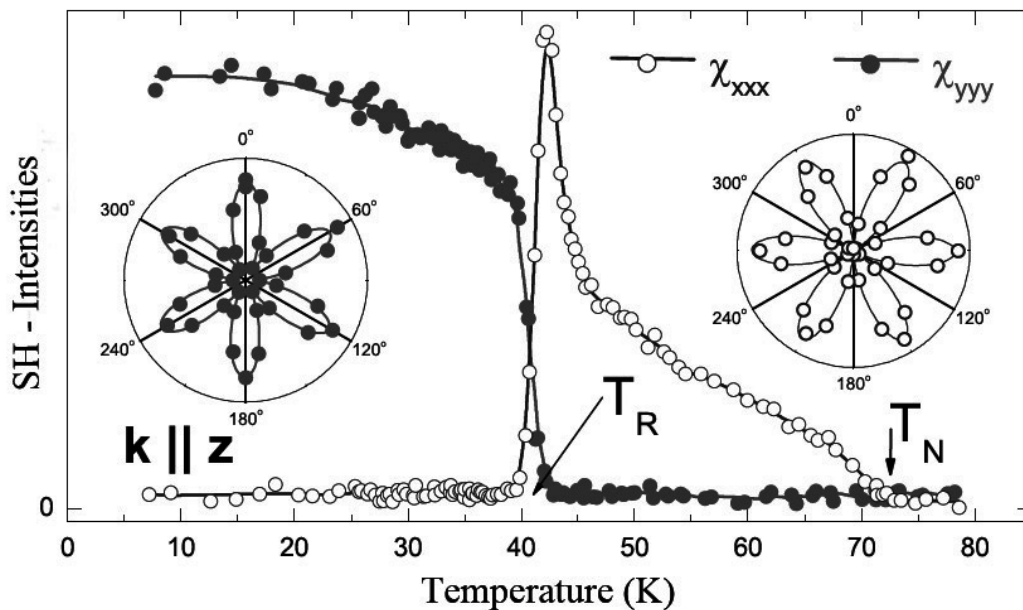


Figure 6.4: The temperature dependence of magnetic SHG in a  $\text{HoMnO}_3$  single-crystal. Below the Néel temperature,  $x$ -polarized light ( $\chi_{xxx}$ ) gives a signal. Below the spin reorientation temperature  $T_{SR}$  of  $\text{Mn}^{3+}$ , in contrast,  $y$ -polarized light ( $\chi_{yyy}$ ) produces a signal [Lottermoser 04a].



gument whether the films do actually have a single ferroelectric domain or whether the domain imaging by PFM is reliable even with the rather low resistivity of the films. However, if it is assumed that the film has a single ferroelectric domain, then this state is supposed to be the same as that of the single-crystal under a sufficiently large electric field [Lottermoser 04b]. In the case of a single-crystal, it has a single ferroelectric domain due to the applied electric field. In this state, the magnetic order of  $\text{Ho}^{3+}$  changes to ferromagnetic order. In addition, the superexchange interaction between  $\text{Mn}^{3+}-\text{O}^{2-}-\text{Mn}^{3+}$  in the basal plane is affected by the electric field through the magnetoelectric coupling. As a result, the magnetic order of  $\text{Mn}^{3+}$  moments changes from model  $\alpha$  (parallel  $\text{Mn}^{3+}$  spins for adjacent layers) to model  $\beta$  (antiparallel  $\text{Mn}^{3+}$  spins for adjacent layers) (Fig.2.4). Similar to single-crystal, the single ferroelectric domain state in films might lead to a magnetic order of  $\text{Mn}^{3+}$  like in model  $\beta$ , where the magnetic SH signal in crystals is very weak or vanishes [Kordel 08].

What is the origin of the “magnetic” signal? As shown in Fig.6.5, the signal is

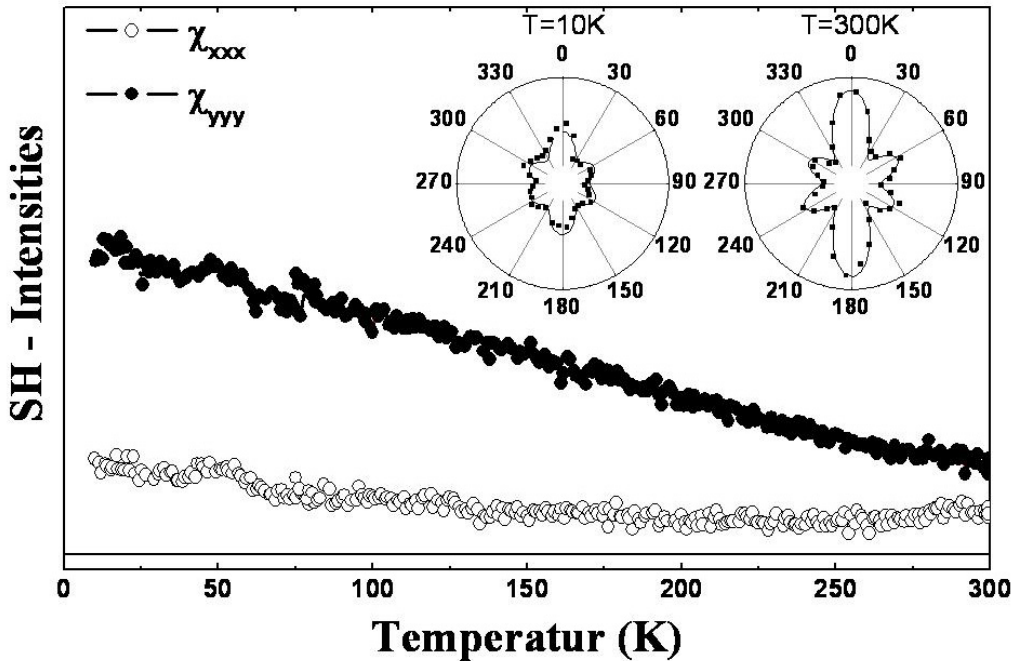


Figure 6.5: Temperature dependence of the second harmonic of a 600 nm thick film at  $E_{SH} = 2.75$  eV. The angular-dependent anisotropy measurements are taken at 10 K (left) and 300 K (right) [Kordel 08].

retained up to room temperature. This suggests the possibility that the origin is electric order. Misoriented crystallites of very low volume fraction may be an explanation for this behavior. According to HR-TEM investigations [Graboy 03, Gélard 09], some misoriented inclusions were found in the hexagonal YMnO<sub>3</sub>/YSZ(111) film, which is isostructural to hexagonal RMnO<sub>3</sub>. These inclusions have the correct hexagonal matrix, but are rotated by  $\sim 57^\circ$  around the  $\langle 1\bar{1}0 \rangle$  direction. This rotation produces the following orientation:

$$[111] \text{ RMnO}_3^{incl.} \parallel [001] \text{ RMnO}_3^{matrix}$$

Crystallites of this orientation can serve as a source of the six-fold symmetry signal, which is due to the ferroelectric contribution, since these misoriented crystallites have  $\mathbf{k} \parallel z$  with respect to the incident light. This produces an electric order contribution with 2-fold symmetry. In the hexagonal coordinate system, there are 3 equivalent  $\langle 1\bar{1}0 \rangle$  axes. This results in a six-fold symmetry.

In line with the TEM study, the misoriented inclusions have been detected recently by SHG [Kordel 09]. In this research, a tiny amount (estimated to be about 0.1 vol-%) but homogeneous distributed ferroelectric nanoinclusions was observed. In a comparative study, it is revealed that the nanoscale-sized misoriented inclusions is independent of growth techniques and film thickness. These inclusions have secondary orientations in the  $c$ -axis-oriented films and give contributions as polarized ferroelectric nanodomains, which are responsible for a six-fold symmetry in Fig.6.5.

### 6.3 Summary

A non-linear optical method, SHG has been employed as an effective tool for detecting electric and magnetic orders because of its sensitivity to the breaking of inversion and time reversal symmetries.

SH spectra for ferroelectric polar order of HoMnO<sub>3</sub> films were measured above the Néel temperature to avoid interference with any magnetic signal. Films show a spectrum with a two-peak structure around  $E_{SH} = 2.7$  eV, which is typical for the ferroelectric state of single-crystals. An angular-dependent anisotropy measurement further confirms the electric polar order. For instance, the electric SH signal of a 600 nm film shows the two-lobes shape as the light polarization is rotated. The maximum intensities are obtained for an incident light polarization along the  $z$  axis where the breaking of space inversion symmetry takes place. With these measurements, the ferroelectric polar lattice structure of the HoMnO<sub>3</sub> films has been confirmed.

SHG also detects the antiferromagnetic order of  $\text{Mn}^{3+}$  moments in  $\text{HoMnO}_3$ . Single-crystals show a six-fold symmetry from the magnetic structure of the  $\text{Mn}^{3+}$  sublattice. Thin films also show a six-fold symmetry in angular-dependent anisotropy measurements, with an additional 2-fold symmetry. However, recent measurements of SHG indicate that the six-fold symmetry in the films is not originating from the magnetic order [Kordel 08]. This is concluded from the observation that the SH signal of a 600 nm film does not vanish up to 300 K and does not show any magnetic phase transitions. Regarding that the six-fold symmetry signal was retained up to room temperature, it is likely to be of electric origin. A tiny volume fraction of misoriented grains detected with HR-TEM [Graboy 03, Gélard 09] and SHG [Kordel 09] investigations may be the origin for this SH signal in  $\text{HoMnO}_3$  films. Some possible reasons for the absence of a magnetic SH signal have been discussed, e.g. destructive interference from small magnetic domains or a single ferroelectric domain state associated with a magnetic structure leading to zero SH signals.



## Chapter 7

# Electrical properties

Hexagonal  $\text{HoMnO}_3$  is ferroelectric below the ferroelectric Curie temperature  $T_{CE} = 875$  K [Fujimura 96]. The spontaneous polarization is oriented along the hexagonal  $c$ -axis. As discussed in chapter 6, the ferroelectric polar order of films has been revealed by optical SHG measurements. Since ferroelectricity is defined as a *switchable* electric polarization, this has to be shown in  $\text{HoMnO}_3$  films by an applying electric field along the  $c$ -axis.

Therefore, the measurements of the electric polarization have been done perpendicular to the film plane at 300 K and at low temperatures. Capacitor trilayer structures using a Pt bottom electrode and top contacts of an area of about  $0.5 \text{ mm}^2$  have been prepared to apply the electric field.

In this chapter, the first results of ferroelectric polarization and attempts for magnetoelectric properties on  $\text{HoMnO}_3$  films will be discussed.

## 7.1 Ferroelectric polarization

Figure 7.1 shows the results of ferroelectric polarization measurements of a 300 nm thick film at 300 K. The applied voltage is varied from 1 – 3 V with the frequency of 10 Hz, providing a maximum field of 90 kV / cm for 3 V. This field is supposed to be sufficient to saturate a single-crystal (100 kV/cm at 40 Hz) [Lottermoser 02].

With the shape of the shown  $P(E)$  loops (Fig.7.1(a)), two features can be seen: Firstly, by the fact that the polarization is decreasing as the field is increasing, there is considerable leakage current flowing through the film. Secondly, switching is detectable from the steep slopes.

Figure 7.1(b) represents a typical current–field characteristic. From this curve, the switching behavior can be detected more clearly. The presence of polarization

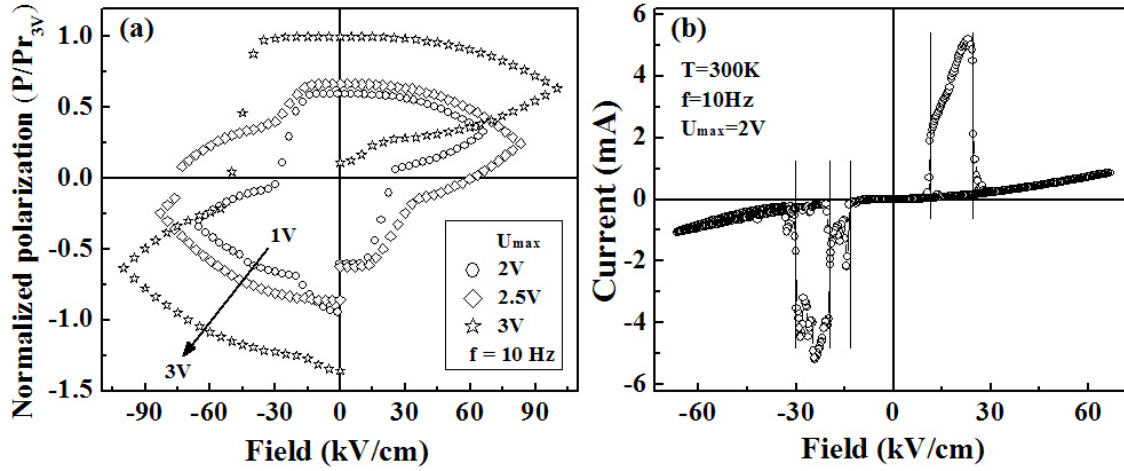


Figure 7.1: First observations of ferroelectric polarization of a  $\text{HoMnO}_3$  film at room temperature. (a) Polarization measurements at various electric fields (normalized with the remnant polarization ( $P_r$ ) of  $U_{max} = 3$  V), (b) a clear switching behavior of the ferroelectric order in the  $\text{HoMnO}_3$  film.

switching is obvious from the two large peaks, one situated between 14 and 28 kV/cm and the other at similar but negative fields. The small additional peak at negative field probably results from a film region with lower switching field. This and the width of the peaks indicates rather inhomogeneous switching of the polarization. On the positive side, this appears to be the first observation of ferroelectric switching at 300 K in any  $\text{HoMnO}_3$  film [Kim 07b].

The resistivity of the film (Fig.7.1) at 300 K is about  $10^7 \Omega\cdot\text{cm}$ . Most of films showed resistivity of  $10^6 - 10^7 \Omega\cdot\text{cm}$ . This value is only slightly lower than the required value for a good ferroelectric film, but nearly all films were leaky at 300 K to observe the ferroelectric switching. The resistivity becomes generally higher at low temperature. Therefore, low temperature polarization measurements have also been conducted. For this, the polarization measurement is carried out in a SQUID magnetometer (Fig.3.3). However, the leakage problem is still remained even at low temperatures.

## 7.2 Experimental difficulties with leakage current

Any direct measurement of magnetoelectric coupling requires the application of an electric field. This is necessary either for electrical control of the magnetic order

(magnetization), or ferroelectric polarization in an applied magnetic field. So the reduction of the leakage current in films is a prerequisite. The attempts done in order to reduce the leakage of the films, and possible origins for the leakage current are discussed.

The two typical steps have been done that are known to reduce leakage currents:

(i) Measurements were carried out at low temperature (5 K – 100 K) in a cryostat (both in the SQUID magnetometer and a cryogenic probe station with a tip contacting the top electrodes). Activated conduction processes can be efficiently suppressed this way. However, the observed current was not reduced much.

(ii) The area of the top contacts was reduced. For a number of films, lithographically processed 50  $\mu\text{m}$  Pt top contacts have been used and the samples were measured at 80 K. Even in this case, the leakage current could not be suppressed.

The Pt bottom electrode was considered as possible origin of the leakage, since it may form islands of considerable height (Fig.4.10) during  $\text{HoMnO}_3$  deposition at high temperature. If Pt *hillocks* penetrate through the ferroelectric film, it may produce shortcuts between the top and the bottom electrode. To avoid this problem, the  $\text{HoMnO}_3$  thickness has been enhanced up to 300 nm. However, the leakage current could not be removed.

Further, the Pt bottom electrode was substituted by conductive oxides, e.g.  $\text{La}_{0.7}\text{Sr}_{0.3}\text{MnO}_3$  and  $\text{La}_{0.7}\text{Ca}_{0.3}\text{MnO}_3$ . In this case, however, the  $\text{HoMnO}_3$  could not grow epitaxially in the hexagonal phase. Moreover, the leakage current still remained.

Another substrate had been employed, e.g.  $\text{Al}_2\text{O}_3$ , which was used for polarization experiments by the group of Prof. Noh in Seoul [Lee 07, Murugavel 07]. However, the hexagonal  $\text{HoMnO}_3$  phase was not easily obtained on  $\text{Al}_2\text{O}_3$  substrates with PLD deposition system. The Pt bottom electrode was tried to be deposited by another deposition technique, i.e. dc sputtering. The attempts to enhance the film's resistivity didn't bring satisfactory solutions so far.

### ***What is the possible origin of the leakage problem?***

Since a high-quality capacitor structure could not be prepared with a different bottom electrode material than Pt, conducting Pt paths through the ferroelectric film could be one of the possible reasons. The isostructural (and also chemically comparable)  $\text{YMnO}_3$  has been considered as a low-fatigue ferroelectric, and numerous publications on the good ferroelectric performance of  $\text{YMnO}_3$  films are available

[Ito 00, Fujimura 03, Martí 06]. In these, many use Pt bottom electrodes, too. However, the deposition temperature of the YMnO<sub>3</sub> film is typically lower. Thus, Pt interdiffusion might be a consequence of the high growth temperature of HoMnO<sub>3</sub> films that has been optimized for best HoMnO<sub>3</sub> structural quality. Hence, another optimization of the process, according to the lines used in YMnO<sub>3</sub> experiments appears promising to produce less leaky HoMnO<sub>3</sub> films.

The other possible origin of leakage currents are the HoMnO<sub>3</sub> films themselves. In oxide ferroelectrics, slight deviations of the oxygen content (over- or underoxygenation) are a typical reason for leakage and have also been proposed for hexagonal REMnO<sub>3</sub> films [Murugavel 07]. In general, point defects or vacancies of any of the three elemental components can cause the reduced resistivity even at a quite low concentration [Pabst 07]. It may be necessary to control the film composition with a precision of better than 1 % as Kordel *et al.* [Kordel 09] pointed out in REMnO<sub>3</sub> (RE = Y, Dy, Ho, Er) films by SHG measurements.

### 7.3 Summary

Using the capacitor trilayer structures, ferroelectric polarization measurements have been performed on a number of epitaxially grown HoMnO<sub>3</sub> films. A clear ferroelectric switching of the HoMnO<sub>3</sub> film could be demonstrated for the first time at room temperature on a 300 nm thick film. The result is important as a direct demonstration of the ferroelectricity of HoMnO<sub>3</sub> films.

A large number of films has been measured also at low temperatures, but generally a too large leakage current prevented the application of a sufficiently large electric field, even though the resistivity of the films was  $10^6 - 10^7 \Omega\cdot\text{cm}$ , which is not considerably lower than that of many ferroelectric oxide films.

The reason for leakage current could be either (i) a Pt interdiffusion / penetration from the bottom electrode through the ferroelectric HoMnO<sub>3</sub> film caused by the high growth temperature of the manganite, or (ii) a small compositional deviation, in particular in the oxygen content, of the HoMnO<sub>3</sub> films.

Since leakage current issues have been solved earlier for the very similar material of YMnO<sub>3</sub> considered for low-fatigue ferroelectric applications, the problem in HoMnO<sub>3</sub> might be possible to overcome in future experiments.



## Chapter 8

# Conclusions and outlook

The fundamental nature of multiferroic hexagonal HoMnO<sub>3</sub> films has been thoroughly investigated. Hexagonal HoMnO<sub>3</sub> is known for its strong magnetoelectric coupling, and has been prepared as thin films for the first time. The properties of HoMnO<sub>3</sub> thin films are discussed in comparison with those of single-crystals.

The films have been grown epitaxially on a YSZ(111) substrate with / without a Pt bottom layer by Pulsed Laser Deposition. The thickness range studied is 25 nm to 1000 nm. X-ray diffraction measurements indicate that the films are free of impurity phases and grown in the hexagonal phase with a single orientation with the *c*-axis along the film normal. Rocking curves reveal a good out-of-plane crystallinity with small FWHM values. Pole figures show a clear six-fold symmetry, which indicates a twin-free hexagonal phase. Films have been grown with low surface roughness; in particular, thicker films up to 1000 nm show rms roughness below 1 nm.

The lattice parameters vary systematically with the film thickness. The in-plane (*a*) and out-of-plane (*c*) lattice parameters both have been measured for a number of films. Thin films of  $d < 50$  nm are in a tensile-strained state, since the YSZ substrate is larger by about 3 %. The lattice parameters vary with the film thickness. Thicker films have enlarged lattice parameters *a* and *c* with respect to bulk values. The larger lattice parameters may originate from small deviations in composition or from lattice defects in the crystal lattice as the nano-inclusions detected by non-linear optics (SHG).

Superlattices with the isostructural YMnO<sub>3</sub> have been grown with a layer thickness down to 1 unit cell. A capacitor trilayer structure with Pt electrode has been prepared for electric property investigations.

Magnetic properties of hexagonal HoMnO<sub>3</sub> have been investigated based on magnetization measurements for both single-crystals and thin films in the temperature

range of 2 K to 300 K and for fields up to 7 T. For the single-crystal, a distinct transition to a low-temperature high-field phase with a ferromagnetic alignment of the  $\text{Ho}^{3+}$  moments was detected for the first time for  $T = 2$  K,  $\mu_0 H > 6.5$  T. For the films, the magnetic transitions based on the  $\text{Ho}^{3+}$  ordering could be detected in magnetization measurements. For instance, films show four low temperature anomalies in low magnetic field, which are related with  $\text{Ho}^{3+}$ 's contribution. On the other hand, the antiferromagnetic  $\text{Mn}^{3+}$  ordering at  $T_N$  and the  $\text{Mn}^{3+}$  spin reorientation at  $T_{SR}$  were not unambiguously detectable.

Several observations reveal that the antiferromagnetic interaction of  $\text{Ho}^{3+}$  moments is weakened in all films than in the single-crystals: the ordering temperature  $T_{Ho}$  and the paramagnetic Curie temperature for the  $\text{Ho}^{3+}$  sublattice is lower (as an absolute value) than in the single-crystal. The weakened antiferromagnetic phases lead to presumably somewhat suppressed transitions in the  $M(H)$  and  $M(T)$  curves than for the single-crystal. For instance, there are no pronounced metamagnetic transitions in the field-dependent data  $M(H)$  at  $T < 5$  K. The fact is tentatively attributed to the absence of the respective antiferromagnetic phases. The enlarged lattice parameters of thin films may serve as a reason for the weak antiferromagnetism in films via modification of the magnetic superexchange strength.

With all the magnetization measurements results, an approximate magnetic phase diagram of hexagonal  $\text{HoMnO}_3$  is constructed, and a modified phase diagram for the films is discussed.

Non-linear optical Second Harmonic Generation (SHG) measurements conducted in the group of M. Fiebig at the University of Bonn have revealed the same ferroelectric signal / spectrum for films as for  $\text{HoMnO}_3$  single-crystals with more spectral details and larger intensity. This gives evidence for the ferroelectric polar lattice structure, i.e. the presence of spontaneous polarization in the  $\text{HoMnO}_3$  films. On the other hand, the magnetic transitions where the  $\text{Mn}^{3+}$  sublattice orders or reorients could not be observed even though they are clearly detectable in single-crystals. The possible reasons for the invisibility of the magnetic order in films have been discussed.

Ferroelectric polarization has been measured for a number of films at 300 K and at low temperature ( $T \leq 100$  K). Most films proved to have a somewhat low resistivity ( $10^6 - 10^7 \Omega \cdot \text{cm}$ ) even at low temperature, so a sufficiently large electric field could not be applied to reverse the polarization or for the magnetoelectric control of the magnetic order. The likely reasons for the enhanced conductivity or leakage current in the capacitor trilayers using a Pt bottom electrode are (i) the

recrystallization (Pt hillock formation) and possible interdiffusion of the Pt as a consequence of the high  $\text{HoMnO}_3$  deposition temperature or (ii) vacancies / point defects in the  $\text{HoMnO}_3$  lattice. Nevertheless, polarization switching at about 30 kV / cm could be proven in one case at 300 K. This result is the first observation of room temperature ferroelectricity in  $\text{HoMnO}_3$  films thus far.

Thin films of magnetoelectric multiferroics are promising for electrical control of magnetic order, since the low film thickness leads to low voltages required for applying substantial electric fields. It turned out that two general obstacles have to be overcome on the way to make this approach successful:

(i) The complex and typically frustrated nature of multiferroics leads to an extreme sensitivity of their properties towards modifications of lattice parameters and composition. Therefore, the studies of thin films are difficult, revealing many deviating properties from bulk behavior.

(ii) The general challenge for ferroelectric films is to make them highly insulating for the application of large electric fields.

Though such experiments remain difficult, the identification of the magnetic phases and the investigation of the magnetoelectric properties of films are encouraging for future work. The leakage problem in  $\text{HoMnO}_3$  films might be solved by optimizing experimental conditions like other studies, e.g.  $\text{YMnO}_3$ ,  $\text{BiFeO}_3$ . The influence of strain on the multiferroic order and the magnetoelectric effect, in addition to a precise microstructural analysis, is a matter of research.

## References

- [Aizu 70] K. Aizu. *Possible Species of Ferromagnetic, Ferroelectric, and Ferroelastic Crystals*. Physical Review B **2**(3), 754–772, Aug 1970.
- [Ascher 66] E. Ascher, H. Rieder, H. Schmid and H. Stossel. *Some Properties of Ferromagnetoelectric Nickel-Iodine Boracite,  $Ni_3B_7O_{13}I$* . Journal of Applied Physics **37**(3), 1404–1405, 1966.
- [Astrov 60] D.N. Astrov. *The magnetoelectric effect in antiferromagnetics*. Sov. Phys.-JETP **11**, 708–709, 1960.
- [Barone 82] A. Barone and G. Paternò. *Physics and applications of the Josephson effect*. John Wiley & Sons, Inc., New York, 1982. pp.1-24, 383-424.
- [Bertaut 63a] E.F. Bertaut, F. Forrat and P. Fang. *Les manganites de terres rares et d'yttrium une nouvelle classe de ferroélectriques*. Comptes Rendus Académie des Sciences **256**, 1958–1961, 1963.
- [Bertaut 63b] E.F. Bertaut and M. Mercier. *Structure Magnétique de  $MnYO_3$* . Physics Letters **5**, 27–29, 1963.
- [Bertaut 71] E.F. Bertaut and M. Mercier. *Magnetoelectricity in theory and experiment*. Mat. Res. Bull. **6**, 907–922, 1971.
- [Birss 64] R.R. Birss. *Symmetry and magnetism*. vol. 3. North-Holland publ. Co., Amsterdam, 1964. pp.128-129, 133-136.
- [Brinks 01] H.W. Brinks, J. Rodríguez-Carvajal, H. Fjellvåg, A. Kjekshus and B.C. Hauback. *Crystal and magnetic structure of orthorhombic  $HoMnO_3$* . Physical Review B **63**(9), 094411, 2001.
- [Brown 68] W.F. Jr. Brown, R.M. Hornreich and S. Shtrikman. *Upper bound on the magnetoelectric susceptibility*. Physical Review **168**, 574–577, 1968.
- [Cheong 07] S.-W. Cheong and M. Mostovoy. *Multiferroics: a magnetic twist for ferroelectricity*. Nature Materials **6**, 13–20, 2007.
- [Chrisey 94] Edited by D.B. Chrisey and G.K. Hubler. *Pulsed laser deposition of thin films*. John Wiley & Sons, Inc., New York, 1994. pp.89-111, 144-146, 182-196, 232, 281-285, 455-456, 477-478.

- [Cullity 72] B.D. Cullity. *Introduction to magnetic materials*. Adison-Wesley publ. co., London, 1972. pp.92-111.
- [Cullity 78] B.D. Cullity. *Elements of x-ray diffraction*. Adison-Wesley publ. co., London, english, 2nd edition, 1978. pp.99-106, 277-279, 295-300, 501.
- [Curie 94] P. Curie. *Symétrie d'un champ électrique et d'un champ magnétique*. Journal de Physique **3e Série**, t.III, 393–415, 1894. Reprinted in Oeuvres de Pierre Curie, Gauthier-Villars, Paris, 1908, pp.118-141.
- [dela Cruz 05] C. dela Cruz, F. Yen, B. Lorenz, Y.Q. Wang, Y.Y. Sun, M.M. Gospodinov and C.W. Chu. *Strong spin-lattice coupling in multiferroic HoMnO<sub>3</sub>: Thermal expansion anomalies and pressure effect*. Physical Review B **71**(6), 060407(R), 2005.
- [Dho 04] J. Dho, C.W. Leung, J.L. MacManus-Driscoll and M.G. Blamire. *Epitaxial and oriented YMnO<sub>3</sub> film growth by pulsed laser deposition*. Journal of Crystal Growth **267**, 548–553, 2004.
- [Dörr 07] K. Dörr, C. Thiele, J.-W. Kim, O. Bilani, K. Nenkov and L. Schultz. *Approaches towards ferroelectric control of thin film magnetism*. Philosophical Magazine Letters **87**(3-4), 269–278, 2007.
- [Dubourdieu 07] C. Dubourdieu, G. Huot, I. Gelard, H. Roussel, O.I. Lebedev and G. Van Tendeloo. *Thin films and superlattice of multiferroic hexagonal rare earth manganites*. Philosophical Magazine Letters **87**, 203–210, 2007.
- [Dzyaloshinskii 60] I.E. Dzyaloshinskii. *On the magneto-electrical effect in antiferromagnets*. Sov. Phys.-JETP **10**, 628–629, 1960.
- [Ederer 04] C. Ederer and N.A. Spaldin. *A new route to magnetic ferroelectrics*. Nature Materials **3**, 849–851, 2004.
- [Ederer 05] C. Ederer and N.A. Spaldin. *Recent progress in first-principles studies of magnetoelectric multiferroics*. Current Opinion in Solid State and Materials Science **9**, 128–139, 2005.
- [Eerenstein 06] W. Eerenstein, N.D. Mathur and J.F. Scott. *Multiferroic and magnetoelectric materials*. Nature **442**, 759–765, 2006.
- [Fiebig 96] M. Fiebig. *Nichtlineare Spektroskopie und Topografie und antiferromagnetische Domänen*. Dissertation, Fachbereich Physik der Universität Dortmund, 1996. pp.38-49, 68-78, 118-121.

- [Fiebig 02] M. Fiebig, C. Degenhardt and R.V. Pisarev. *Magnetic phase diagram of  $HoMnO_3$* . Journal of Applied Physics **91**(10), 8867–8869, 2002.
- [Fiebig 03] M. Fiebig, Th. Lottermoser and R.V. Pisarev. *Spin-rotation phenomena and magnetic phase diagrams of hexagonal  $RMnO_3$* . Journal of Applied Physics **93**(10), 8194–8196, 2003.
- [Fiebig 05a] M. Fiebig. *Revival of the magnetoelectric effect*. Journal of Physics D-Applied Physics **38**(8), R123–152, 2005.
- [Fiebig 05b] M. Fiebig, V.V. Pavlov and R.V. Pisarev. *Second-harmonic generation as a tool for studying electronic and magnetic structures of crystals: review*. J. Opt. Soc. Am. B **22**(1), 96–118, 2005.
- [Folen 61] V.J. Folen, G.T. Rado and E.W. Stalder. *Anisotropy of the Magnetoelectric Effect in  $Cr_2O_3$* . Physical Review Letters **6**(11), 607–608, 1961.
- [Fröhlich 99] D. Fröhlich, St. Leute, V.V. Pavlov, R.V. Pisarev and K. Kohn. *Determination of the magnetic structure of hexagonal manganites  $RMnO_3$  ( $R=Sc, Y, Ho, Er, Tm, Yb$ ) by second-harmonic spectroscopy*. Journal of Applied Physics **85**(8), 4762–4764, 1999.
- [Fujimura 96] N. Fujimura, T. Ishida, T. Yoshimura and T. Ito. *Epitaxially grown  $YMnO_3$  film: New candidate for nonvolatile memory devices*. Applied Physics Letters **67**(7), 1011–1013, 1996.
- [Fujimura 03] N. Fujimura, H. Sakata, D. Ito, T. Yoshimura, T. Tokura and T. Ito. *Ferromagnetic and ferroelectric behaviors of A-site substituted  $YMnO_3$ -based epitaxial thin films*. Journal of Applied Physics **93**(10), 6990–6992, 2003.
- [Gélard 08] I. Gélard, C. Dubourdieu, S. Pailhès, S. Petit and Ch. Simom. *Neutron diffraction study of hexagonal manganite  $YMnO_3$ ,  $HoMnO_3$  and  $ErMnO_3$  epitaxial films*. Applied Physics Letters **92**, 232506, 2008.
- [Gélard 09] I. Gélard. *Heterostructures d'oxydes multiferroïques de manganites de terre-rares hexagonaux  $RMnO_3$  - Elaboration par MOCVD à injection et caractérisations structurales et physiques*. Dissertation, Grenoble -INP, 2009.
- [Graboy 03] I.E. Graboy, A.A. Bosak, O.Yu. Gorbenko, A.R. Kaul, C. Dubourdieu, J.-P. Sénateur, V.L. Svetchnikov and H.W. Zandbergen. *HREM Study*

- of epitaxially stabilized hexagonal rare earth manganites.* Chem. Mater. **15**, 2632–2637, 2003.
- [Gross 90] R. Gross, P. Chaudhari, M. Kawasaki, M. B. Ketchen and A. Gupta. *Low noise  $YBa_2Cu_3O_{7-\delta}$  grain boundary junction dc SQUIDS.* Applied Physics Letters **57**(7), 727–729, 1990.
- [Gupta 91] A. Gupta and B. W. Hussey. *Laser deposition of  $YBa_2Cu_3O_{7-\delta}$  films using a pulsed oxygen source.* Applied Physics Letters **58**(11), 1211–1213, 1991.
- [Heisenberg 28] W. Heisenberg. *Zur Theorie des Ferromagnetismus.* Z. Physik **49**, 619–636, 1928.
- [Hill 00] N.A. Hill. *Why are there so few magnetic ferroelectrics?* Journal of Physical Chemistry B **104**(29), 6694–6709, 2000.
- [Hill 02] N.A. Hill and A. Filippetti. *Why are there any magnetic ferroelectrics?* Journal of Magnetism and Magnetic Materials(29), 976–979, 2002.
- [Hirone 57] T. Hirone and K. Adachi. *On the magnetic properties of nickel-arsenide type crystals.* Journal of the Physical Society of Japan **12**(2), 156–163, 1957.
- [Holzapfel 92] B. Holzapfel, B. Roas, L. Schultz, P. Bauer and G. Saemann-Ischenko. *Off-axis laser deposition of  $YBa_2Cu_3O_{7-\delta}$ .* Applied Physics Letters **61**(26), 3178–3180, 1992.
- [Hur 04] N. Hur, S. Park, P.A. Sharma, J.S. Ahan, S. Guha and S-W. Cheong. *Electric polarization reversal and memory in a multiferroic material induced by magnetic fields.* Nature **429**, 392–395, 2004.
- [Ibach 95] H. Ibach and H. Lüth. *Solid-state physics - an introduction to principles of materials science.* Springer, Berlin, 2nd edition, 1995. pp.275-285.
- [Ito 00] D. Ito, N. Fujimura and T. Ito. *Initial stage of film growth of pulsed laser deposited  $YMnO_3$ .* Jpn. J. Appl. Phys. **39**, 5525–5527, 2000.
- [Iwata 98] N. Iwata and K. Kohn. *Dielectric anomalies at magnetic transitions of hexagonal rare earth manganese oxides  $RMnO_3$ .* Journal of the Physical Society of Japan **67**(9), 3318–3319, 1998.

- [Khomskii 06] D.I. Khomskii. *Multiferroics: Different ways to combine magnetism and ferroelectricity*. Journal of Magnetism and Magnetic Materials **306**(1), 1–8, 2006.
- [Kim 91] H. Kim. *Electroceramics (in Korean)*. Bando publ. co., Seoul, 1991. pp.25-35.
- [Kim 07a] J.-W. Kim, K. Dörr, A. Kwon and L. Schultz. *Epitaxial growth of multiferroic HoMnO<sub>3</sub> films and capacitor trilayers*. Journal of Magnetism and Magnetic Materials **310**(2, Part 2), e352–e354, 2007.
- [Kim 07b] J.-W. Kim, K. Dörr, K. Nenkov and L. Schultz. *Multiferroic properties of HoMnO<sub>3</sub> films and capacitor trilayers*. Journal of Applied Physics **101**(9), 09M108, 2007.
- [Kim 07c] J.-W. Kim, L. Schultz, K. Dörr, B. B. Van Aken and M. Fiebig. *Growth and multiferroic properties of hexagonal HoMnO<sub>3</sub> films*. Applied Physics Letters **90**(1), 012502, 2007.
- [Kim 09] J.-W. Kim, K. Nenkov, L. Schultz and K. Dörr. *Magnetic properties of thick multiferroic hexagonal HoMnO<sub>3</sub> films*. Journal of Magnetism and Magnetic Materials **321**, 1727–1730, 2009.
- [Kimura 03] T. Kimura, T. Goto, H. Shintani, K. Ishizaka, T. Arima and Y. Tokura. *Magnetic control of ferroelectric polarization*. Nature **426**, 55–58, 2003.
- [Kittel 96] C. Kittel. *Introduction to solid state physics*. John Wiley & Sons, Inc., New York, 7th edition, 1996. pp.364-370.
- [Koehler 64] W.C. Koehler, H.L. Yakel, E.O. Wollan and J.W. Cable. *A note on the magnetic structures of rare earth manganese oxides*. Physics Letters **9**(2), 93–95, 1964.
- [Kordel 08] T. Kordel. *Charakterisierung von Multiferroischen HoMnO<sub>3</sub>-Schichten mittels nichtlinearer Optik*. Diplomarbeit, Universität Bonn, 2008.
- [Kordel 09] T. Kordel, C. Wehrenfennig, D. Meier, Th. Lottermoser, M. Fiebig, I. Gélard, C. Dubourdieu, J.-W. Kim, L. Schultz and K. Dörr. *Nano domains in multiferroic hexagonal RMnO<sub>3</sub> films (R=Y,Dy,Ho,Er)*. Physical Review B **80**, 045409, 2009.



- [Krebs 93] H.-U. Krebs and O. Bremert. *Pulsed laser deposition of thin metallic alloys*. Applied Physics Letters **62**(19), 2341–2343, 1993.
- [Kwon 93] C. Kwon, Q. Li, X.X. Xi, S. Bhattacharya, C. Doughty, T. Venkatesan, H. Zhang, J.W. Lynn, J.L. Peng, Z.Y. Li, N.D. Spencer and K. Feldman. *High critical current densities in ultrathin  $YBa_2Cu_3O_{7-\delta}$  films sandwiched between  $(Pr_xY_{1-x})Ba_2Cu_3O_{7-\delta}$  layers*. Applied Physics Letters **62**(11), 1289–1291, 1993.
- [Kwon 07] A.R. Kwon, V. Neu, L. Schultz and S. Fähler. *Morphology and hard magnetic properties of epitaxial Nd-Fe-B films grown on Mo and Cr/Ta buffers*. Journal of Applied Physics **101**(9), 09K506, 2007.
- [Landau 84] L.D. Landau, E.M. Lifshitz and L.P. Pitaevskii. *Electrodynamics of continuous media*. Elsevier, Heidelberg, 2nd edition, 1984. pp.130-135, 172-177, This book was first published in 1957 (in Russian) by Landau and Lifshitz, translated to English in 1960 (Pergamon Press).
- [Lee 07] J.-H. Lee, P. Murugavel, D. Lee, T.W. Noh, Y. Jo, M.-H. Jung, K.H. Jang and J.-G. Park. *Multiferroic properties of epitaxially stabilized hexagonal  $DyMnO_3$  thin films*. Applied Physics Letters **90**, 012903, 2007.
- [Lonkai 02] Th. Lonkai, D. Hohlwein, J. Ihringer and W. Prandl. *The magnetic structures of  $YMnO_{3-\delta}$  and  $HoMnO_3$* . Appl. Phys. A **74**[Suppl], S843–S845, 2002.
- [Lonkai 03] Th. Lonkai, D.G. Tomuta, J.U. Hoffmann, R. Schneider, D. Hohlwein and J. Ihringer. *Magnetic two-dimensional short-range order in hexagonal manganites*. Journal of Applied Physics **93**(10), 8191–8193, 2003.
- [Lonkai 04] Th. Lonkai, D.G. Tomuta, U. Amann, J. Ihringer, R.W.A. Hexdrikk, D.M. Többens and J.A. Mydosh. *Development of the high-temperature phase of hexagonal manganites*. Physical Review B **69**, 134108, 2004.
- [Lorenz 04a] B. Lorenz, A.P. Litvinchuk, M.M. Gospodinov and C.W. Chu. *Field-induced reentrant novel phase and a ferroelectric-magnetic order coupling in  $HoMnO_3$* . Physical Review Letters **92**(8), 087204, 2004.
- [Lorenz 04b] B. Lorenz, Y.Q. Wang, Y.Y. Sun and C.W. Chu. *Large magnetodielectric effects in orthorhombic  $HoMnO_3$  and  $YMnO_3$* . Physical Review B **70**(21), 212412, 2004.

- [Lorenz 05] B. Lorenz, F. Yen, M.M. Gospodinov and C.W. Chu. *Field-induced phases in HoMnO<sub>3</sub> at low temperatures*. Physical Review B **71**(1), 014438, 2005.
- [Lottermoser 02] Th. Lottermoser. *Elektrische und magnetische Ordnung hexagonaler Manganite*. Dissertation, Fachbereich Physik der Universität Dortmund, 2002. pp.11-29, 39-42, 83-86, 92-96, 107-110, 149-152.
- [Lottermoser 04a] T. Lottermoser and M. Fiebig. *Magnetoelectric behaviour of domain walls in multiferroic HoMnO<sub>3</sub>*. Physical Review B **70**, 220407(R), 2004.
- [Lottermoser 04b] T. Lottermoser, T. Lonkai, U. Amann, D. Hohlwein, J. Ihringer and M. Fiebig. *Magnetic phase control by an electric field*. Nature **430**, 541–544, 2004.
- [Martí 06] X. Martí, F. Sánchez, D. Hrabovsky, L. Fàbrega, A. Ruyter, J. Fontcuberta, V. Laukhin, V. Skumryev, M.V. García-Cuenca, C. Ferrater, M. Varela, A. Vilà, U. Lüders and J.F. Bobo. *Exchange biasing and electric polarization with YMnO<sub>3</sub>*. Applied Physics Letters **89**, 032510, 2006.
- [McGuire 56] T.R. McGuire, E.J. Scott and F.H. Grannis. *Antiferromagnetism in a Cr<sub>2</sub>O<sub>3</sub> crystal*. Physical Review **102**(4), 1000–1003, 1956.
- [Muñoz 01] A. Muñoz, J.A. Alonso, M.J. Martínez-Lope, M.T. Casáis, J.L. Martínez and M.T. Fernández-Díaz. *Evolution of the magnetic structure of hexagonal HoMnO<sub>3</sub> from neutron powder diffraction data*. Chem. Mater. **13**, 1497–1505, 2001.
- [Murugavel 07] P. Murugavel, J.H. Lee, D. Lee, T.W. Noh, Y. Jo, M.H. Jung, Y.S. Oh and K.H. Kim. *Physical properties of multiferroic hexagonal HoMnO<sub>3</sub> thin films*. Applied Physics Letters **90**(14), 142902, 2007.
- [Nénert 07] G. Nénert. *Orbital ordering and multiferroics*. Dissertation, University of Groningen, the Netherlands, 2007. pp.55-59, 93-96.
- [O'Dell 70] T.H O'Dell. *The electrodynamics of magneto-electric media*. North-Holland publ. Co., London, 1970. pp.1-17, 116-117.
- [Ohring 91] M. Ohring. *The materials science of thin films*. Academic Press, Inc., London, 1991. pp.275-300, 307-322, 339-343, 347-350, 395-298.

- [Pabst 07] G.W. Pabst, L.W. Martin, Y.-H. Chu and R. Ramesh. *Leakage mechanisms in BiFeO<sub>3</sub> thin films*. Applied Physics Letters **90**, 072902, 2007.
- [Patra 07] A.K. Patra, V. Neu, S. Fähler, R. Groetzschel, S. Bedanta, W. Kleemann and L. Schultz. *Crystal structure and its correlation to intrinsic and extrinsic magnetic properties of epitaxial hard magnetic Pr-Co films*. Physical Review B **75**, 184417, 2007.
- [Prellier 05] W. Prellier, M.P. Singh and P. Murugavel. *The single-phase multiferroic oxides: from bulk to thin film*. J. Phys.: Condens. Matter **17**, R803–R832, 2005.
- [Rado 61] G.T. Rado and V.J. Folen. *Observation of the Magnetically Induced Magnetoelectric Effect and Evidence for Antiferromagnetic Domains*. Physical Review Letters **7**(8), 310–311, 1961.
- [Rado 74] G.T. Rado. *Present status of the theory of magnetoelectric effects*. Int. J. Magnetism **6**, 121–133, 1974.
- [Ramesh 07] R. Ramesh and N.A. Spaldin. *Multiferroics: progress and prospects in thin films*. Nature materials **6**, 21–29, 2007.
- [Roas 88] B. Roas, L. Schultz and G. Endres. *Epitaxial growth of YBa<sub>2</sub>Cu<sub>3</sub>O<sub>7-δ</sub> thin films by a laser evaporation process*. Applied Physics Letters **53**(16), 1557–1559, 1988.
- [Ryu 01] J. Ryu, A.V. Carazo, K. Uchino and H. Kim. *Magnetoelectric properties in piezoelectric and magnetostrictive laminate composites*. Jpn. J. Appl. Phys. **40**, 4498–4951, 2001.
- [Schmid 73] H. Schmid. *On a magnetoelectric classification of materials*. Int. J. Magnetism **4**, 337–361, 1973.
- [Schmid 94a] H. Schmid. *Introduction to the proceedings of the 2nd international conference on magnetoelectric interaction phenomena in crystals, MEIPIC-2*. Ferroelectrics **161**, 1–28, 1994.
- [Schmid 94b] H. Schmid. *Multi-ferroic magnetoelectrics*. Ferroelectrics **162**, 317–338, 1994.
- [Shen 03] Y.R. Shen. *The principles of nonlinear optics*. John Wiley & Sons, Inc., New Jersey, 2003. pp.13-17, 25-29, 202-209. This book was originally published with same title in 1984 (Wiley, New York).

- [Singh 05] A. Singh, R. Tamm, V. Neu, S.Fähler, C.-G. Oertel, W. Skrotzki, L. Schultz and B. Holzapfel. *Epitaxial growth of highly coercive Sm-Co thin films using pulsed laser deposition*. Journal of Applied Physics **97**, 093902, 2005.
- [Spaldin 05] N.A. Spaldin and M. Fiebig. *The renaissance of magnetoelectric multiferroics*. Science **309**, 391–392, 2005.
- [Sugie 02] H. Sugie, N. Iwata and K. Kohn. *Magnetic ordering of rare earth ions and magnetic-electric interaction of hexagonal RMnO<sub>3</sub> (R=Ho, Er, Yb or Lu)*. Journal of the Physical Society of Japan **71**(6), 1558–1564, 2002.
- [Vajk 05] O.P. Vajk, M. Kenzelmann, J.W. Lynn, S.B. Kim and S.W. Cheong. *Magnetic order and spin dynamics in ferroelectric HoMnO<sub>3</sub>*. Physical Review Letters **94**, 087601, 2005.
- [Vajk 06] O.P. Vajk, M. Kenzelmann, J.W. Lynn, S.B. Kim and S.W. Cheong. *Neutron-scattering studies of magnetism in multiferroic HoMnO<sub>3</sub>*. Journal of Applied Physics **99**(8), 08E301, 2006.
- [Van Aken 01] B.B. Van Aken, A.Meetsma and T.T.M. Palstra. *Hexagonal YMnO<sub>3</sub>*. Acta Crystallographica Section C **57**, 230–232, 2001.
- [Van Aken 04] B.B. Van Aken, T.T.M. Palstra, A. Filippetti and N.A. Spaldin. *The origin of ferroelectricity in magnetoelectric YMnO<sub>3</sub>*. Nature Materials **3**(3), 164–170, 2004.
- [von Helmolt 93] R. von Helmolt, J. Wecker, B. Holzapfel, L. Schultz and K. Samwer. *Giant negative magnetoresistance in perovskitelike La<sub>2/3</sub>Ba<sub>1/3</sub>MnO<sub>x</sub> ferromagnetic films*. Physical Review Letters **71**(14), 2331–2333, 1993.
- [Willmott 00] P.R. Willmott and J.R. Huber. *Pulsed laser vaporization and deposition*. Reviews of Modern Physics **72**(1), 315–328, 2000.
- [Wood 74] Van E. Wood and A.E. Austin. *Possible applications for magnetoelectric materials*. Int. J. Magnetism **5**, 303–315, 1974.
- [Yakel 63] H.L. Yakel and W.C. Koehler. *On the crystal structure of the manganese (III) trioxides of the heavy lanthanides and yttrium*. Acta Cryst. **16**, 957, 1963.
- [Yen 05] F. Yen, C.R. dela Cruz, B. Lorenz, Y.Y. Sun, Y.Q. Wang, M.M. Gospodinov and C.W. Chu. *Low-temperature dielectric anomalies in*

- 
- HoMnO<sub>3</sub>: The complex phase diagram.* Physical Review B **71**(18), 180407, 2005.
- [Yoshimura 03] T. Yoshimura and N. Fujimura. *Polarization hysteresis loops of ferroelectric gate capacitors measured by Sawyer-Tower circuit.* Jpn. J. Appl. Phys. **42**, 6011–6014, 2003.

## Publications

During Ph.D., some achievements were published in SCI journals as below.

- K. Dörr, O. Bilani-Zeneli, A. Herklotz, A.D. Rata, K. Boldyreva, J.-W. Kim, M.C. Dekker, K. Nenkov, L. Schultz and M. Reibold  
“A model system for strain effects: epitaxial magnetic films on a piezoelectric substrate”  
*Eur. Phys. J. B* **71**, 361-366 (2009)
- T. Kordel, C. Wehrenfennig, D. Meier, Th. Lottermoser, M. Fiebig, I. Gélard, C. Dubourdieu, J.-W. Kim, L. Schultz and K. Dörr  
“Nanodomains in multiferroic hexagonal RMnO<sub>3</sub> films (R=Y, Dy, Ho, Er)”  
*Physical Review B* **80**, 045409 (2009)
- J.-W. Kim, K. Nenkov, L. Schultz and K. Dörr  
“Magnetic properties of multiferroic hexagonal HoMnO<sub>3</sub> films”  
*Journal of Magnetism and Magnetic Materials* **321**, 1727-1730 (2009)
- J.-W. Kim, K. Dörr, K. Nenkov and L. Schultz  
“Multiferroic properties of HoMnO<sub>3</sub> films and capacitor trilayers”  
*Journal of Applied Physics* **101**, 09M108 (2007)
- K. Dörr, C. Thiele, J.-W. Kim, O. Bilani, K. Nenkov, L. Schultz  
“Approaches towards ferroelectric control of thin film magnetism”  
*Philosophical Magazine Letters* **87**, 269-278 (2007)
- J.-W. Kim, L. Schultz, K. Drr, B. B. Van Aken and M. Fiebig  
“Growth and multiferroic properties of hexagonal HoMnO<sub>3</sub> films”  
*Applied Physics Letters* **90**, 012502 (2007)
- J.-W. Kim, K. Dörr, A.-R. Kwon and L. Schultz  
“Epitaxial growth of multiferroic HoMnO<sub>3</sub> films and capacitor trilayers”  
*Journal of Magnetism and Magnetic Materials* **310**, e352-e354 (2007)

## ■ Award

The presentation entitled “Preparation and characterization of multiferroic hexagonal HoMnO<sub>3</sub> films” was awarded for ‘**Young Scientist Award**’ at the E-MRS spring meeting held at Strasbourg, France, 26-30 May 2008.

## Acknowledgements

Herewith I give my gratitude to whom helped me a lot during my Ph.D. work. With the supports of many people, this work could be successfully accomplished.

Above all I heartily appreciate to Prof. Ludwig Schultz for giving me a chance to perform my Ph.D. at IFW. I equally appreciate to my research supervisor, Dr. Kathrin Dörr for her active discussions and effective research guidelines.

I thank to the defence committee, the chairperson Prof. B. Kieback, the committee members Prof. J. Eckert, Dr. O. Gutfleisch and Prof. M. Fiebig. Especially I sincerely thank to Prof. Manfred Fiebig for being the second reviewer of this dissertation and the collaboration of SHG experiments.

I would not forget to thank to Dr. Konstantin Nenkov for the SQUID measurements, Mrs. Kerstin Pittruff for the experimental supports and all the library staffs for their quick and precise searching service. I thank to the group members of Prof. Fiebig, Dr. Bas B. van Aken, Tobias Kordel, Christian Wehrenfennig for the intensive SHG experiments.

I also give my thanks to Dr. Karl-Hartmut Müller, Dr. Nadezda Kozlova and Mrs. Angela Heinrich. They gave me a lot of useful advises and led me to adapt easily, when I firstly started to work in IFW. I am so grateful to the former and current group members, Dr. Diana Rata, Orkidia Bilani, Martina Cornelia Dekker, Andreas Herklotz, Dr. Christian Thiele, Dr. Ramesh Babu Gangineni, Dr. Ksenia Boldyreva and the former office neighbor Dr. Ajit Kumar Patra for the useful scientific discussions, experimental supports as well as social activities. I thank to Dr. Volker Neu for his kind help to prepare In-House Ph.D. seminar. It's sad that I cannot mention here all colleagues and friends in IFW, however I also give my kind greetings to them. I would not forget you and surely will keep in touch.

This work has been carried out with the help of fellowship financial supports granted by DAAD (Oct.2004-Nov.2008) and IFW (Dec.2008-Dec.2009). I heartily appreciate its fellowship supports.

Finally I would like to give my special thanks to my lovely family, Ah-Ram, Sumin, Jong-Ho and parents as well as parents-in-law for their mental encouragements and constant supports all through my life.